C.1

The University of Michigan

MASS AND ANGULAR DISTRIBUTIONS OF CHARGED DIHADRON PRODUCTION

by

Mary Anne Clare Cummings

A dissertation in partial fulfillment
of the requirements for the degree of
Doctor of Philosophy
(Physics)
in The University of Michigan
1990

LIBOFFCE
FERMILAB
THESIS

UM HE 90-41

MASS AND ANGULAR DISTRIBUTIONS OF CHARGED DIHADRON PRODUCTION

by

Mary Anne Clare Cummings

A dissertation in partial fulfillment
of the requirements for the degree of
Doctor of Philosophy
(Physics)
in The University of Michigan
1990

Doctoral Committee:

Professor Lawrence Jones Chair
Professor Gordon MacAlpine
Ass. Professor R. Akhoury
Ass. Professor Jean Krisch
Ass. Professor Greg Snow
Research Scientist H. Richard Gustafson

ABSTRACT

Experiment 711, conducted at Fermilab, provided a unique handle towards understanding valence quark scattering by studying pairs of single, charged, high-transverse momentum hadrons produced in collisions of 800 GeV/c protons on fixed metal targets. The apparatus consisted of a double-arm spectrometer, calorimetrically triggered, with high momentum resolution and a large angular acceptance for all charge states of particle pairs. The experiment was designed to select those hadron pairs that carried most of the momentum and energy of the underlying scattered quarks and gluons. The charge of such "leading" hadrons is correlated with the charge of the quark that produced it. Quantum Chromodynamics (QCD) assumes that the scattering behavior of quarks is independent of their charge, or "flavour"; Experiment 711 could test this assumption.

This dissertation describes the analysis of the mass and angular distributions of hadron pair production for three separate charge states: +-, ++ and --. The angular distributions are found to deviate from theory predictions of flavour symmetry. Also, the mass cross sections indicate ratios of positive to negative hard-scattered particles that are larger than expected from theory. These results could warrant reconsideration of the assumptions and approxiamtions currently made in leading-order QCD calculations.

To My Parents, Owen and Ruth Cummings

ACKNOWLEDGMENTS

My thanks goes first to my committee chairman, Larry Jones, who managed to see a potential scientist in a very unlikely candidate, and consistently provided financial and moral support throughout my graduate school carrer. Dick Gustafson was my effective advisor for the duration of my experiment, and for years has been a great friend and mentor. He has been the principal source of inspiration and guidance since the beginning of my education as a scientist. As my committee members, Jena Krisch, R. Akhoury, Greg Snow and Gordon MacAlpine provided me with excellent feedback and suggestions.

Andy Lathrop and Fred Lopez made my difficult transition from student to scientist (by no means over) bearable and even fun. They were invaluable in the construction and setup of E711, and in the final analysis (which was mine), they proved to be RIGHT all along. I would like to thank my fellow graduate students, who went through many difficult times along with me: Gianluigi Boca, Kathy (Turner) Streets, Herman White and Christopher Young. Thnaks also to Lee Sawyer who took some of the heat with us. My stay as a guest at Florida State University was made pleasant and productive by the assistance and kindness of Sharon and Vasken Hagopian. Much advice and help came from Kurtis Johnson and Jonathan Streets during the data reduction and analysis. Jeff Owens was very generous with his time and knowledge in many hours of discussion over QCD theory. I also acknowledge the rest of the FSU contingent for their participation in the analysis: Christos Georgiopoulos, J. Harvey Goldman and D. Levinthal.

As for the Fermilab contingent, I should thank Stephen Pordes and Michael Crisler for some face-slappingly astute admonition from the real world. E711 had first-rate technical assistance from Andy Lathrop, Bill Burley and Sharon Austin, and my thanks for their friendship as well as their competence. The Fermilab operators put up with innumerable frantic calls from E711 and 14 other experiments during the run, and managed to consistently deliver beam amid the sound and fury. In particular, thanks to

Carl Hebron, Maxwell Monningh and Tara Vraniak for their help in beam tuning and innumerable other tasks in the neutrino beamline which many of the experimenters never know to appreciate. I also acknowledge the many hours of help from Peter Heineke and Nancy Hughart while managing the E711 computer.

Many other people who were not on my experiment were invaluable sources of advice and good cheer: Gary Johannes, Stephan Linn, Bruce Straub, Saul Youssef and Maxwell Monningh. All have been good friends and teachers. Especially, my lasting thanks to Maxwell Monningh for his patience and innovation in taking on the considerable task of typesetting my dissertation.

TABLE OF CONTENTS

DEDICATION ii

ACKNOWLEDGMENTS iii

LIST OF TABLES viii

LIST OF FIGURES x

LIST OF APPENDICES xiii

CHAPTER

1 ANGULAR DISTRIBUTIONS AND QCD 1

1.1 High Pt Phenomena and the Structure of Matter 1

1.2 Hadron Pair Production 6

1.3 Fermilab Experiment E711 10

2 APPARATUS 14

2.1 Design 14

2.2 Beamline 18

2.2.1 Beamline elements 18

2.2.2 Beam monitoring and luminosity 19

2.3 Targets 19

2.4 Magnets 22
2.5 Drift Chambers 24
2.6 Calorimeter and Hodoscopes 25
2.6.1 Design 25
2.6.2 Calibration 29
2.7 Muon Trigger 31

3 APPARATUS TRIGGERING AND DATA ACQUISITION 34

3.1 Organisation 34
3.2 Trigger Design and Operation 35
3.2.1 The P trigger elements 36
3.2.2 The Q and Q • P trigger elements 33
3.2.3 The M and Q • P • M trigger elements . . . 39
3.2.4 Event triggers 41
3.3 Data Readout and Transfer 43
3.3.1 A-interrupt 43
3.3.2 B-interrupt 44
3.4 Online Monitoring 45

4 ANALYSIS 48

4.1 Variables Used in This Analysis 48
4.2 Definition of the Cross Sections 50
4.3 Data Reduction - Event Sample 51
4.3.1 Track reconstruction 52
4.3.2 Calorimeter information 53
4.3.3 Data set selection 54
4.4 Momentum Calculation 62
4.5 Acceptance Calculation 63
4.6 Efficiencies 67
4.6.1 Mass trigger efficiency 67
4.6.2 Trackfitter efficiency 68

4.6.3 Chamber plane and dead wire efficiency 69
4.7 Normalisation 70
4.8 Background 76

5 MASS AND ANGULAR DISTRIBUTIONS 78

5.1 Cross Sections 78
5.1.1 Differential cross sections in mass 79
5.1.2 Angular distributions 80
5.1.3 Ratio of charge states 81

6 QCD CALCULATIONS 101
6.1 QCD 101
6.1.1 Distribution and Fragmentation functions 102
6.1.2 QCD coupling constant 103
6.2 Calculations 107
6.2.1 Parton kinematics 107
6.2.2 Dihadron cross section 109
6.2.3 Angular distributions 108
7 CONCLUSION 114

APPENDICES 116

REFERENCES 127

LIST OF TABLES

Table

2.1 Target characteristics 21

2.2 Nominal photomultiplier tube gain settings 32

3.1 Q•P trigger segment composition 37

3.2 Event trigger composition 41

3.3 A interrupt list 44

3.4 B-interrupt list 45

4.1 DST production 53

4.2 CDSF event data list 61

4.3 Data reduction summary 62

4.4 Calculated target dependant errors 63

4.5 Mass trigger efficiency 68

4.6 Trackfitter efficiencies 69

4.7 Total integrated luminosity 75

4.8 Percentage of background events 77

5.1 Data for mass cross sections from Be target 87

5.2 Data for mass cross sections from Al target 88

5.3 Data for mass cross sections from Fe target 89

5.4 Data for mass cross sections from W target 90

5.5 Normalised Cosθ Distribution for + - pairs at $6.5<M<7.5$ Gev/c^2 91

5.6 Normalised Cosθ Distribution for + - pairs at $7.5<M<15.0$ Gev/c^2 92

5.7 Normalised Cosθ Distribution for + + pairs at $6.5<M<7.5$ Gev/c^2 93

5.8 Normalised Cosθ Distribution for + + pairs at 7.5<M<15.0 Gev/c^2 94

5.9 Normalised Cosθ Distribution for - - pairs at 6.5<M<7.5 Gev/c^2 95

5.10 Normalised Cosθ Distribution for - - pairs at 7.5<M<15.0 Gev/c^2 96

5.11 Cosθ distributions fit to QCD parametrisations 97

6.1 Cross sections for lowest order QCD subprocesses 111

6.2 Relative contributions of lowest order QCD subprocesses 112

A1.1 Calibration constants of longitudinal sections 118

A2.1 Chamber wire spacing 120

A2.2 Chamber Wire Voltages 120

A2.3 Chamber Wire Diameters 121

A2.4 Number of Sense Wires in Each Chamber Plane 121

A2.5 Chamber Active Region Dimensions 121

LIST OF FIGURES

Figure

1.1 Classical scattering of particle m_1 with charge e_1 against particle m_2 with charge e_2 1

1.2 Comparison of inelatsic scattering at the atomic and nucleon levels 3

1.3 Constituent scattering subprocces in nucleon collision . . . 5

1.4 Bias effects in high pt production 6

1.5 $\langle z \rangle$ versus p_t for inclusive π_0 production at $\sqrt{s}$ of 31, 44.8, and 62.4 GeV 8

1.6 Di-jet data from E609 9

1.7 Angular distribution for two-jet events from the UA1 experiment 11

1.8 Angular distribution of π_0's from the CCOR data at $\sqrt{s}$ = 44.8 GeV 13

2.1 Plan view of the E711 detector 15

2.2 Side view of the E711 detector 16

2.3 "Beam's eye" view of the E711 calorimeter 17

2.4 The E711 beamline elements 20

2.5 Target and luminosity monitor setup 21

2.6 Data from ZIPTRACK magnetic field measurement 23

2.7 Front view of the E711 calorimeter 27

2.8 Side view of the E711 calorimeter and hodoscopes 28

2.9 Example of an E711 calorimeter module 29

2.10 Muon trigger setup 33

3.1 Module composition of a P trigger (a) and Q•P trigger (b) 38
3.2 Module composition of an M trigger element 40
3.3 Total logic schematic for the E711 trigger 39
3.4 Display of trigger segment latches from monitoring program 47
4.1 Track y-intercept at the plane of the target 56
4.2 Turn-on curve for trigger segment P latch 57
4.3 Energy-momentum deviation 59
4.4 Number of tracks per event 60
4.5 Geometric acceptance at y= -0.2 and y=0.2 64
4.6 P_t scattering plane decomposition 66
4.7 NECIC beam monitor calibration 72
4.8 Calibration of magnet NECH 73
4.9 Example of a target scan 74
4.10 Delay curves for pairs trigger 76
5.1 Phase space cut on rapidity 82
5.2 Phase space cut on net P_t of pair 83
5.3 Differential mass cross sections for + - pairs 84
5.4 Differential mass cross sections for + + pairs 85
5.5 Differential mass cross sections for - - pairs 86
5.6 Plot of Cosθ Distribution for + - pairs at 6.5<M<7.5 Gev/c^2 91
5.7 Plot of Cosθ Distribution for + - pairs at 7.5<M<15.0 Gev/c^2 92
5.8 Plot of Cosθ Distribution for + + pairs at 6.5<M<7.5 Gev/c^2 93
5.9 Plot of Cosθ Distribution for + + pairs at 7.5<M<15.0 Gev/c^2 94

5.10 Plot of Cosθ Distribution for - - pairs at 6.5<M<7.5 Gev/c^2 95
5.11 Plot of Cosθ Distribution for - - pairs at 7.5<M<15.0 Gev/c^2 96
5.12 ++/-- pairs ratios versus mass 98
5.13 +-/++ pairs ratios versus mass 99
5.14 +- /-- pairs ratios versus mass 100
6.1 Schematic of hadron interaction 102
6.2 Feynman diagrams for lowest order QCD subprocesses 104
6.3 Screening of electromagnetic and strong charge. 105
6.4 Redefinition of strong coupling constant 106
A1.1 Total energy deposited in calorimeter (calibration) 118
A3.1 Calculation of momentum 124

LIST OF APPENDICES

Appendix

1. Calorimeter Calibration 116
2. Chamber Construction 119
3. Momentum Calculation 122
4. Lorentz Boost Of 2 Particle System 125

CHAPTER 1

INTRODUCTION

1.1 High-Pt Phenomena and the Structure of Matter

The study of high transverse momentum phenomena has been the principle means of modern physics for investigating the small scale structure of matter. A simple example of classical scattering is shown in Figure 1.1.

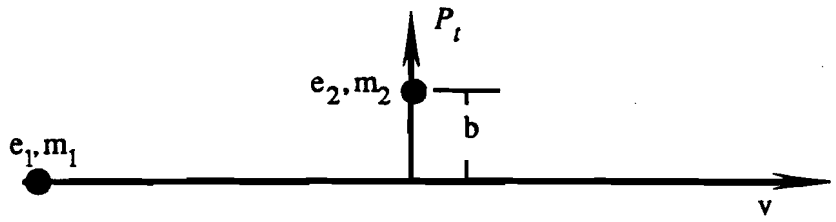

Figure 1.1
Classical scattering of particle m_1 with charge e_1 against particle m_2 with charge e_2.

$$p_t = \frac{2e_1 \times e_2}{b \times v} \tag{1.1.1}$$

The impact parameter b, is small in these collisions, so a "high-p_t" particle is the result of a close-range scatter. This kind of hard scatter indicates the concentrated presence of charge, a non-uniform distribution of matter on the scale of the interaction. Rutherford, in 1911, was able to infer the localised, compact structure of the nucleus in the atom from observing high-p_t scattering of charged particles off of a gold foil. The number of particles scattered into a given area of solid angle is given by the expression for the differential cross section

$$\frac{d\sigma_R}{d\Omega} = \frac{Z^2\alpha^2}{4E^2} \cdot \frac{1}{\sin^4(\theta/2)} \tag{1.1.2}$$

where α is a constant denoting the strength of the electromagnetic interaction related to the electric charge, Z is the number of protons in the gold nucleus, E is the energy of the incoming particle and θ is the polar angle of its scattering trajectory.

Charge is a more general concept than the familiar electrostatic charge. It is related to the probability of coupling and momentum exchange between "particles", a measure of the strength of the interaction. In the 1930's a picture emerged of this interaction as comprising an exchange of an intermediate particle that carried the momentum transferred. The field is thereby quantised into these exchange particles through which all physical interactions are communicated. For the electromagnetic interactions, this exchange particle is a virtual photon. "Virtual" here means that the photon exists for a very brief time such that energy may not be conserved for the duration of the exchange. This license is a consequence of the quantisation of matter and energy, and is expressed by the Heisenberg uncertainty principle $\Delta E \times \Delta t = \hbar$, where $\hbar$ is Plank's constant. Loosely, it can be said to describe the "granularity" of nature that quantisation introduces. The uncertainty principle can be expressed by another set of "canonical" variables (those sets of variables providing complete information of the dynamical system), namely $\Delta p \times \Delta x = \hbar$. This reflects the same relation of impact parameter to transverse momentum described classically above. The interpretation of the Rutherford experiment can be seen as an exchange of a high-p_t, i.e. short wavelength, photon between the incoming particle and the nucleus. This short wavelength photon better defines the nucleus than would a photon of longer wavelength (lower p_t).

More recently, a similar field theory has emerged to describe the forces in the nucleus. After several attempts to construct such a theory with the π mesons as the

exchange "quantum" proved inadequate, there emerged a theory of the baryon structure, wherein the nucleons and mesons were themselves composed of smaller particles, or "partons". Experiments measuring deep inelastic proton-proton scattering[1] found a p_t distribution consistent with hard-core constituents in the proton substructure. Figure 1.2 shows this result compared to Rutherford's findings on the atomic level. Both p_t spectra exhibit a similar power law deviation from the exponential dependence at their low end, where the structure of the next scale becomes evident (i.e. objects once behaving like particles show signs of internal structure). The higher momentum exchange particle , with its shorter wavelength, can more effectively illuminate the smaller-scale structure of the objects involved in the scattering process. Nucleons, by analogy to the Rutherford atom, appear to have dense "nuclei" of "strong" charge, whose structure starts manifesting in hadronic interactions with p_t above 1 GeV/c. The subnucleon partons experience a short-range scatter by exchanging a quantum of the nuclear or "strong" force, analogous to the photon.

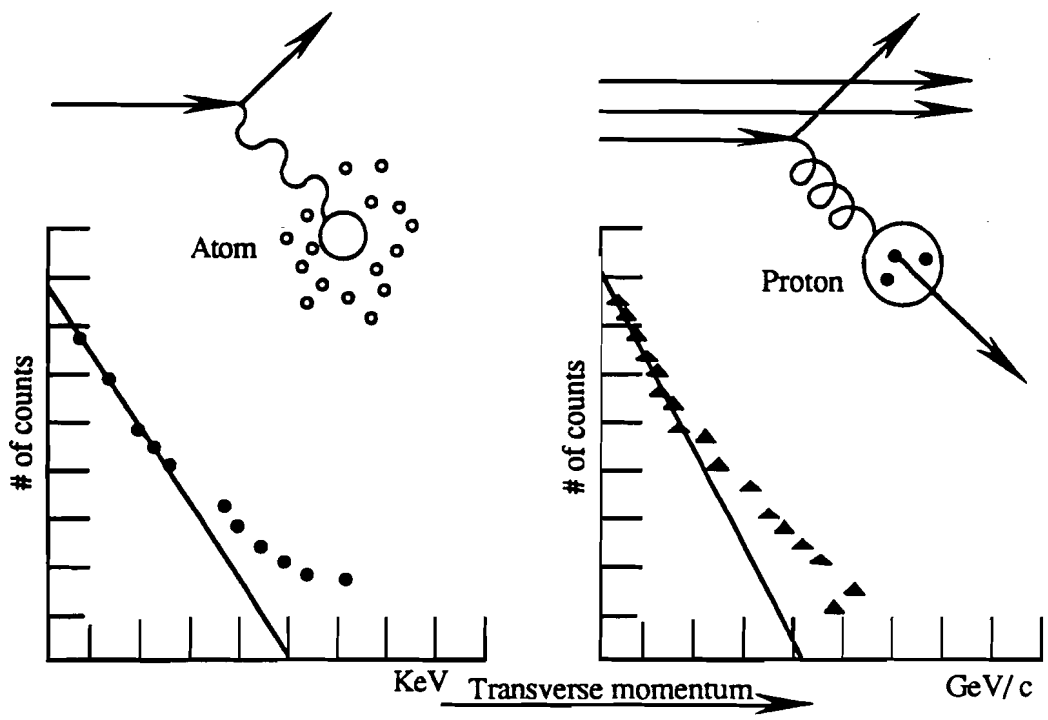

Figure 1.2
Comparison of inelastic scattering at the atomic and nucleon levels.

In fact, at very short distances, the behavior of the scattered nucleon constituents can be expressed by an analogue to Rutherford's formula

$$\frac{d\sigma_R}{d\Omega} \sim \frac{\alpha_s^2}{4E^2} \cdot \frac{1}{\sin^4(\theta/2)} \tag{1.1.3}$$

where α_s relates the strength of the nuclear (strong) force.

There are some complications with this particular field theory. The strong force couples to a kind of charge different from that of the electromagnetic force. The strong-force charge is dubbed colour, and there are three kinds: red, blue and green. These have nothing to do with ordinary colour, the terminology just being an analogue to the way all real colours are made up of three primary colours. The intermediate exchange particle for the strong force is called a gluon, and this differs from the photon in its ability to couple to itself (as it also carries a colour charge) as well as the primary coloured particles, called quarks. Another peculiarity of the strong charge is that, unlike its electromagnetic counterpart, no colour charge is ever observed directly. This will be expanded upon in a later chapter, but the effect experimentally is that the scattered quark or gluon is violently decelerated (the coupling increases, rather than decreases with distance), and radiates hadrons, similar to the bremsstrauhlung radiation emitted by accelerated electrons. These hadrons form a "jet" of particles in a cone centered around the original parton direction. This jet of particles is what is seen experimentally. Since the partons are always found in bound colour-neutral particles, the initial states of the scatter are indeterminate as the quarks and gluons carry varying amounts of the hadron's or meson's momentum. Figure 1.3 illustrates the smaller scale scatter in a proton-nucleon collision. These distributions, as well as the composition of final state jets, have been studied extensively in earlier experiments[2][3][4]. Several parametrisations have been constructed to describe their functional dependence on various physical quantities. It is necessary to fold these into any QCD calculation to interpret the distributions of hadronic final states in the laboratory, and will be discussed in a later chapter.

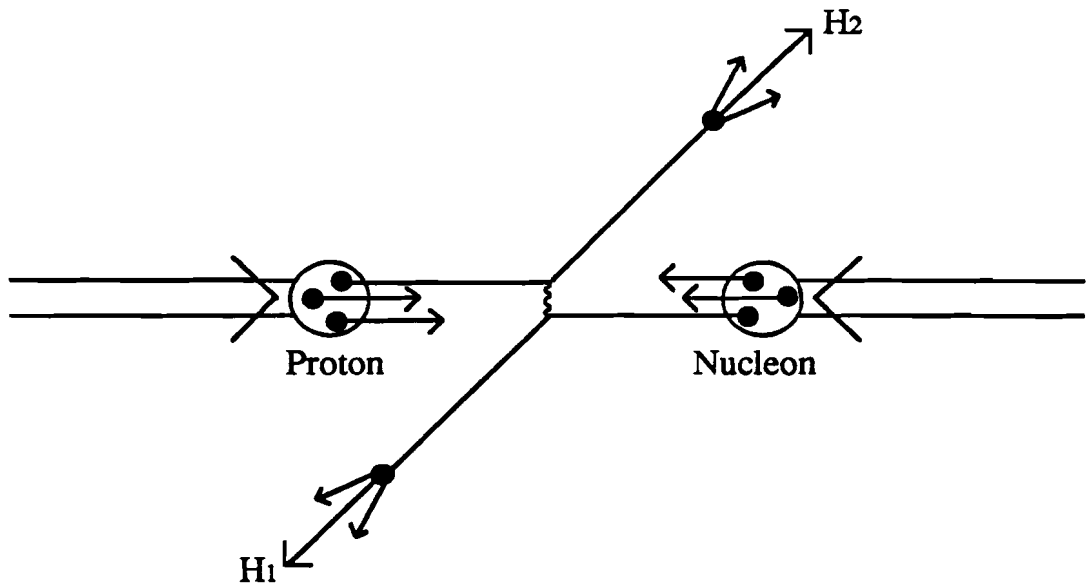

Figure 1.3
Constituent scattering subprocess in nucleon collision

The first experiments to probe the parton substructure of nucleons from p-p collisions triggered on single high-p_t pions (> 1 GeV/c^2)[5]. The true p_t spectrum of these events were smeared by the fact that this trigger favoured those pions coming from partons whose intrinsic transverse motion in the protons were toward the direction of the detector. Later, experiments with "symmetric", or two-armed, detectors were introduced to eliminate this "trigger bias", and provide complete information on final state kinematics (see Figure 1.4).

The jet structure of the final state requires the momentum and energy reconstruction of many particles. This introduces analytic difficulties, particularly at lower energies where the jets are less collimated, and their composite particles difficult to sort out from those of the "spectator jets" from the non-interacting partons.

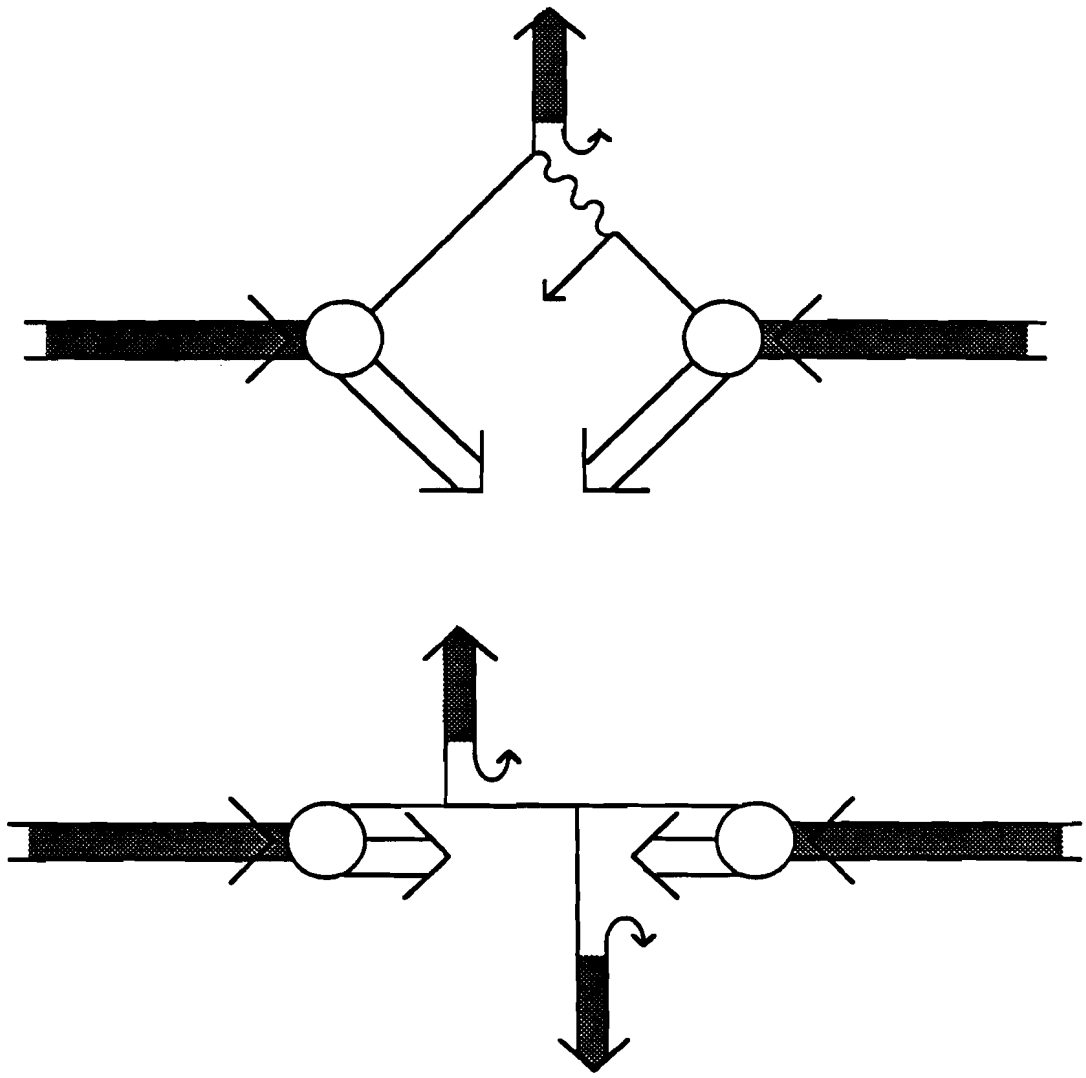

Figure 1.4.
Bias effects in high-p_t production
Possible bias in direction of trigger in high-p_t single hadron production (top)
No bias in symmetric hadron pair production (bottom)

1.2. Hadron Pair Production

The complications involved in jet analysis can be avoided by studying those events where most of the original scattered parton's momentum is carried by a single particle. This provides direct, if approximate, information on the parton interaction final state. For the purpose of analysis, the energy and momentum of the leading hadron in a selected jet is then taken to be the energy and momentum of the scattered parton. The requirement for detection can be reduced to a concentrated deposition of energy in a

hadron calorimeter. Several experiments have studied high p_t hadron production. These include Fermilab experiments 100A, 300 and 258 done at 200, 300 and 400 GeV/c^2, respectively, by the Fermilab-Chicago-Princeton collaboration, studying single hadron production[6-8]; the CCOR group at the CERN Intersecting Storage Ring (ISR) studying massive π_0 pair production[9]; the Fermilab E454 collaboration, studying dihadron production at 200 and 400 GeV/c^2[10]; and Fermilab experiment 605 studying hadronic singles and pair production[11].

The question arises as to how well the parton kinematics are reflected in a single high transverse momentum hadron. Experiments that have selected events on the presence of single "high-p_t" hadrons have found that these hadrons, on average, carry a momentum fraction (z) of over 80% of the of the entire jet[12]. Figure 1.5 shows results from the CCOR experiments done at the CERN ISR. This holds true for the production of single hadrons and hadron pairs. This is a consequence of the steep production cross section for jets as function of transverse momentum (p_t) (see Figure 1.6). For any given high-p_t hadron produced, the likelihood for it to have been part of jet of significantly higher p_t is small compared to that of a jet of comparable p_t. In probabilistic terms, the "sample space" of possible jets that a hadron of given p_t can belong to is much more heavily populated in the p_t bins nearest to its own value than in bins further down the spectrum. Of course, jets with "leading hadrons" of very low z are constantly produced and certain of these will have their leading hadron being identified as an event; but bin for bin these will contribute little to the overall cross section.

In narrowing consideration to these leading hadrons or "single particle jets", there is also a strong clue to the parton charge. For a certain range of interaction energies, the dominant scattering processes are those involving the "valence quarks", the fundamental constituents of hadrons. For protons and neutrons these are of 2 types or "flavours": up (charge +2/3) and down (charge -1/3). These charges are electric charges, so that a proton (uud) has a net electric charge of +1 and the neutron (udd) has a net charge of zero. Neutrino experiments at Fermilab have shown a strong correlation between the flavour of quark and the charge of the leading hadron that it "fragments" into - this gets stronger as the momentum fraction (z) carried off by the scattered hadron increases[13].

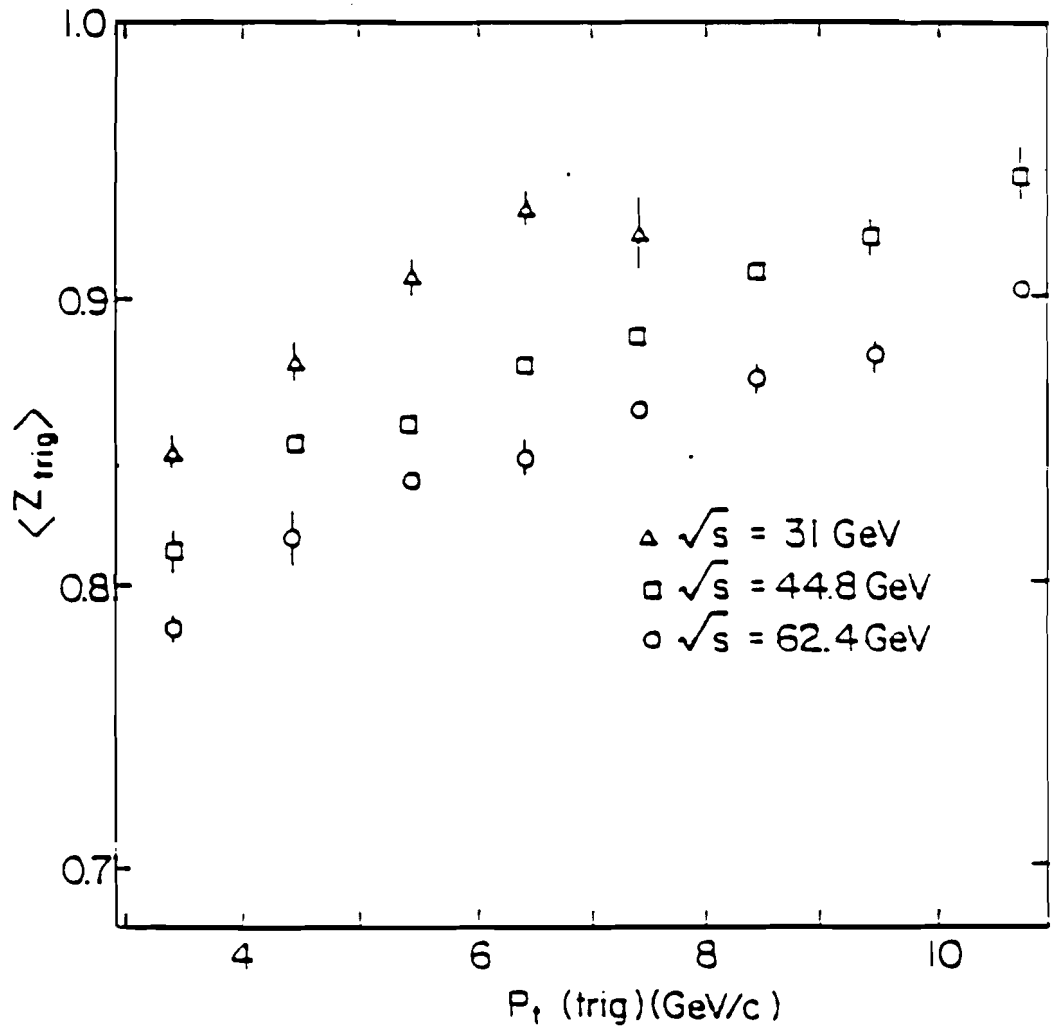

Figure 1.5

$\langle z \rangle$ versus p_t for inclusive π_0 production at $\sqrt{s}$ of 31, 44.8, and 62.4 GeV

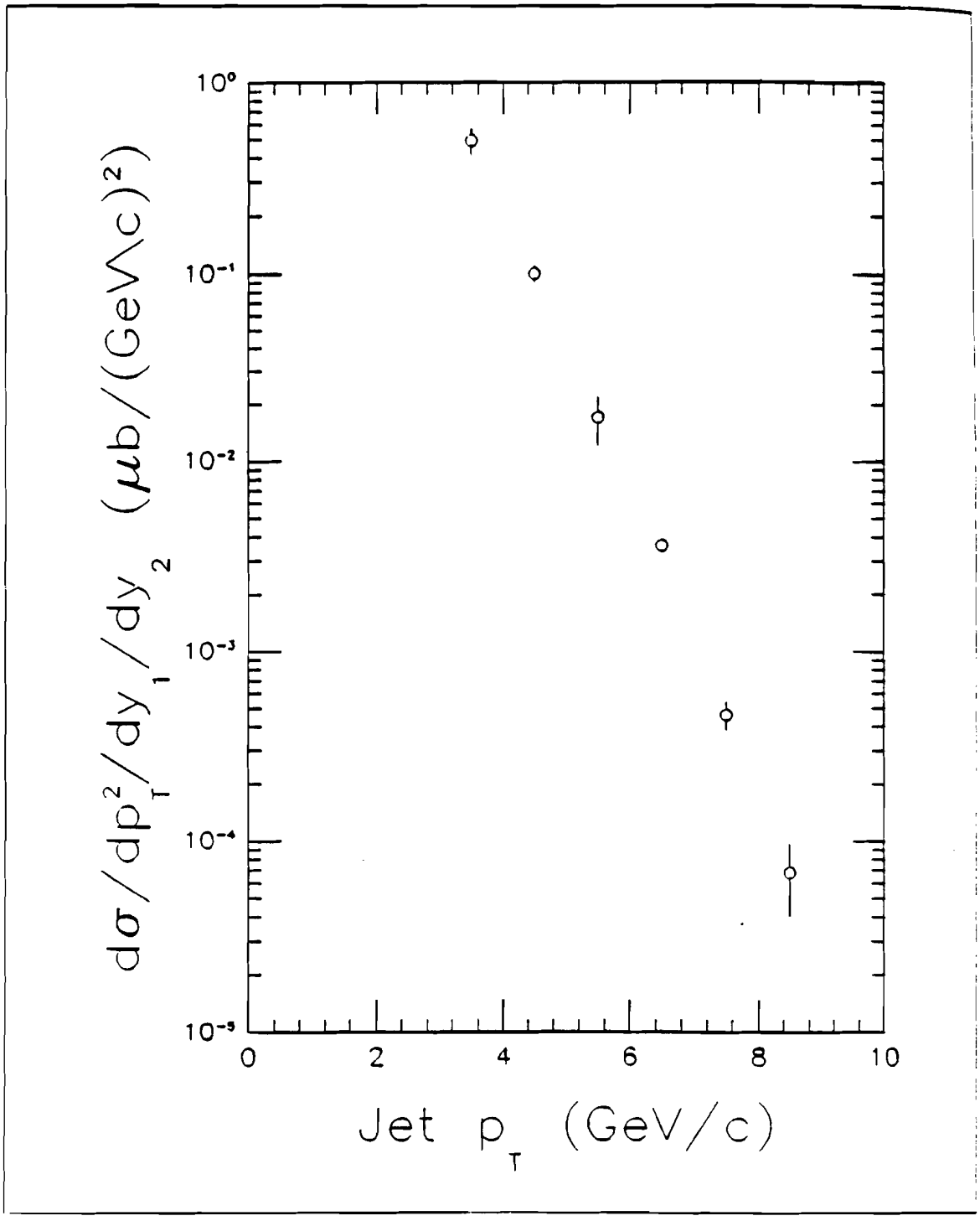

Figure 1.6
Di-jet data from E609 (Arenton et al., 1985)

Continuing with the earlier discussion, a Rutherford-like cross section should be expected in the limit of interaction lengths much smaller than the size of the nucleus. In fact, such behavior of the "di-jet" distributions have been seen at experiments done on the CERN pp machine[14] (see Figure 1.7). The simplest QCD predictions are that, to lowest order, the angular distribution of quark scattering is independent of the charge of the quark. None of the experiments mentioned above have looked for possible flavour dependence, so, to date, there has been no confirmation of this fundamental prediction.

1.3 Fermilab Experiment E711

An experiment to study charge dependence of angular distributions would need complete kinematic information of the final state of the parton scattering process, and this requires a "double-arm" experimental setup; that is, detection and reconstruction capability of both forward and backward (centre of mass) fragments from the parton scattering subprocess. A trigger requiring signals from 2 high-p_t particles also eliminates those particles whose transverse momentum arises from the intrinsic transverse motion of partons in nucleon, rather than from a genuine sub-nucleon hard scatter. Furthermore, we need a detector with large angular acceptance to reconstruct enough of the $cos\theta$ distribution to draw any meaningful conclusions comparing data with QCD predictions. Finally, of course, the apparatus should be able to identify the charge of the particle.

Fermilab Experiment 711 was proposed as an open geometry, fixed target experiment which would meet the requirements mentioned above to study the angular distribution of charged pairs of high-p_t hadrons. "Open geometry" simply means that the experiment has only a fractional geometric acceptance for all possible events. The design of E711 allowed for a $cos\theta$ acceptance from -0.6 to 0.6 in the centre of mass frame of the beam proton-target nucleon system. Run with a 800 GeV/c proton beam on various nuclear targets, E711 provided a symmetric event signal (or trigger) using energy deposition in 2 halves of a hadron calorimeter.

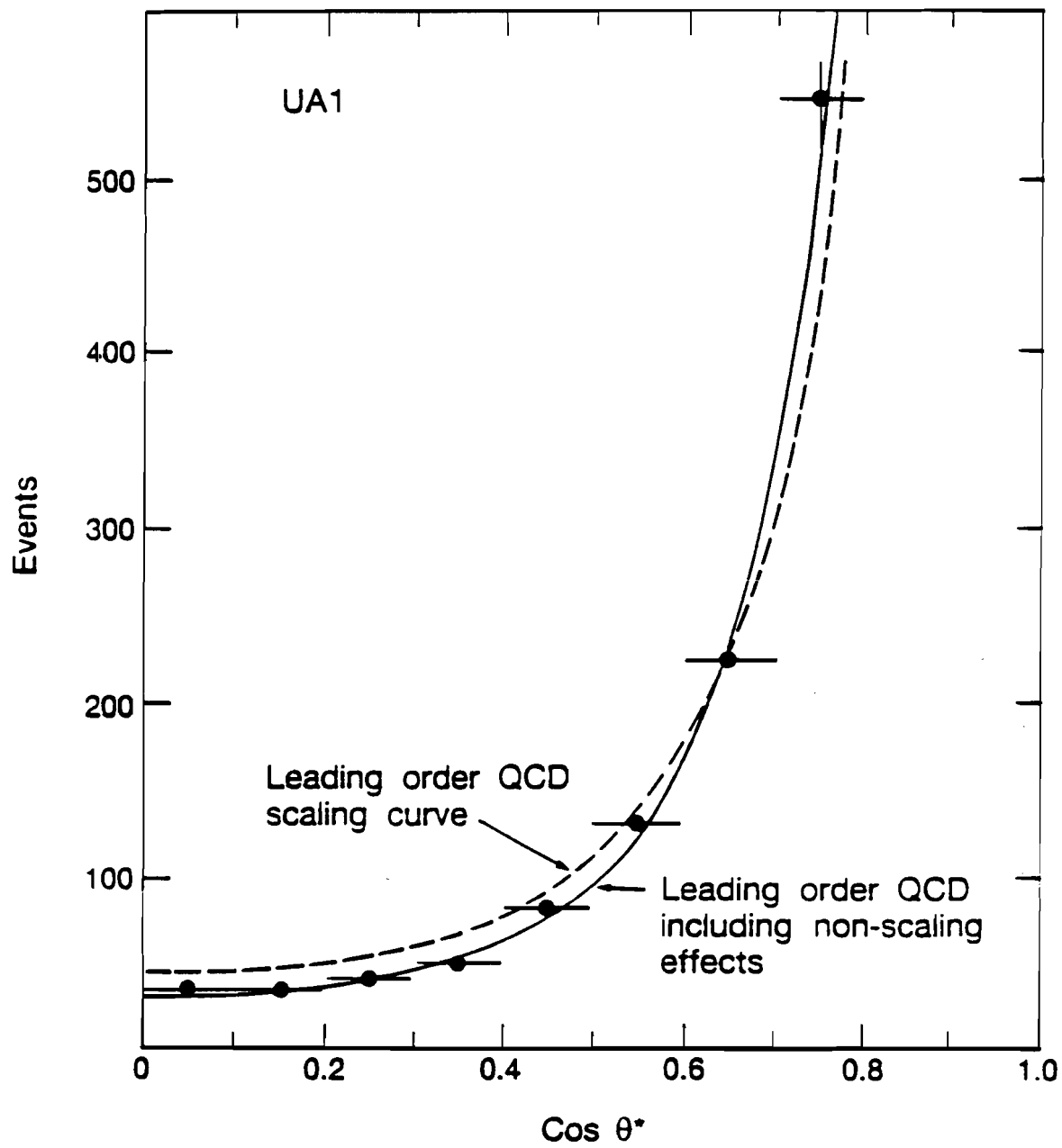

Figure 1.7
Angular distribution for two-jet events with mass of the two jets in the range of 150-250 GeV from the UA1 experiment

A magnetic spectrometer provided the momentum and charge information. E711 was performed in the Neutrino East beamline at Fermilab. An engineering run took place in 1985, and the data this dissertation describes were taken from November of 1987 to February of 1988.

This experiment compliments another done at the ISR (CERN) by the CCOR collaboration[15] where the the mass and angular dependence of high-p_t π_0 pairs were studied (Figure 1.8). Among recent experiments studying high-p_t hadron pairs, E711 is unique in its large acceptance for both like-sign, and opposite-sign charge states. At a c.m. energy similar to that of the ISR (38.7 GeV/c^2) and a good order of magnitude lower than recent CERN $p\bar{p}$ experiments, it is also a test of the lower energy limits of perturbative QCD theory. What follows is a description of the experimental setup and of the analysis leading to mass cross sections and $cos\theta$ cross sections. Chapter 6 has further discussions of QCD pertinent to the results.

CHAPTER 2

APPARATUS

The E711 detector was designed to handle the problems inherent in studying "massive" hadron pairs, with the acceptance necessary for acquiring decent angular distributions. The steep hadron production cross section with respect to p_t (see Figure 1.5) made it necessary for the detector to accept high enough rate of nucleon interaction to yield sufficient number of events in the mass range of interest. The "mass" of a hadron pair consists of the energy, both kinetic and rest mass, of the pair in its centre-of-momentum frame. The kinematics of hard scattering sub-processes are identical to those of a two-body decay, so a pair of high transverse momentum particles is often referred to as a "massive state". The detector had to discriminate the "high mass" pairs from the far greater number of lower mass events, and provide accurate charge and momentum information

2.1 Design

Figures 2.1 and 2.2 show illustrations of the detector looked at from the top and side views. The active parts of the apparatus are separated symmetrically above and below the proton beam line. A "beam's eye" view of the calorimeter is shown in Figure 2.3. The geometry of the calorimeter determined the basic acceptance for particles for the experiment. The two calorimeter halves were segmented vertically, and each covered an azimuthal range of $\pm$ 25.3^{o}. The inner and outer edges of the calorimeter were calculated to subtend an angle of 20-100 mr from the target which corresponds to a range of -0.6 to 0.6 $cos\theta$ relative to the beamline in the beam-target centre-of-mass frame.

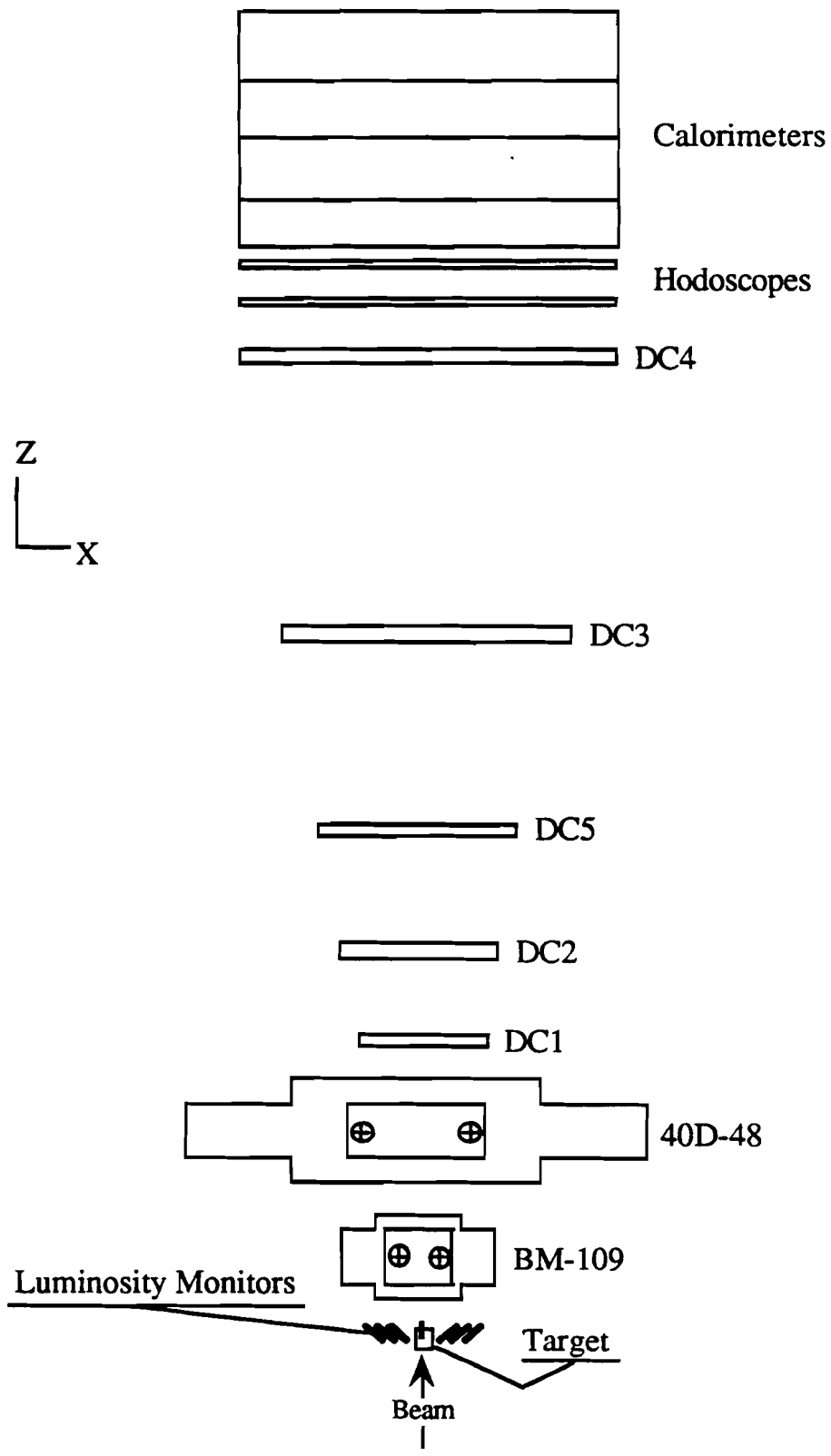

Figure 2.1
Plan view of E711 detector.

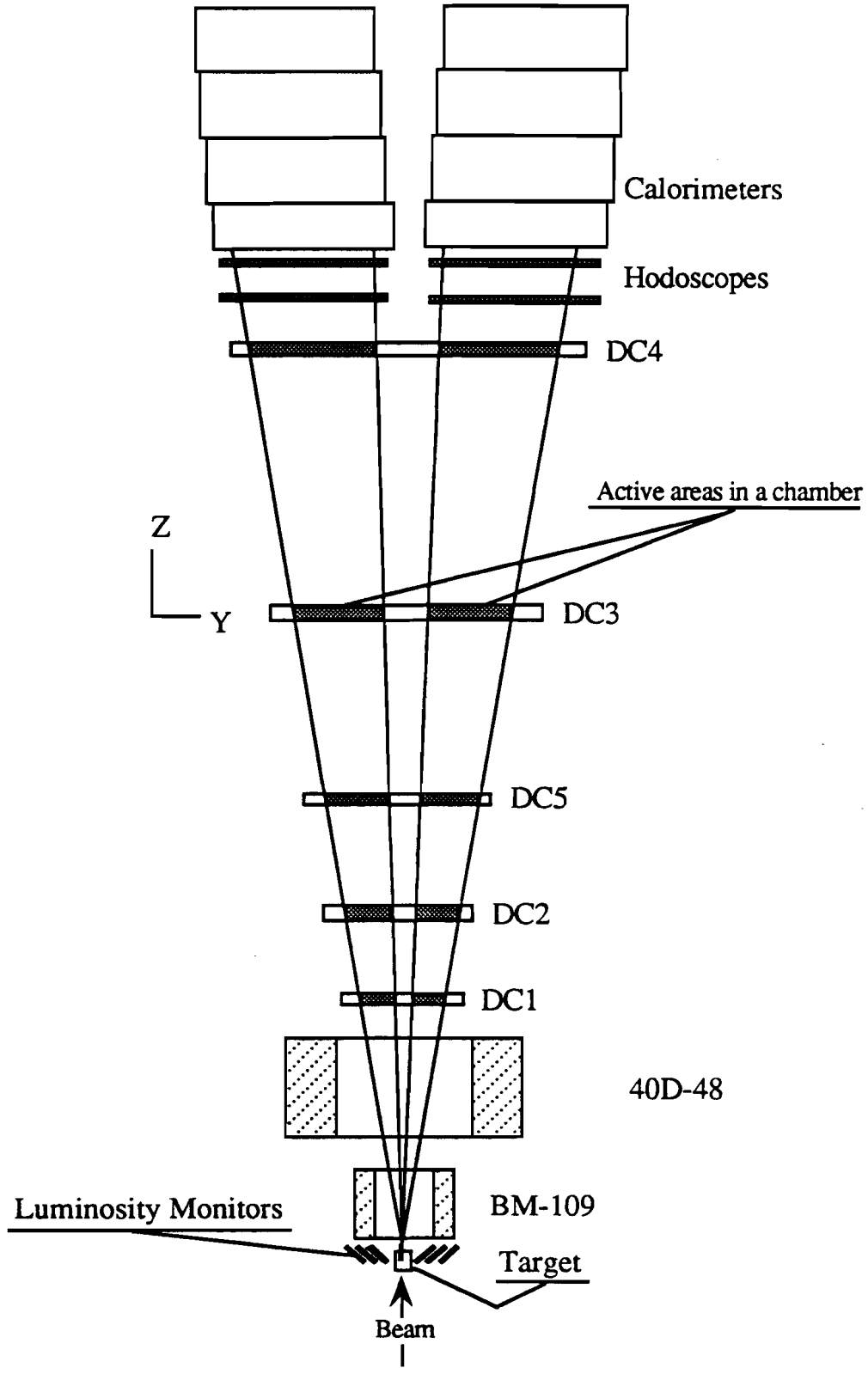

Figure 2.2
Side view of E711 detector.

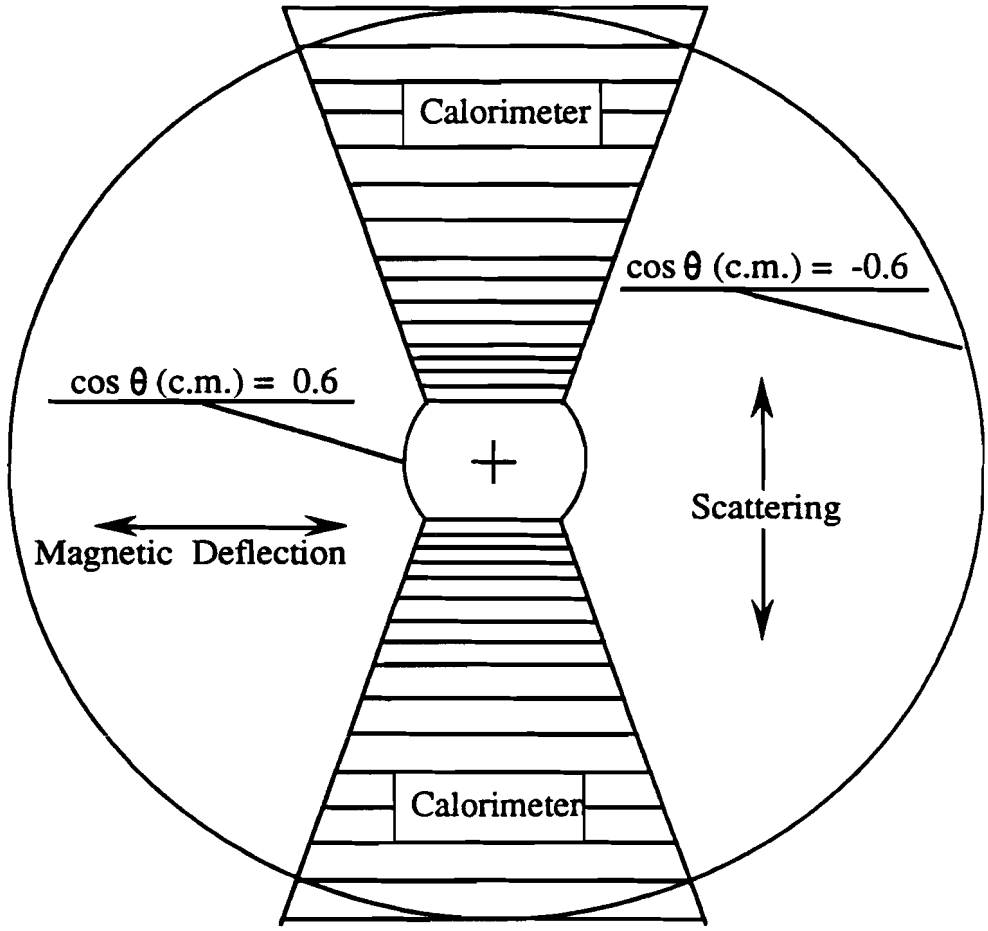

Figure 2.3
"Beam's eye" view of E711 calorimeter

From the entrance of the beam into the lab, the apparatus of the experiment consisted of beam monitoring devices, metal target, luminosity monitors, two magnets, five stations of drift chambers, two planes of hodoscopes, two planes of proprotional tubes and a calorimeter. The hodoscopes, proportional tube planes and calorimeter each consisted of two identical halves, symmetric about the beamline. With the region around the beamline desensitised in all the chambers, protons not interacting with the target could pass between the two arms of the detector allowing the the experiment to take a rate of 10^7 to 10^8 protons/sec. This was necessary to observe sufficient numbers of high mass events. The calorimeter signalled an event when each half detected a high-p_t particle simultaneously. Particles coming from interactions in the target went through a vertical

magnetic field. The two magnets imparted a net p_t kick of 1.16 GeV/c in the horizontal direction to all charged particles, with the low momentum particles swept out of the detector. This horizontal deflection, and the particle trajectory information from the chambers, was used later on in the momentum calculation. With much of the particle's original p_t in the vertical direction, the momentum measurement and the calorimeter event selection were effectively decoupled. The targets' small size gave a good approximation to the vertex position for tracks upstream of the magnets, obviating the need for chambers before the magnets. This overcame a major obstacle to high rate capability, and simplified the track reconstruction.

2.2 Beam Line

The experiment was run on the NE (Neutrino East) beamline that directed 800 GeV protons in 20 second spills to the E711 target. The protons flux was resolved into "buckets" (bunches in time), approximately 2 nanoseconds long at intervals of 18.2 nanoseconds. This reflected the RF-driven acceleration of the Tevatron. The beam was focussed such that its transverse profile was roughly Gaussian with a sigma that was typically ~0.4mm in the horizontal direction. During the 1987-1988 run the beam flux to the experiment averaged 2.5×10^7 protons/sec (5×10^8 protons per spill).

2.2.1 Beamline Elements

From the switchyard, the protons were transported to Lab G using a variety of magnets, splitters and collimators. Figure 2.4 shows a layout of the NE line into Lab G. The devices directly controlled by E711 were:NEBE (horizontal deflection dipoles); NEBV (vertical deflection dipole); NEBQ2 (horizontally defocussing quadrupole); NECQ (horizontally focussing quadrupole); NECH (horizontal deflection dipole); NEEAN1 and NEEAN2 (dipoles). These last were used as analysing magnets for the momentum reconstruction of charged particles through the E711 detector. NEBV and NECH were the

principle elements used in positioning the beam onto the target. Target scans were performed by changing the deflection of NECH such that the beam was swept across the target to determine the beam profile and target interception fraction.

2.2.2 Beam Monitoring and Luminosity

To measure the total proton flux into the experiment, an ion chamber (NECIC) was positioned at the entrance of the beamline into the experimental area. The number of protons interacting with the target was measured with a system of 4 luminosity monitors (labelled UW, UE, DW DE) placed symmetrically about the target at 90° to the beamline. Each monitor consisted of 3 counters in coincidence, telescoping toward the target. This gave 4 independent measurements of the proton-target interaction rate. The output from the ion chamber and luminosity monitors were used to calculate the total luminosity, or normalisation, for the cross sections. The luminosity calculation, and the calibration of luminosity monitors and the ion chamber are discussed in chapter 3.

2.3 Targets

The high intensity of beam-target interactions necessary for a sufficient data sample precluded the use of chambers upstream of the magnets. Therefore the targets needed to be small enough to approximate the scattering vertex. They were mounted on a narrow stand whose base was attached to micrometer-adjustable plate for accurate placement in the beamline. Positioned edgewise to the beam, the width in x was smaller than the beam spot, necessary to define the vertex in the x coordinate, since the magnets deflected particles in the horizontal direction. As the y component of a charged particle's momentum was uneffected by the magnetic field, the target width in y was not critical. The length in z (along the beam) for each target was about 10% of an interaction length for its material. This was the compromise to limit possible multiple scatterings while providing sufficient interaction rate. Table 1. 2 summarises target characteristics.

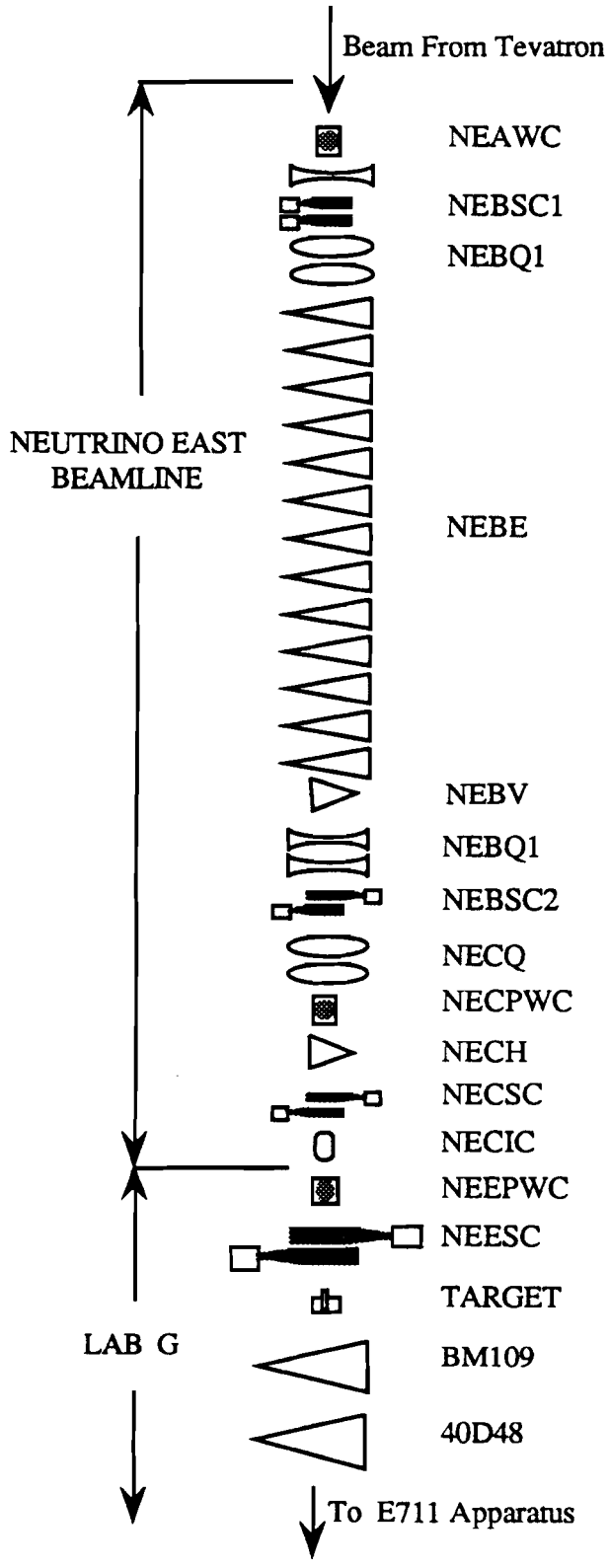

Figure 2.4
The E711 beamline elements

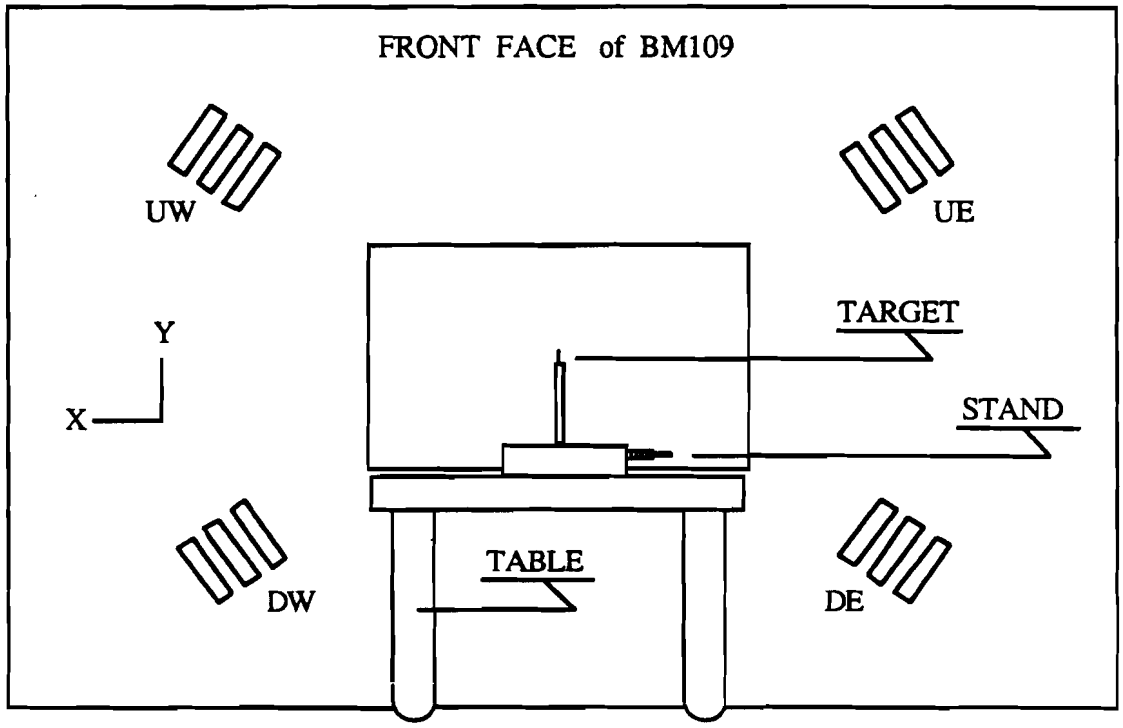

Figure 2.5
Target and luminosity monitor setup

Target	x (cm)	y (cm)	z (cm)	λ	# of Protons	# of Neutrons
Be	0.10225	2.5	4.066	0.0999	4	5
Al	0.08357	2.5	3.951	0.1003	13	14
Fe	0.04892	2.5	1.670	0.0997	26	30
W	0.10211	2.5	0.956	0.9970	74	110

Table 2.1
Target characteristics

Four different metal targets were used during the run: beryllium, aluminum, iron and tungsten. Data were taken using the different targets to yield information on the possible atomic number dependence of the dihadron production cross sections. That analysis is described elsewhere[16], and yielded a small dependence on the atomic number: A^{α}, where α was equal to 1.05 ± 0.012

2.4 Magnets

Immediately downstream of the target, two analysing magnets (Fermilab magnets BM109 and 40D48) imparted a sideways momentum kick of 1.16 GeV/c to charged particles that, together with the drift chambers, constituted the momentum spectrometer of the apparatus. The magnet currents were set to 2000 amps and 4500 amps, for a peak field of 10 kG and 8 kG in the BM109 and 40D48, respectively. The 40D48 had dimensions 2.0 x 2.5 x 3.3m with an aperture of 50.8 x 43.3 x 182.9cm; for the BM109, 2.7 x 2.5 x 3.8m and 101.6 x 93.7 x 122.6. These are labelled NEEAN1 and NEEAN2 in the beamline schematic (see Figure 2.4).

Measurement of the magnetic field was done using the Fermilab ZIPTRACK measuring system[17]. Three mutually perpendicular coils were mounted on a cart that moved on aluminum tracks set parallel to the z direction inside the magnets. With the magnets turned on, the cart was moved through the magnets, and the current induced in the coils integrated and digitised using an analogue-to-digital converter (ADC). A three-dimensional grid of magnetic field values was thereby obtained to within 1% accuracy. Figure 2.6 shows a plot of the magnetic along the z direction produced by interpolating the ZIPTRACK data. Another measurement of the magnetic field using a Hall probe was consistent with that of the ZIPTRACK method.

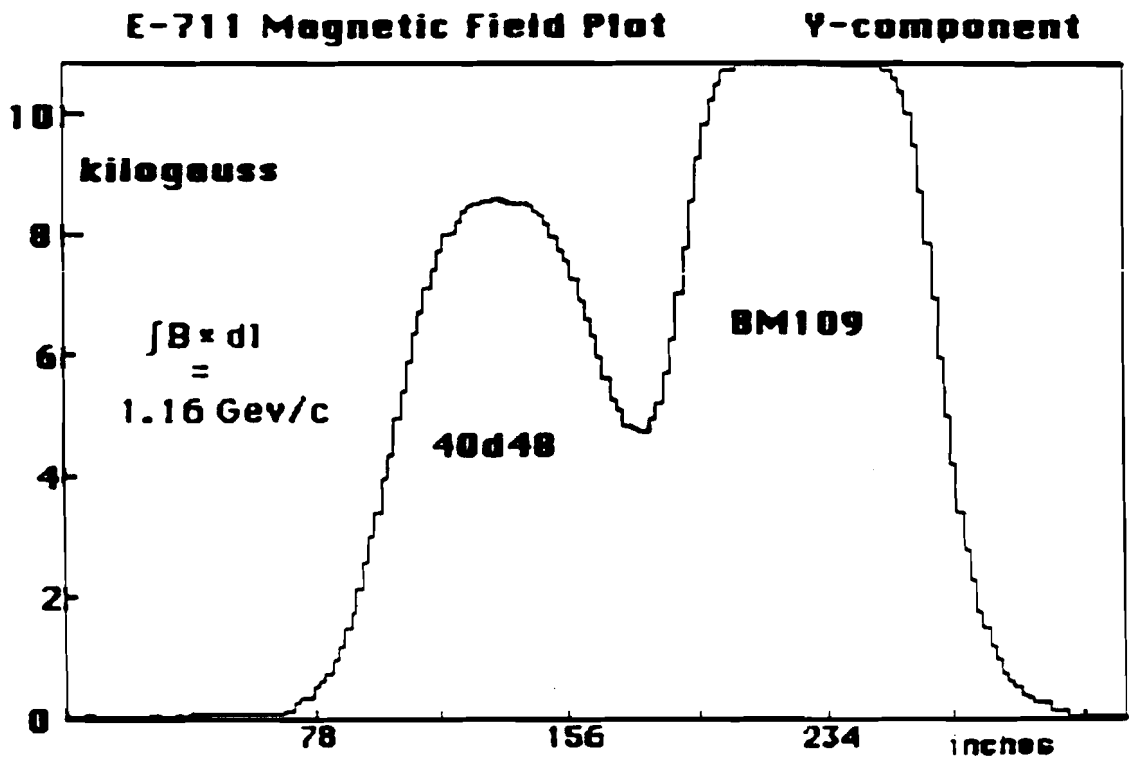

Figure 2.6
Data from ZIPTRACK magnetic field measurement

2.5. Drift Chambers

The drift chambers provided the information on particle tracks that, together with the vertex constraint given by the small target and the p_t kick of the magnets, were used in reconstructing particle momenta. There were five stations of drift chambers, each with four anode planes containing sense wires perpendicular to the beam direction. These four planes provided information on the particle's position along four different axes: y (vertical), x (horizontal), u and v (at 10° and -10° to the x axis respectively).

The drift chamber stations consisted of these anode (signal) planes as well as cathode (high voltage) wire planes and ground wire planes. These were supported inside aluminum frames, sealed with mylar covers on the faces, through which a neutral gas mixture was circulated. When a charged particle passed through a chamber, the gas atoms were ionised, and the electrons drifted toward the closest sense wire in each anode plane. The high voltage planes provided the electric field necessary to move the electrons along toward the sense planes. Near the wire, the increasing ion velocity initiated multiple ionisation processes (gas amplification), and a large enough number of electrons gathered onto a given sense wire to form a detectable signal. Each sense wire had on one end a preamplifier circuit that enhanced the signal by ~ 20 X. This allowed the chambers to be run at a lower voltage than would normally be the case, enabling them to withstand the high beam intensity. The signals from the preamplifiers were sent on to an amplifier/discriminator, and from there to a time-to-digital converter (TDC). The interwire position of the charged particle was calculated offline using the TDC information.

The high voltage wires in each drift station chamber were strung horizontally, so that a central region in each station could be deadened vertically around the beam. This allowed the beam not interacting with the target to pass through the apparatus, allowing the experiment a high rate capability. A region of intermediate voltage was set between the

"live" cathode wires and the "dead" cathode wires to cut down the electric field gradients. This transition region was typically 200 V lower than the live region, with the "dead" region being about the same amount lower than the transition region. More details of the chamber voltages and construction are included in Appendix 2.

2.6 Calorimeter and Hodoscopes

2.6.1 Design

The combined system of calorimeter and hodoscope planes provided the double-armed trigger to the read-out system of a possible event. Figures 2.7 and 2.8 show detailed illustrations of the calorimeter from "beam's eye" view and the side view of the calorimeter and hodoscopes, respectively. An event signal, or "trigger", required that a high-p_t particle be detected in each arm of the apparatus.

The geometry of the calorimeter is such that most of the transverse momentum of a detected particle is in the vertical direction. The calorimeter's vertical segmentation into 16 modules enabled its response to be made roughly proportional to p_y ($\sim p_t$). The response of each module was set to be proportional to the average value of the $\sin \theta_y$, where θ_y was the polar angle between the beam line and the line connecting the target and the given module. Given that $E \sim p$ for relativistic particles (in natural units where c is set equal to 1), the signal $E \times .(\sin \theta_y)$ made a good approximation to p_t. The invariant mass of the pair can be approximated by $M \sim p_{t1} + p_{t2}$ for "symmetric" pairs (those produced back-to-back in the proton-nucleon c.m. frame), so the calorimeter could provide a reasonable threshold for massive pairs.

The hodoscope (*hodos:*"path" or "road" in Greek) consisted of two planes of scintillation counters (labelled *HF* and *HB*, front and back). These were segmented in the vertical direction with each module's signal amplified by a photomultiplier tube at either

end. The simultaneous firing of corresponding front and back hodoscope modules indicated the path of a charged particle through the detector. Signals from the hodoscopes were incorporated into the event trigger to select out those massive pairs in one of three charge states: +-, ++, --.

The calorimeter measured the energy of an incident particle by causing the particle to disperse its energy, through inelastic nuclear interactions, into a shower of lower energy particles. The E711 calorimeter was constructed from modules composed of alternate layers of metal and scintillator for particle showering and detection, the standard "sampling calorimeter". Several layers of scintillator tapered into a light guide and photomuliplier tube on either end of each module (see Figure 2.9). There were 4 sections of modules in the longitudinal (z) direction in each half of the calorimeter. The first section (*EM*) was an electromagnetic calorimeter and consisted of alternating lead and scintillator for a total of 29.7 radiation lengths. This insured that all photons and electrons from the target interactions were completely absorbed. The remaining 3 sections (*H1*, *H2*, *H3*) consisted of iron and scintillator layers, composing the hadronic portion of the calorimeter. The majority of hadron showers were contained in these sections. The 4 sections together gave the each calorimeter half a total of 9.24 nuclear interaction lengths, which guaranteed near total energy absorption for hadrons. The quick response of the photomultiplier tubes (PMT's) made for the fast triggering necessary for taking high rates of target interaction.

The position of the corresponding modules in the hodoscopes and calorimeter z sections formed a rough projection toward the target. The various combinations of signals from these modules that triggered the read-out system are explained in the next chapter.

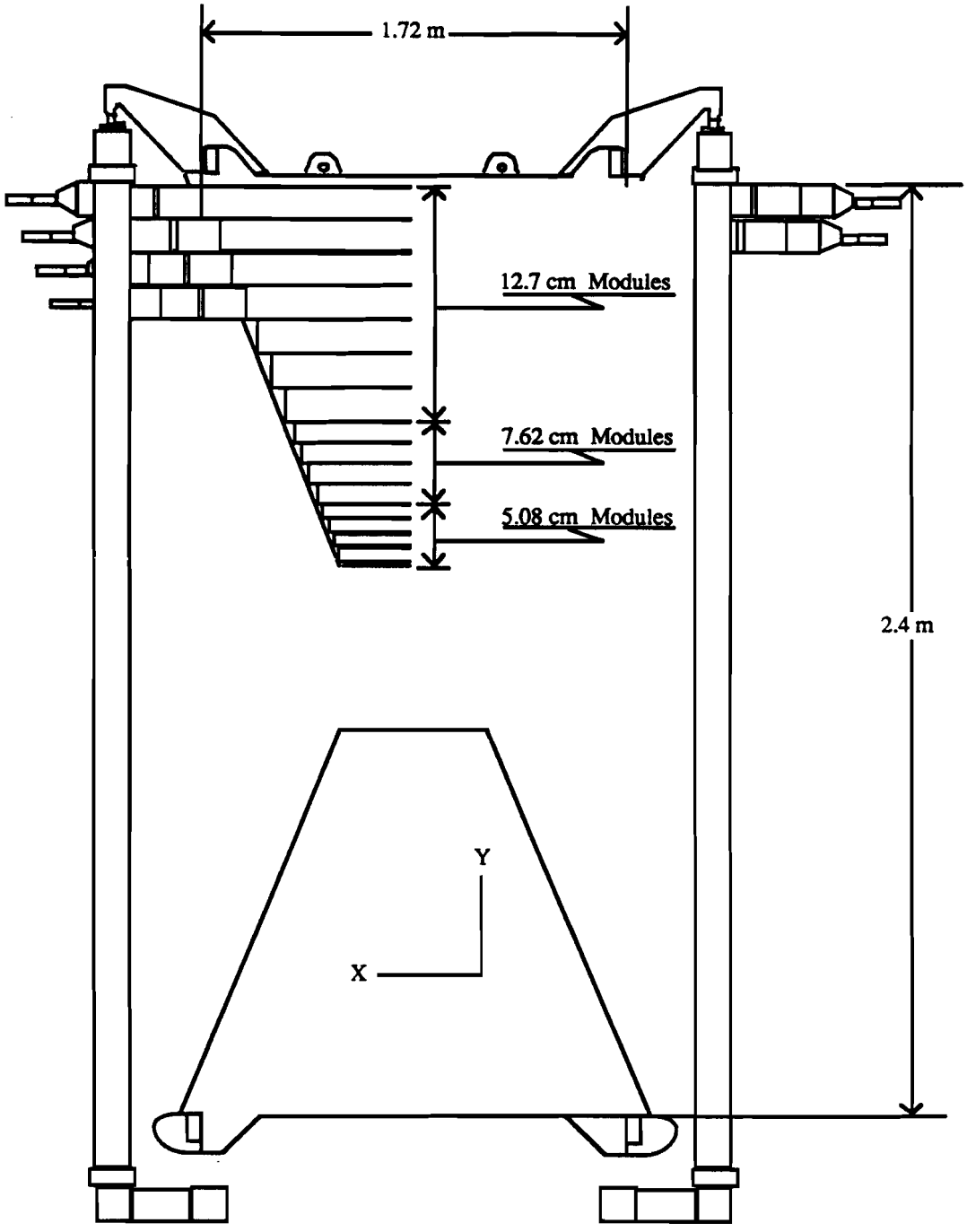

Figure 2.7
Front view of the E711 calorimeter

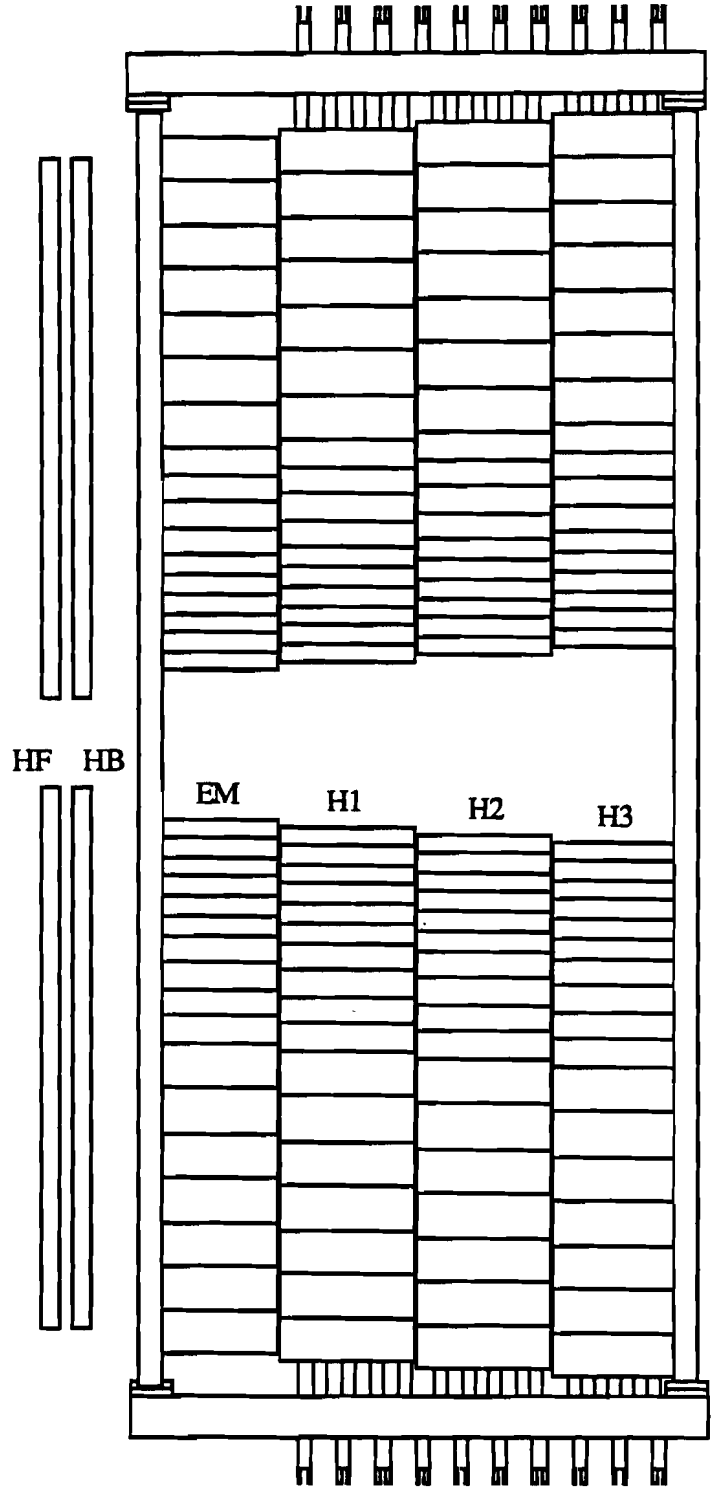

Figure 2.8
Side view of the E711 calorimeter and hodoscopes

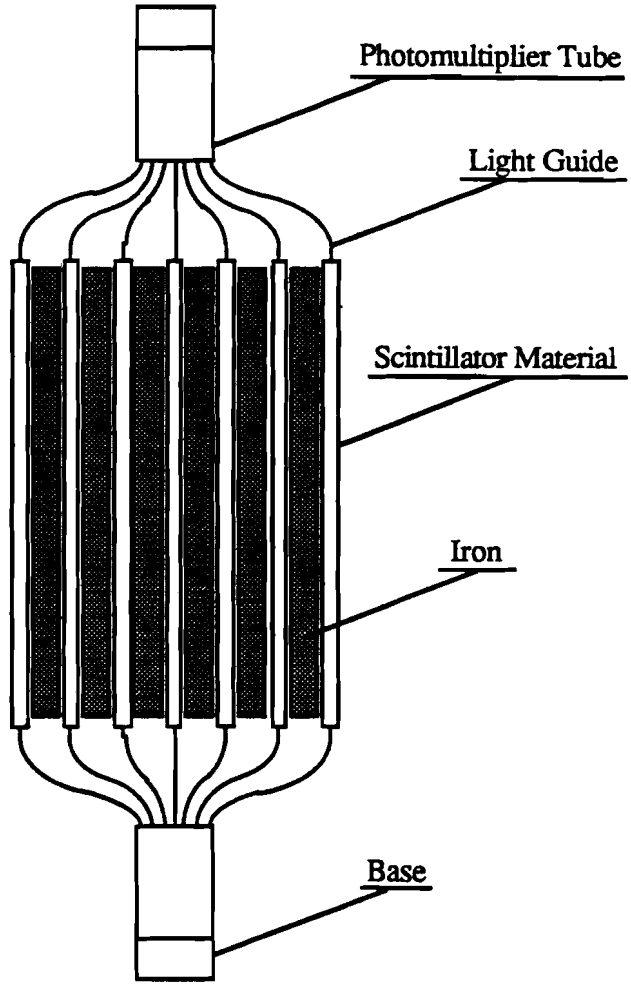

Figure 2.9
Example of an E711 calorimeter module

2.6.2 Calibration

Before and throughout the data taking run the relative gains of the PMTs were adjusted by calibrating on muon energy deposition in the calorimeter. Muons with energies between ~ 0.4 and 4-500 GeV are close to being "minimum ionising", that is, they lose energy by ionisation at an approximately constant rate while traversing the calorimeter. Gammas and electrons of comparable energy, in contrast, lose their energy rapidly in matter through a cascading shower of interactions. The near uniformity of energy loss for muon traversing the calorimeter allows for the relative calibration of different length detector elements. Because the difference in the magnitudes of muon and

hadron energy deposits were greater than could be accommodated by the range of the digitising electronics, the calorimeter PMTs had two gain settings. The high gain was turned on for the muon runs (the setup for muon runs is described below), and the lower gain for regular data taking.

The hodoscope PMT voltages were first set to the same high value and then their gains adjusted by a variable resistor in the base so that each module gave the same response to single muon passing through. The pulse height was chosen so as to insure that it fired the corresponding electronic module in the trigger electronics.

The calorimeter PMT's were set by varying the high voltage in the high gain mode so that they gave a uniform response to muons. In this manner, the gains of the various calorimeter sections in z were set in a ratio of .44 : 1 : 1 : 1, reflecting the ratios of the peak of the muon energy deposition. The low gains were then adjusted to be proportional to *sin* θ_y of of each module from the target, making the module's response proportional to the transverse energy of an incoming hadron. *Sin* θ_y is defined by

$$\sin\theta_y = \frac{y}{\sqrt{y^2 + z^2}} \tag{2.6.1}$$

where y is the vertical position of the module from the beam line and z is its distance down the beamline from the target. The ratio of high and low gain for a given module is

$$\frac{High\ \ gain}{Low\ \ gain} = \frac{C}{\sin\theta_y} \tag{2.6.2}$$

The constant C was chosen to give an adequate size pulse to the trigger electronics. To set the low gains, light-emitting diodes (LEDs) were placed toward the face of each PMT to measure test signals and thereby set the ratio. These were set manually by switching from high gain to low gain, measuring the response of the LED using a voltmeter. Appendix 1 describes the absolute calorimeter calibration.

2.7 Muon Trigger

Data for calorimeter calibration and alignment were taken periodically during the run with a separate trigger on muons. The trigger setup consisted of three sets of scintillation counters in both top and bottom arms of the detector. A muon trigger was defined as a three-fold coincidence of these counters in either arm. One set of counters were placed between chambers 1 and 2 to insure that the muons passed through the sensitive regions of the chambers. Two sets of vertical counters were placed in front and in back of two sets of steel absorbers that were in place behind each calorimeter half. The length of the counters insured that muons could be detected in the entire vertical span of each calorimeter half.

The trigger required only a single muon in either arm for the purposes of calibration. The vertical alignment of the calorimeter modules in the *H1*, *H2* and *H3* longitudinal sections of the calorimeter was done using survey measurements of the front modules (*EM*), and the reconstructed y and z positions of the muon when the electronics detected a pulse from the downstream modules. Figure 2.10 illustrates the detector configured for triggering on muons.

Module Number	EM	H1	H2	H3
1	26.1	20.8	20.1	19.4
2	18.6	18.0	17.5	16.9
3	16.3	15.9	15.4	15.0
4	14.6	14.2	13.9	13.5
5	13.1	12.8	12.6	12.3
6	11.7	11.5	11.3	11.0
7	10.4	10.2	10.0	9.84
8	9.32	9.16	9.02	8.88
9	8.45	8.33	7.54	7.44
10	7.53	7.43	6.97	6.88
11	6.62	6.54	6.18	6.17
12	5.91	5.85	5.56	5.51
13	5.34	5.29	5.05	5.01
14	4.87	4.83	4.63	4.59
15	4.47	4.44	4.27	4.24
16	4.14	4.11	3.96	3.93

Table 2.2
Nominal photomultiplier tube gain settings

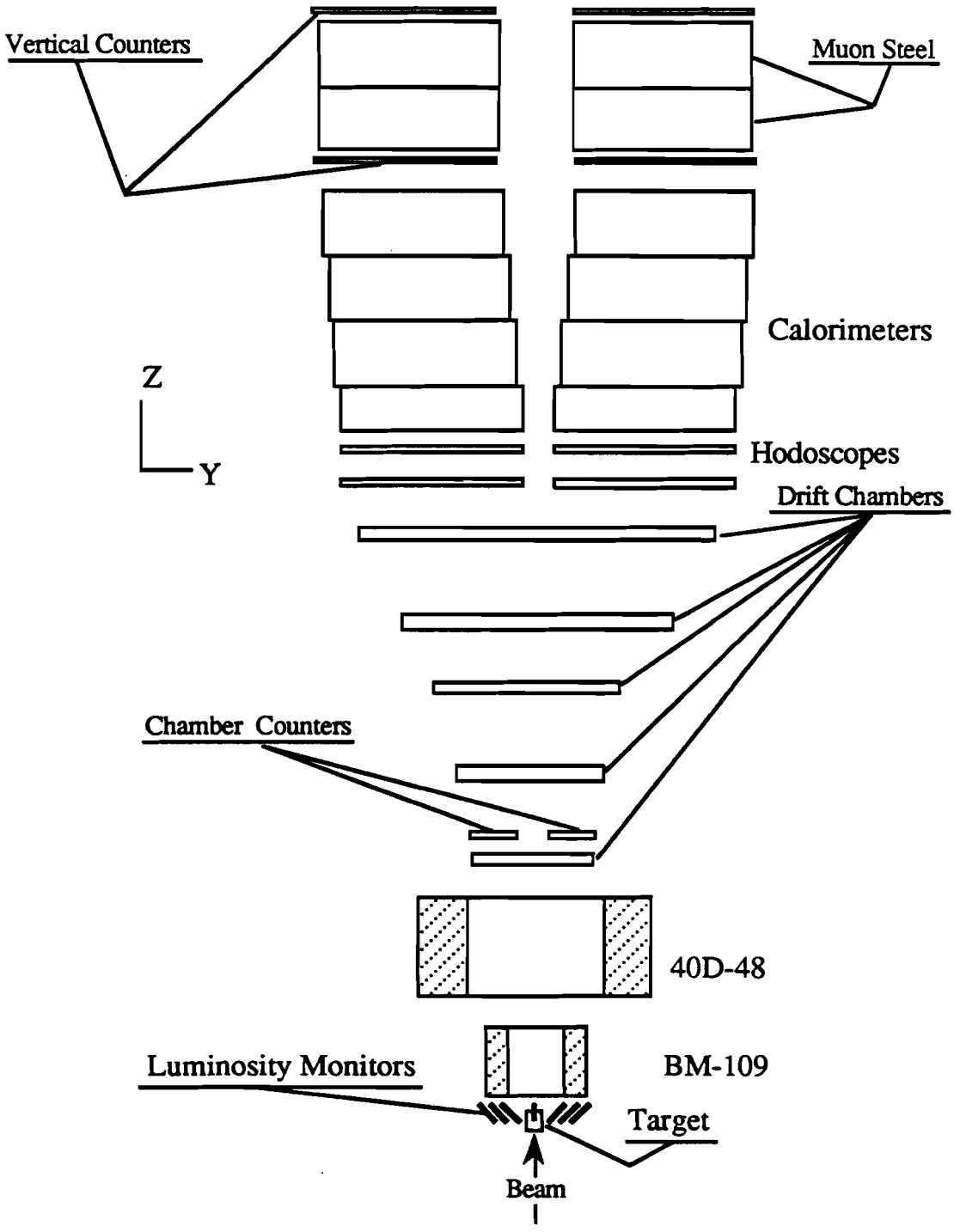

Figure 2.10
Muon trigger setup

CHAPTER 3

APPARATUS TRIGGERING AND DATA ACQUISITION

The actual running of the experiment for data collection was an orchestration of various detector elements, electronics, readout system and on-line computer synchronised with the cycle of proton spills from the Tevatron. This section gives an account of all aspects of this amalgamation of activity.

3.1 Organisation

The Fermilab accelerator delivered 20 seconds of continuous proton beam during every one minute spill cycle. Reference signals from the accelerator were received by the experiment's control electronics at 6 different times during spill cycle. These were used to set the timing for the various operations involved in the data acquisition. In particular, the experiment was "enabled" or made data-ready upon receipt of such a signal by the control electronics. Scaler resetting and pedestal triggers were also timed in this way. These are described more fully below.

Once the experiment was "live", signals from the detector elements could be received by the trigger electronics. Hodoscopes and calorimeter pulses were routed through a signal splitting panel, where one set went off to the logic circuits of the electronic trigger and the other set to the data read-out modules. The read-out electronics consisted of all the pulse digitisers, or analogue-to-digital converters (ADC's), the chamber drift time digitisers, or time-to-digital converters (TDC's), and all scalers (electronic counters).

Scaled quantities included the sums of all triggers and logic counts, luminosity monitor counts and detector and beamline magnet currents. Signals from the front hodoscopes set the event reference time (t_0) to the TDC's. The TDC's and ADC's were recorded for each event, while the scalers were read only at the end of each spill.

All the read-out modules were mounted into CAMAC crates, which provided them with power and connection to a "branch highway", or data bus into a PDP-11 computer. A controller in each crate received read-out commands and addresses from the PDP and transferred data from the modules onto the branch highway. Seven of these crates ran off of a single highway. A Jorway branch "T" allowed data to be sent to both the PDP-11, which did the actual data recording to tape, and to a VAX 780 which ran online analysis and monitoring programs.

3.2 Trigger Design and Operation

Several levels and types of trigger were constructed from the hodoscope and calorimeter modules. This was made necessary by the specific requirements for an event described earlier. The response of the calorimeter to an incoming particle was made proportional to $\sin\theta_y$. With $E_y \sim E\times\sin\theta_y \sim p\times\sin\theta_y \cong p_t$, a mass trigger, where $M \cong p_{t1}+p_{t2}$, can be formed from the combination (or, in boolean terms, "anding") of one of these signals from each side of the calorimeter. The number of approximations used above does not discredit this mass reconstruction, since it is used primarily as a trigger signalling a possible event. All the kinematic reconstruction was done with information from the wire chambers, though a certain rough comparison can be made between chamber and calorimeter information. However, the steepness of the production cross section for massive hadron pairs makes it important that the trigger be efficient for high mass pairs without swamping the data sample with low mass events.

3.2.1 The P trigger Elements

Setting the calorimeter response proportional to $\sin \theta_y$ required the vertical segmentation of all longitudinal (z) calorimeter sections. The resulting longitudinal modules are too narrow in the vertical direction to contain a single particle shower, so segments large enough to contain a typical hadron shower were formed in the logic circuits by combining the pulse heights from four adjacent modules in all four calorimeter z sections. Pulse heights from both ends of a given module were used so that the response would not depend on shower position in x due to attenuation of the signal travelling through the scintillator. The phototube signals are labelled EME, EMW, H1E, H1W, and so on, for each of the 16 modules in both top and bottom calorimeters. The projective geometry of the module placement in each longitudinal calorimeter section made it possible for the entire energy deposition of a particle from the target to be contained in one of these segments. The sum was discriminated so that p_t was greater than 2 GeV/c^2. This formed the trigger element for a high-p_t particle labelled "P". Figure 3.2 shows the composition of an entire segment and the corresponding electronics schematic. There were twelve such trigger elements from each calorimeter half, overlapping so that the $\sin \theta_y$ response could be retained. For a given segment

$$P_j = \sum_{i=j+1}^{j+4} (EME + EMW + H1E + H1W + H2E + H2W + H3E + H3W)_i$$

where j denotes the segment number and i denotes the modules the segment comprises .

3.2.2 The Q and Q • P Trigger Elements

The hodoscopes signalled the presence of a charge particle and set the relative time of the event. Pulse heights from either of two vertically adjacent front hodoscope modules (HFE and HFW) were discriminated, to insure the presence of a minimum

ionising particle, and put into coincidence with an RF pulse from the accelerator. These, in turn, were put into coincidence with the discriminated signals from either of two vertically adjacent back hodoscope modules (HBE and HBW) to form a charge, or "Q", trigger element.

$$Q_{j=i-2} = (HFE \bullet HFW)_i + (HBE \bullet HBW)_i OR (HFE \bullet HFW)_{i+1} \bullet (HBE \bullet HBW)_{i+1}$$

There were 12 such elements in each arm of the detector. Each Q trigger corresponded to a calorimeter P segment trigger, and the charged high-p_t trigger element Q• P was formed by their coincidence. Table 3.1 lists the module composition of the trigger segments. Figure 3.1 illustrates an example of a P and Q • P trigger element.

Q•P TRIGGER SEGMENT	CALORIMETER MODULES	HODOSCOPE ELEMENTS
1	2-3-4-5	3-4
2	3-4-5-6	4-5
3	4-5-6-7	5-6
4	5-6-7-8	6-7
5	6-7-8-9	7-8
6	7-8-9-10	8-9
7	8-9-10-11	9-10
8	9-10-11-12	10-11
9	10-11-12-13	11-12
10	11-12-13-14	12-13
11	12-13-14-15	13-14
12	13-14-15-16	14-15

Table 3.1
Q•P Trigger Segment Composition.
Modules are numbered from those closest to the beam.
Each half of the trigger (top and bottom) have the 12 segments listed

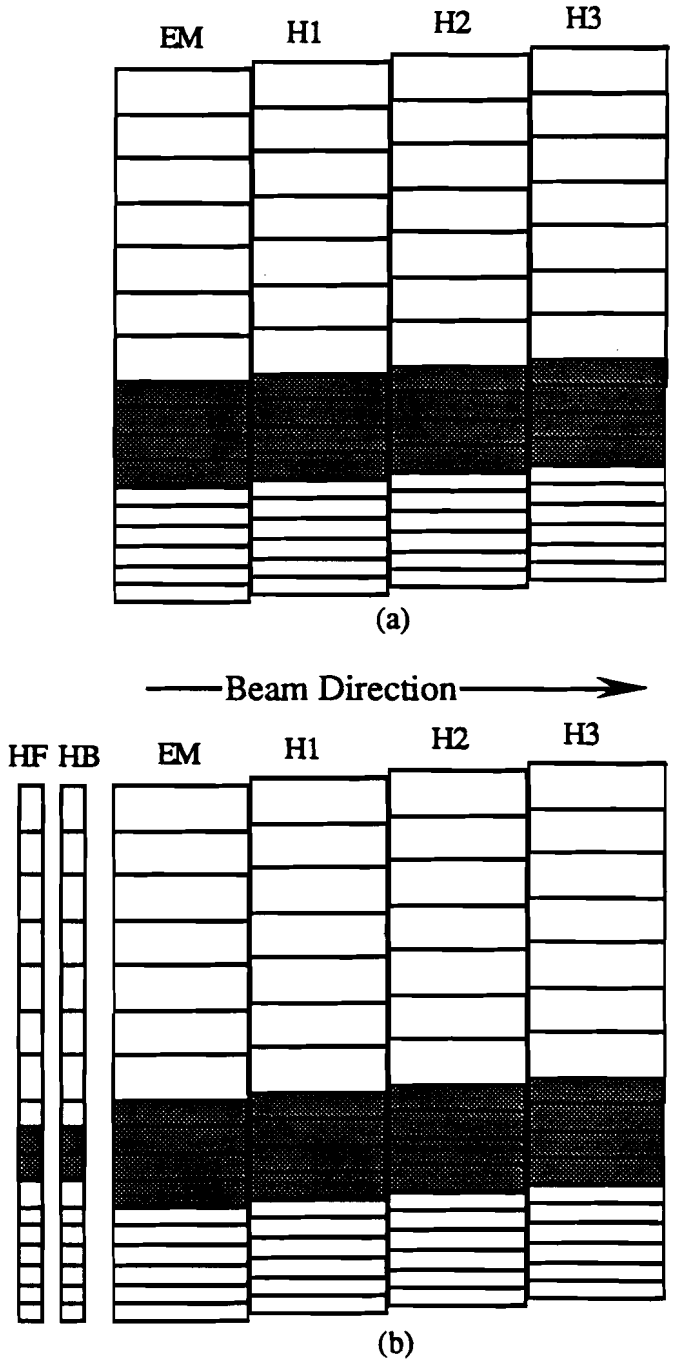

Figure 3.1
Module composition of a P trigger segment (a) and a Q • P trigger segment (b) (both in top calorimeter half).

3.2.3 The M and Q • P • M Trigger Elements

The first chapter described how a "symmetric" (two-particle) trigger was necessary to remove "trigger bias" from intrinsic parton motion. In fact, there was a good deal of asymmetry in many events because the detector accepted hadron pairs with significant net p_t. An asymmetric event would have a larger P signal from one half of the calorimeter and a correspondingly smaller P signal from the other than would the same mass event with net p_t of zero. The P segment threshold needed to be low enough to accommodate the lower apparent p_t of one of the particles in these asymmetric pairs. Yet, triggering only on pairs of Q • P elements would have admitted a huge number of low mass pairs into the data sample.

To address this dilemma, the "mass" signal M was constructed from a given analogue P segment and the sum of all the analogue signals from the opposite calorimeter half. The M signal indicated that a given local particle energy deposition (signalled by the P segment trigger) could be part of a possible massive state event, given the entire opposite side transverse energy deposition (E_t). Each M signal was discriminated such that $p_t + E_{t(opp)}$ was greater than 4 GeV. This reduced the admittance of low mass events without having to form and discriminate on 144 (12× 12) individual Q • P pairs triggers. Each mass signal was associated with the analogue P signal it comprised. Two different logic signals were formed when the M signal was sent through two different discriminators. This gave the experiment two different mass thresholds with the "M" mass logic signals at 6 GeV and "MHI" at 8.5 GeVThe trigger element Q • P • M was formed from the coincidence of the M logic signal with its corresponding Q • P signal. This is illustrated in Figure 3.2:

$$E_T = \sum_{i=2}^{16} (EME + EMW + H1E + H1W + H2E + H2W + H3E + H3W)_i$$

$$M_j = P_j + E_{T(opp.side)}$$

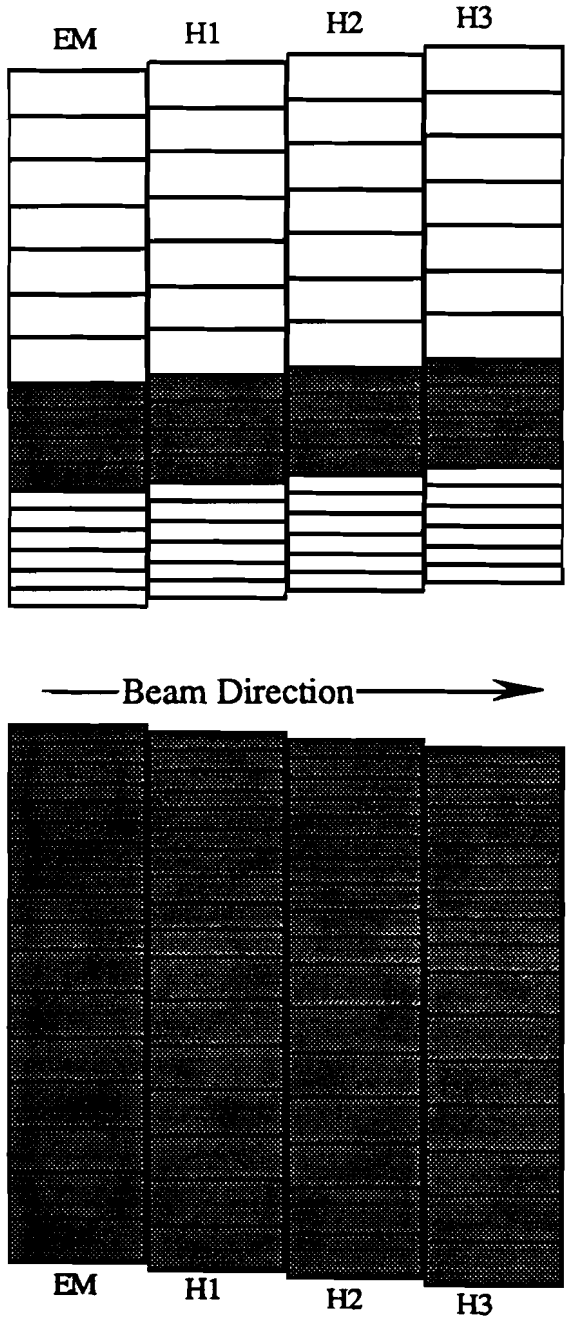

Figure 3.2
Module composition of an M trigger element.

3.2.4 *Event triggers*

The data run employed three different triggers. These comprised Q •P pairs, Q •P •M pairs, and MHI pairs. Each type of pair was constructed from an "OR" of the 12 logic signals from the top half trigger elements in coincidence with an "OR" of the 12 logic signals from those of the bottom A logic signal from an "OR" gate is positive if any of the incoming signals are positive. Table 3.2 lists the event triggers and their trigger segment composition.

The three triggers represented three different mass thresholds. In order to have an adequate sample of high mass events, the two lower triggers Q•P pairs and Q•P•M pairs were "prescaled", typically by factors of 128 and 2 respectively. The complete efficiency of the Q•P pairs trigger below the high mass thresholds enabled "turn-on" curves to be calculated to determine the efficiency of the event trigger over the mass range above 6 GeV/c^2. All MHI triggers, and the selected Q •P •M and Q •P triggers were sent to a "master trigger" circuit which signalled the PDP-11 to begin the data read-out.

Pairs Trigger	Composition
$Q \bullet P$	$OR_{12}(Q_i \bullet P_i)_{top} \bullet OR_{12}(Q_j \bullet P_j)_{bottom}$
$Q \bullet P \bullet M$	$OR_{12}(Q_i \bullet P_i \bullet M_i)_{top} \bullet OR_{12}(Q_j \bullet P_j \bullet M_j)_{bottom}$
MHI	$[OR_{12}(Q_i \bullet P_i \bullet M_i)_{top} \bullet OR_{12}(Q_j \bullet P_j \bullet M_j)_{bottom}]$ $\bullet [OR_{12}(Q_k \bullet P_k \bullet M_k)_{top} \bullet OR_{12}(Q_l \bullet P_l \bullet M_l)_{bottom}]_{HIGH\ MASS}$

Table 3.2
Event trigger composition
The i, j, k, and l indices refer to segment number, and indicate when the elements corresponding to the same segment must be in coincidence. The symbol "OR_{12}" indicates a 12 fold boolean OR.

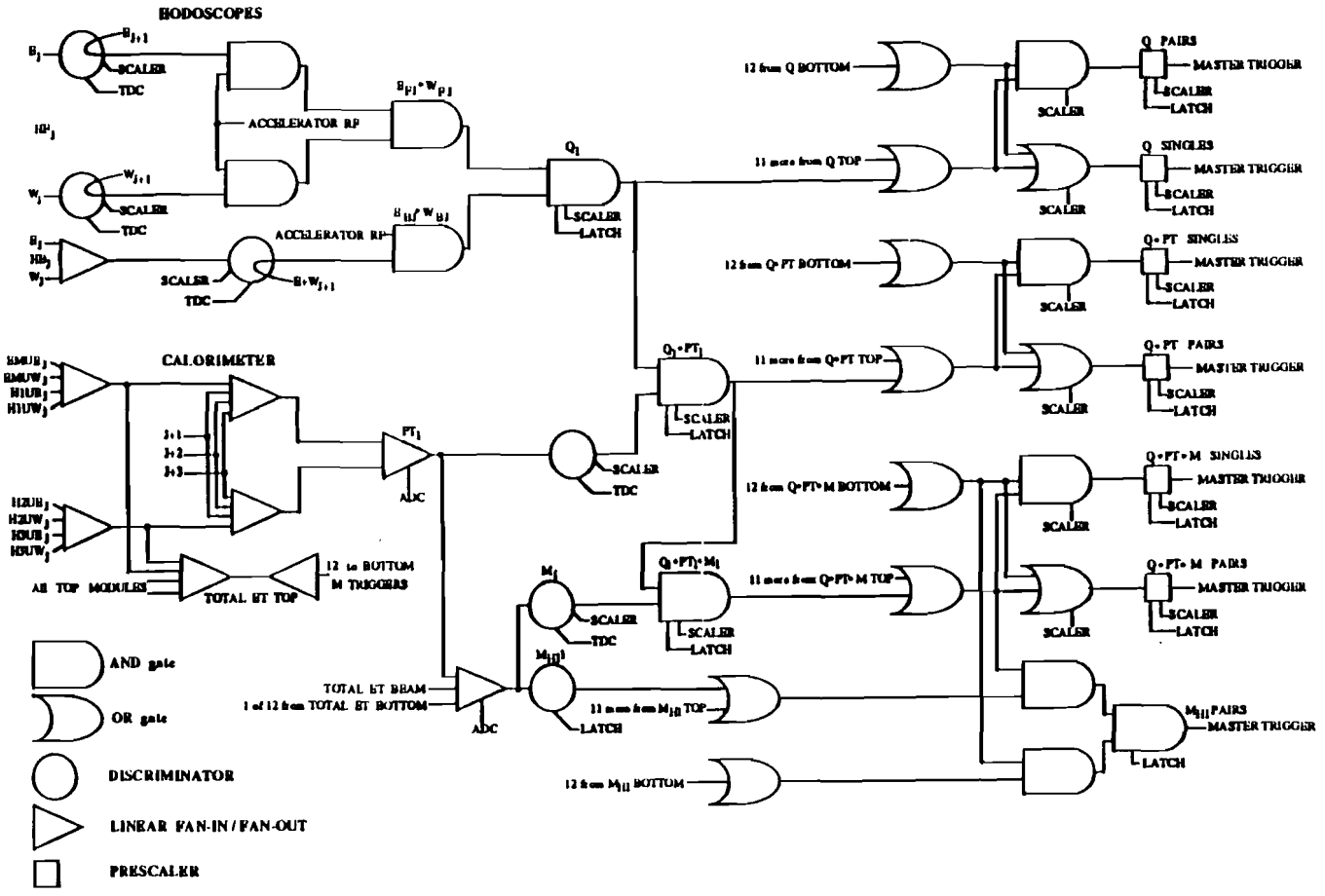

Figure 3.3
Total logic schematic for the E711 trigger.

3.3 Data Readout and Transfer

The operation of the experiment was driven by signals from the accelerator at various times during the one minute spill cycle. One signal was sent to the experiment several seconds before every spill to initiate the generation of 16 "interrupts", or signals to the computer to read out any data from the electronics. These "null triggers" recorded the ADC levels when no phototube signals were coming in. They were then use to calculate digital offsets, or "pedestals" later on in the analysis. A later signal enabled the experiment, setting a "live gate" for the duration of the beam spill. During that time data could be read out upon receipt of a signal from the trigger logic. At the end of the spill, another signal triggered readout of scalers and monitoring devices. The scalers were reset before the next spill by a fourth signal. The relative times could be adjusted by a module in the experiment's control room.

The PDP-11 ran a single data acquisition program, MULTI[18], that read out data upon receipt of a NIM level logic signal from the trigger logic. MULTI issued commands to the CAMAC system that read out data according to one of two command sequences, and wrote the data onto tapes. The two sequences were an "A interrupt", or data event record, and a "B interrupt", or spill record. These are outlined below.

3.3.1 A interrupt

The data A interrupt sequence was initiated by a signal from the trigger logic described in the previous section. All ADC and TDC channels, trigger logic signal latches and some luminosity scalers were read out by the PDP-11 and recorded to tape. This was the sequence for all normal data taking and calibration runs. The pedestal events generated before each spill were also read out as A interrupt events, (the pedestal signals being sent to the master logic trigger). Table 3.3 lists the electronics and their associated physical quantities read out during an A interrupt.

Readout Electronics	Readout Information
LeCroy 2285 ADC	Hodoscope and Calorimeter PTM's
LeCroy 4290 TDC	Wire Chamber Drift Times
EG&G C124 Latches	Q Segment Logic Levels
EG&G C124 Latches	P Segment Logic Levels
EG&G C124 Latches	M Segment Logic Levels
EG&G C124 Latches	Q•P Segment Logic Levels
EG&G C124 Latches	Q•P•M Segment Logic Levels
EG&G C124 Latches	MHI Segment Logic Levels
EG&G C124 Latches	Trigger Type levels
Jorway Scalers	Lumonisity Monitors

Table 3.3
A interrupt list

3.3.2 B interrupt

After the spill, an accelerator clock signal prompted MULTI to read out another set of digitising electronics. The B interrupt read out comprised scalers recording the luminosity monitor counts, the analysing magnets' currents, the settings of various beamline elements, and the trigger totals collected over the duration of the spill. Table 3.4 lists the electronics and their associated quantities read out during a B interrupt.

Readout Electronics	Readout Information
Jorway Scalers	Beamline And Experiment Magnet Currents
Jorway Scalers	Ion Chamber Counts
Jorway Scalers	Lumonisity Monitors
Jorway Scalers	Trigger Type Counts, Prescaled
Jorway Scalers	Trigger Type Counts
Jorway Scalers	Q Logic Signal Counts
Jorway Scalers	P Logic Signal Counts
Jorway Scalers	M Logic Signal Counts
Jorway Scalers	Q•P Logic Signal Counts
Jorway Scalers	Q•P•M Logic Signal Counts
Jorway Scalers	MHI Logic Signal Counts

TABLE 3.4
B interrupt list

3.4 Online Monitoring

During a run, the PDP-11 sent approximately 10% of the events recorded through a parallel link to the VAX 780, for monitoring and analysis. The EVENT BUILDER[19] program received these events and stored them into the VAX 780 memory. another program on the VAX, CONSUMER, read the events from memory and performed various analyses to monitor detector performance. several display screens and hard copy devices were employed for the output display. This was vital to understanding how well the apparatus was functioning, and for spotting malfunctions. Figures 3.4 shows output for trigger latches and chambers hits, as examples of the kind of information continuously displayed. Also displayed were pulse height information from the calorimeter and hodoscope PMT's. An event display showed reconstructed particle trajectories, computed online. With this information, voltage levels and discriminators could be corrected and any other adjustment made to maintain stable running conditions.

The EPICS[20] program, running on a PDP-11 from the beamline operations area, read out the settings of all relevant beamline devices. Some of the devices were under direct control of the E711 experimenters, particularly those magnets used for horizontal and vertical target scans. During a run, these were adjusted to maximize the beam interception by the target. The beam intensity could be controlled by adjusting the aperture of a collimator as necessary to keep rates within the range of the chambers' ability to operate (see section 2.2).

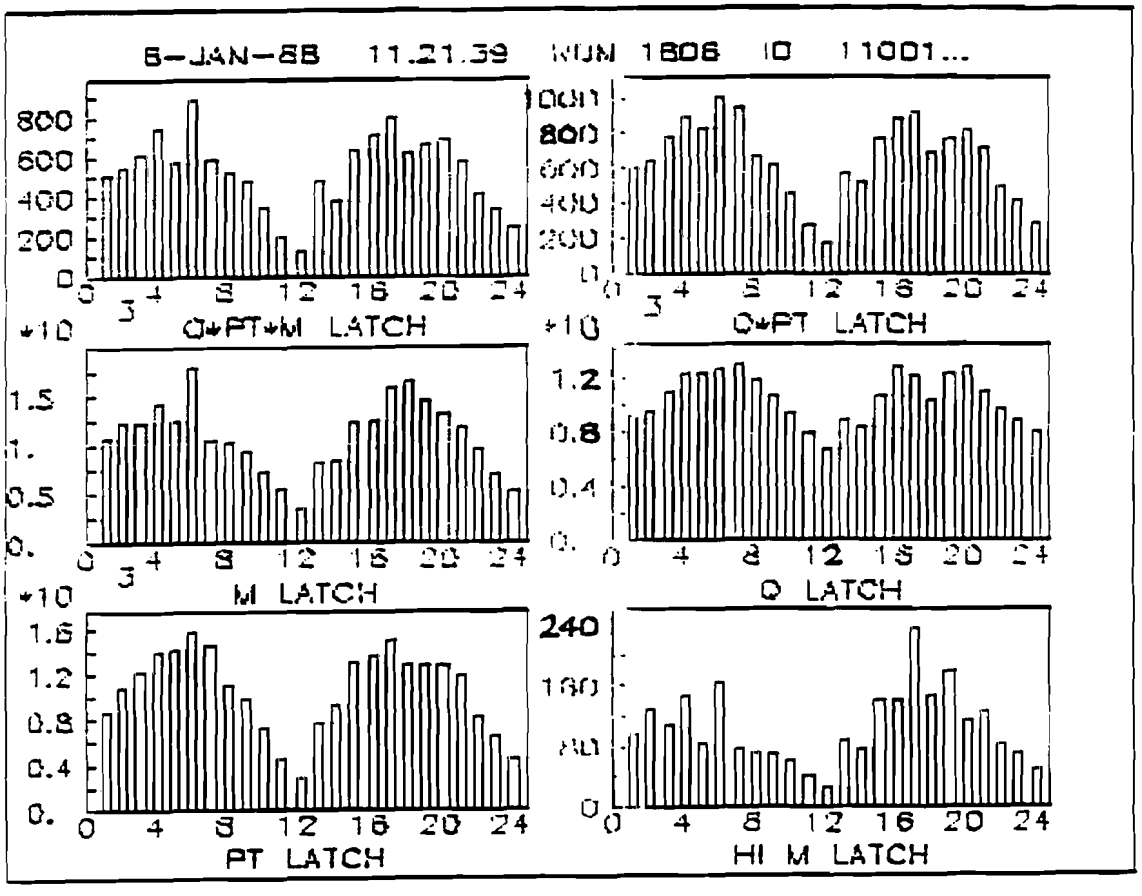

Figure 3.4
Display of trigger segment latches from monitoring program

CHAPTER 4

ANALYSIS

The process of transforming the data written onto tapes into physics results is multifold. First, it must be decided what variables will be useful and necessary for constructing the desired cross sections and distributions. The numbers read off the tapes must then be translated into physical quantities: tracks, momenta, energies, trigger sums, etc. There must be chosen a set of criteria, readily verifiable, for selecting those events that are triggered by genuine high-p_t hadron pairs. Out of these, a sample had to be extracted that was deemed analysable. Detector acceptance and various efficiencies had to be determined, and the systematic errors and backgrounds understood. The purpose of this chapter is to describe the procedure used to produce angular distributions and cross sections for charged states of massive hadron pairs from the raw data. Results are presented in the next chapter.

4.1 Variables Used in This Analysis

The phase space of two-particle systems can be completely described by choosing six variables. As mentioned earlier, the kinematics of hard scattering are exactly those of two-body decay. Therefore, the mass of the hadron pair and and three momentum components of dihadron system, plus the the two angles defining the directions of the hadron scattering in the dihadron c.m. frame constitute a complete set of variables. For the purposes of this analysis, it was convenient to define a slightly different set of variables describing the motion of the system, so the data are parametrised and binned in the following quantities:

1. Mass of the hadron pair:

$$M = \sqrt{(E_1 + E_2)^2 - (p_1 + p_2)^2} \ . \tag{4.1.1}$$

2 Rapidity of the hadron pair:

$$Y = \frac{1}{2} \ln \left[\frac{(E_1 + E_2) + (p_{1z} + p_{2z})}{(E_1 + E_2) - (p_{1z} + p_{2z})} \right] . \tag{4.1.2}$$

3. Magnitude of the net transverse momentum of the pair:

$$P_t = \sqrt{(p_{1x} + p_{2x})^2 + (p_{1y} + p_{2y})^2} \ . \tag{4.1.3}$$

4.Polar angle in the dihadron centre-of-mass:

$$\cos\theta = \frac{p_{1z}^*}{|\vec{p}_1^{\,*}|} = \frac{p_{2z}^*}{|\vec{p}_2^{\,*}|} . \tag{4.1.4}$$

(stars denote quantities in the dihadron c.m.)

The rapidity can be thought of as a way of expressing the net P_z of the massive state in a Lorentz-invariant manner. The azimuthal symmetry of the experiment suggested using the magnitude of the net p_t of the pair. Since the cross sections and distributions are to be plotted as functions of $\cos\theta$ and mass, they are naturally included. The remaining two variables can be chosen to be:

5. Average of the azimuthal angle of the dihadron system:

$$\Phi = \frac{\phi_1 + \phi_2 + \pi}{2} \ . \tag{4.1.5}$$

6. The deviation from dihadron coplanarity :

$$\Delta\Phi = \frac{\phi_1 - (\phi_2 + \pi)}{2} \quad . \tag{4.1.6}$$

The cross sections are independent of both of these variables, and they can be integrated over 2π radians in acceptance.

The definition of $cos\theta$ is problematic. The scattered partons "fragment" into hadrons that carry varying fractions (z) of the parton total momentum. The uncertainty in the difference between the z's of the leading hadrons renders the $cos\theta$ of the parton scatter indeterminate from the dihadron $cos\theta$ reconstruction. An approximation often used is[21]

$$\cos\theta = \frac{1}{2}\left(\frac{|p_{1z}'|}{|\vec{p}_1'|} + \frac{|p_{2z}'|}{|\vec{p}_2'|}\right) \tag{4.1.7}$$

where the primes denote quantities in frame where the net P_Z of the hadron pair is zero. The reconstruction of $cos\theta$ for the present analysis is discussed in the next chapter.

4.2 Definition of the Cross Sections

The standard way of describing results from scattering experiments is by constructing a cross section. A cross section is an expression of the probability for a scattering process to occur, and can be calculated from the parameters of a field theory (i.e., coupling constants, definition of the fields, etc.). Experimentally, cross sections are constructed using the number of a particular event observed, corrected for apparatus acceptances and efficiencies, and the number of total scatterers (in this case beam protons and target nucleons). The latter can expressed as the "luminosity" and can be thought of as the sample space of all possible interactions available to a given experimental setup, integrated over time.

By dividing the events into bins of one or more kinematic variables, a functional dependence of the cross section can be determined. A differential cross section written in the variables described above is expressed as

$$\frac{d^6\sigma}{dM\ dY\ |P_t^2|dP_t\ d\cos\theta\ d\Phi\ d(\Delta\Phi)}$$

The cross section is independent of Φ and $\Delta\Phi$, and these can integrated out over 2π radians in the acceptance. In this analysis two differential cross sections are considered. These are be written as

$$\frac{d^2\sigma}{dMdY} = \frac{1}{\Delta M\Delta Y} \bullet \int \frac{d^4\sigma}{dMdYd\cos\theta dP_t} dMdYd\cos\theta dP_t \qquad (4.2.1)$$

and

$$\frac{d^3\sigma}{dMdYd\cos\theta} = \frac{1}{\Delta M\Delta Y\Delta\cos\theta} \cdot \int \frac{d^4\sigma}{dMdYd\cos\theta dP_t} dMdYd\cos\theta dP_t \qquad (4.2.2)$$

where ΔY, ΔM and $\Delta cos\theta$ are the intervals of integration ranges for rapidity, mass and $cos\theta$. Needed to calculate these cross sections are the numbers of events for each bin, acceptance correction, efficiency corrections and the normalisation (luminosity). These will be described in later sections, with the full expression for the cross-sections made explicit. A description of the selection process for events used in the analysis follows in section 4.3.

4.3 Data Reduction - Event Samples

The actual processing was accomplished in several stages. The first pass, producing "data summary" tapes (DST's), calculated track trajectories from the drift

chamber data, and included them with the rest of the raw data. The second pass converted these data into physical quantities and wrote these onto data summary files (DSF's). From these files a sample of events was selected according to criteria for massive hadron pairs.

4.3.1 Track Reconstruction

The reconstruction of tracks out of chamber hits read out from the TDC's was done on at Florida State University on the Cyber 205 and the ETA 10 supercomputers[22]. The algorithm used the information from the 4 different planes in each of the five stations to find and "fit" straight-line tracks downstream of the bending magnets.

The algorithm for this "trackfitter" ran in a "vector", as opposed to "scalar" mode. That is, operations normally done sequentially on individual elements of the data were done simultaneously on the "vector" formed by the entire set of elements - in this case the list of all the recorded TDC hits for a given event. For this trackfitter, the planes were divided into cells three wires wide, and tables computed of all possible combinations of these cells that formed a 2-dimensional track in any of the four views. These were read into the program and all 2-dimensional tracks in each view were found by direct "masking" of the hit vector by these tables. A second stage involved matching up these 2-dimensional tracks to form 3-dimensional tracks. The corresponding hits of each track were fit to a straight line using the position associated with each point from the TDC drift time.

These 3-dimensional candidate tracks were subjected to several requirements before being passed on. There had to be at least 15 out of a possible 20 hits associated with a given track. At least three out of the four views had to have three out of a possible five hits with at least two hits in the remaining view. The chi-squared per degree-of-freedom calculated from the above straight-line fit needed to be less than 15. Slopes, target plane intercepts, plane hit patterns and chi-squares of all fitted tracks that passed these

requirements were written onto a data summary tape (DST) along with ADC, scaler and latch data for the given event.

One DST was produced for every raw data tape processed in this way. In addition to the track information listed above, data from the "pedestal" and "spill" triggers were also recorded. An event had to have at least one track reconstructed for the event information to be written to the DST. False events were removed this way, as well as a number of real events due to the chamber inefficiencies. These are discussed later this chapter.

Target	Reduction
Be	0.52
Fe	0.61
Al	0.60
W	0.41

Table 4.1
DST Production
Reduction = # DST event/raw events

4.3.2 Calorimeter Information

After the track reconstruction was done on the raw data tapes, the processing proceeded on the local area VAX cluster (LAVC) at FSU. A program read in the "pedestal" events, averaged the ADC pedestals and then proceeded to subtract these values from the ADC data in the regular data events. Using the calibration constants, the values from the sums of the ADC's of each calorimeter segment (the "P" trigger elements described in the last chapter) were converted into an energy. This information, along with the physical quantities and hit patterns from the trackfitter, and the latch information were then written onto a data summary file (DSF). Information from the spill events were written into a separate B interrupt file. Each of the 338 DST's processed produced a separate DSF and B interrupt file.

4.3.3 Data Set Selection

While writing out the track information and module energies, the program producing the DSF's also calculated and plotted all the other physics variables to be used in the analysis to determine how well the reduction programs were working and to come up with reasonable cuts for the final data set. From these, several requirements were adopted for an event to be considered from a real high-p_t hadron pair.

1. Target constraint: The y-z view of the tracking system was not affected by the magnetic field, so each track should point back to the target. The y intercept (expressed in cm) at the target was limited to (see Figure 4.1)

$$-2.0 \leq y_{TARG} \leq 1.6 \tag{4.3.1}$$

2. Calorimeter containment: Because of the trapezoidal geometry of the calorimeter, many genuine high-p_t particles that could be reconstructed by the trackfitter could not have been part of the event trigger. The track coordinates at the calorimeter face needed to be within the area where its energy shower could be largely contained, and the calorimeter nearly 100% efficient for triggering. These "fiducial" volume cuts (*fiducia*: Latin for trust) were determined from studying turn-on curves at the edges of the calorimeter for the P trigger segment associated with a given track. These are shown in Figures 4.5-4.9. For the y coordinate on the calorimeter face

$$-150.0 \leq y_{CAL} \leq -40.0 \tag{4.3.2}$$

for the bottom calorimeter half, and

$$40.0 \leq y_{CAL} \leq 145.0 \tag{4.3.3}$$

for the top half (units in centimeters).

For the azimuthal angle:

$$|\Phi| = arc \quad \tan\left|\frac{x_{CAL}}{y_{CAL}}\right| \leq 40 \tag{4.3.4}$$

3. Momentum: For a track to be part of an event that triggered the detector its y momentum component had to be above the hardware P segment threshold, therefore

$$p_y \geq 2.0\ GeV / c \tag{4.3.5}$$

A typical P segment turnon curve is shown in Figure 4.2.

4. Energy-momentum comparison: Though the calorimeter was designed primarily for triggering rather than measuring, its resolution of $0.64/\sqrt{E}$ was adequate for a rough confirmation of the momentum information from the chambers (the calibration of the calorimeter is discussed in Appendix 1). Tracks coming from photon conversion before the first chamber, accidental showering or simply bad track reconstruction produced tracks with apparent infinite momentum. These could be rejected on the basis of a large discrepancy between p_y and E_y (segment transverse energy). For ΔE=$0.64/\sqrt{E}$ and Δp = $2.6 \times 10^{-4}E^2$, the energy-momentum discrepancy was restricted to

$$\frac{E_y - p_y}{\sigma} \leq 10.0$$

where (4.3.6)

$$\sigma = \sqrt{\Delta E^2 + \Delta P^2}$$

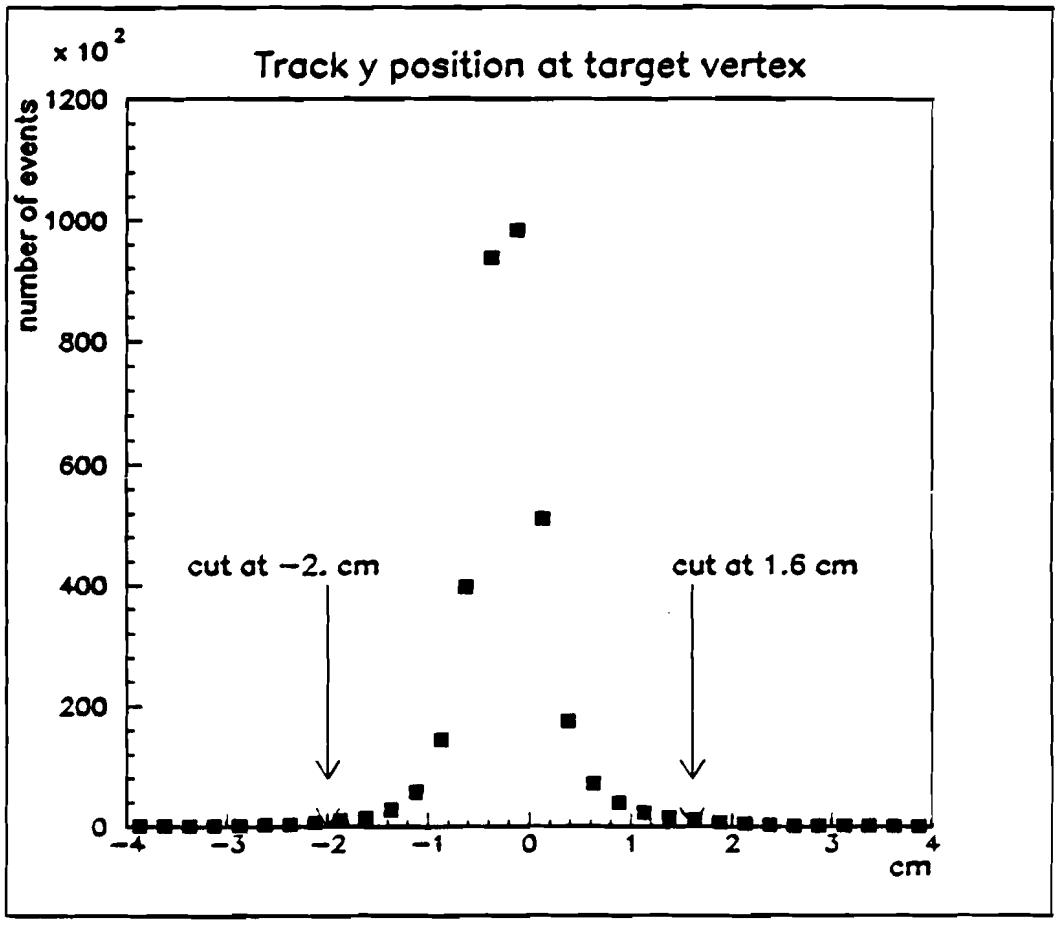

Figure 4.1
Track y-intercept at the plane of the target

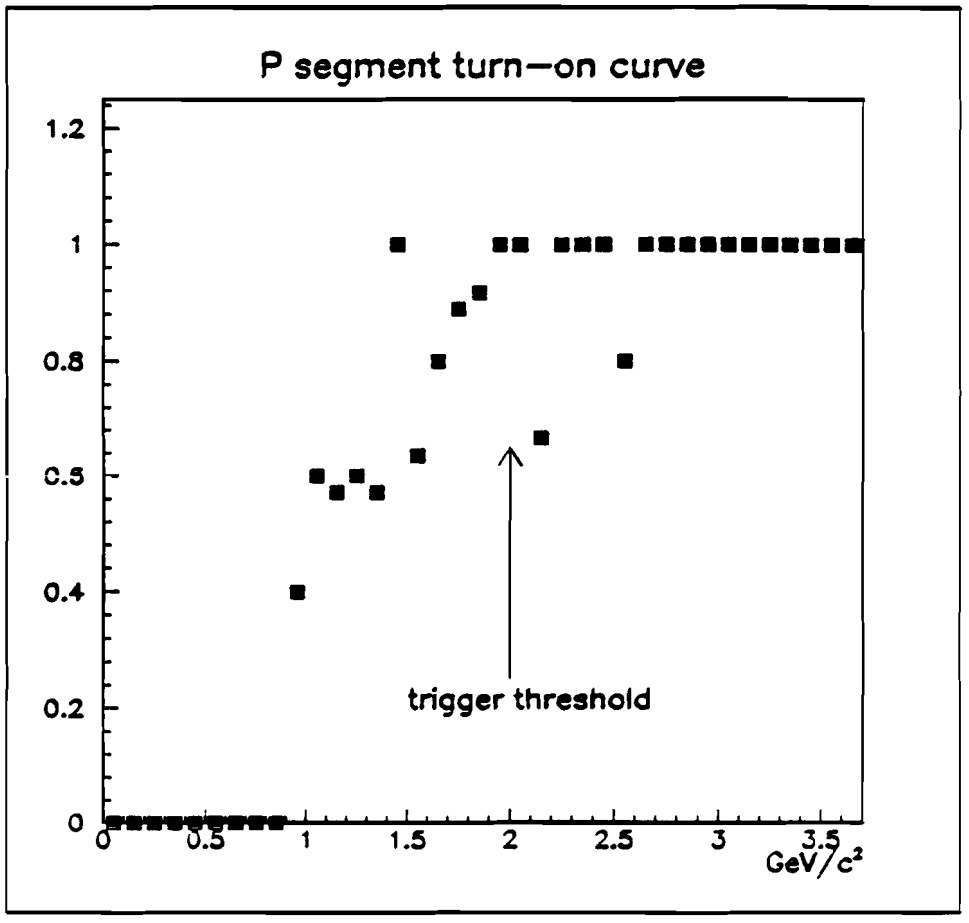

Figure 4.2
Turn-on curve for trigger segment P latch with respect to energy deposited in calorimeter P segment.

The expression for Δp used E rather than p, since the error in p for a badly fit track would be large out of proportion to the real energy deposition. Plots from the uncut data showed no comparable discrepancy of tracks with less momentum than energy deposited. (see Figure 4.3).

5. Electron/hadron energy ratio: To ensure that an energetic electron entering the calorimeter would not simulate a high-p_t hadron, a condition was placed on the ratio of the energy deposited in the *EM* section of a P segment (E_{em}) to the entire segment energy (E_{cal}). Since this ratio would be 1.0 for a real electron (all of its energy being completely contained in the EM section), the requirement

$$E_{em}/E_{cal} < .98 \tag{4.3.7}$$

was made on the track's energy deposition profile.

The selection program went through all the tracks for each event, requiring that each one pass through cuts # 1 through # 5 to be considered viable. However, the 3-wire width of the chamber cells defined in the trackfinder algorithm introduced hit ambiguities that lead to a cluster of duplicate tracks reconstructed about the real track. To eliminate the duplicates, the following separation function was defined :

$$R = \frac{1}{5} \times \sqrt{(x_i - x_j)^2 + (y_i - y_j)^2} \,/\, W \tag{4.3.8}$$

x_i and y_i being the x and y coordinates for track "i" and "j", and W is the width of the wire spacings. Groups of tracks were formed for which R < 3. The track with the the greatest number of hits and smallest chi-square was selected, and the others rejected. The track multiplicity before and after the track selections are given in Figure 4.4

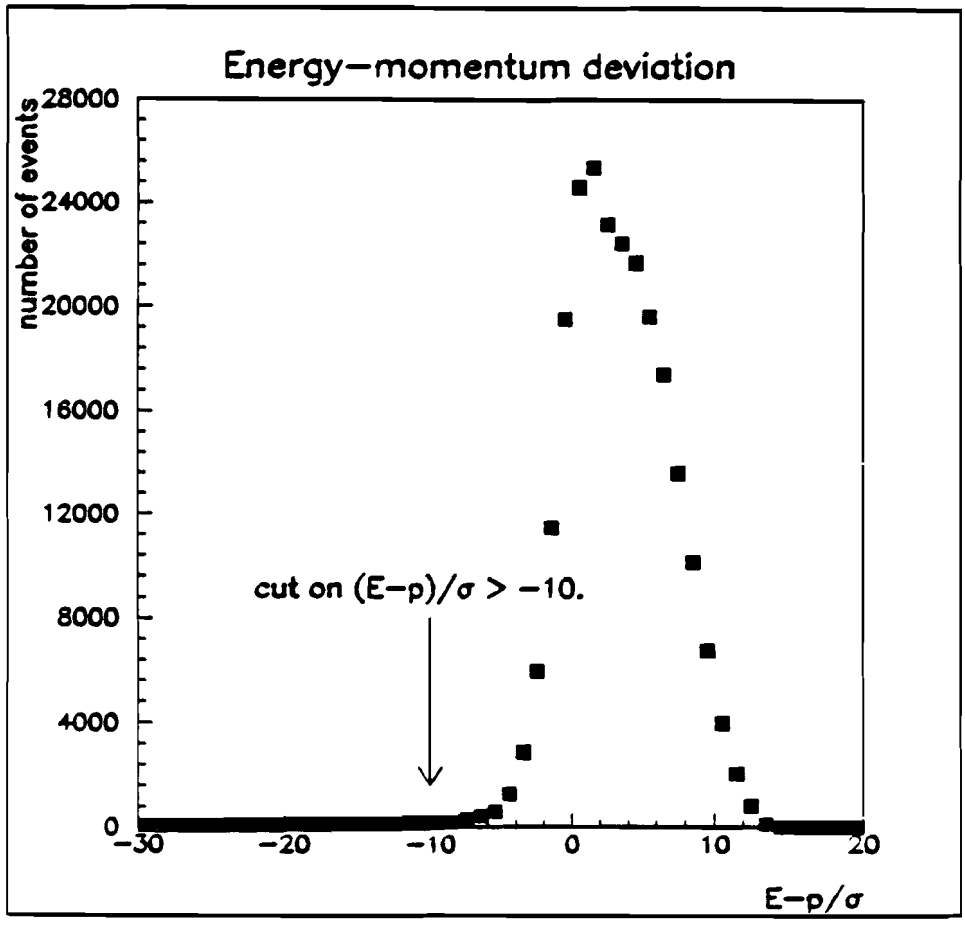

Figure 4.3
Cut on the deviation between Calorimeter energy and momentum reconstructed from Chamber info

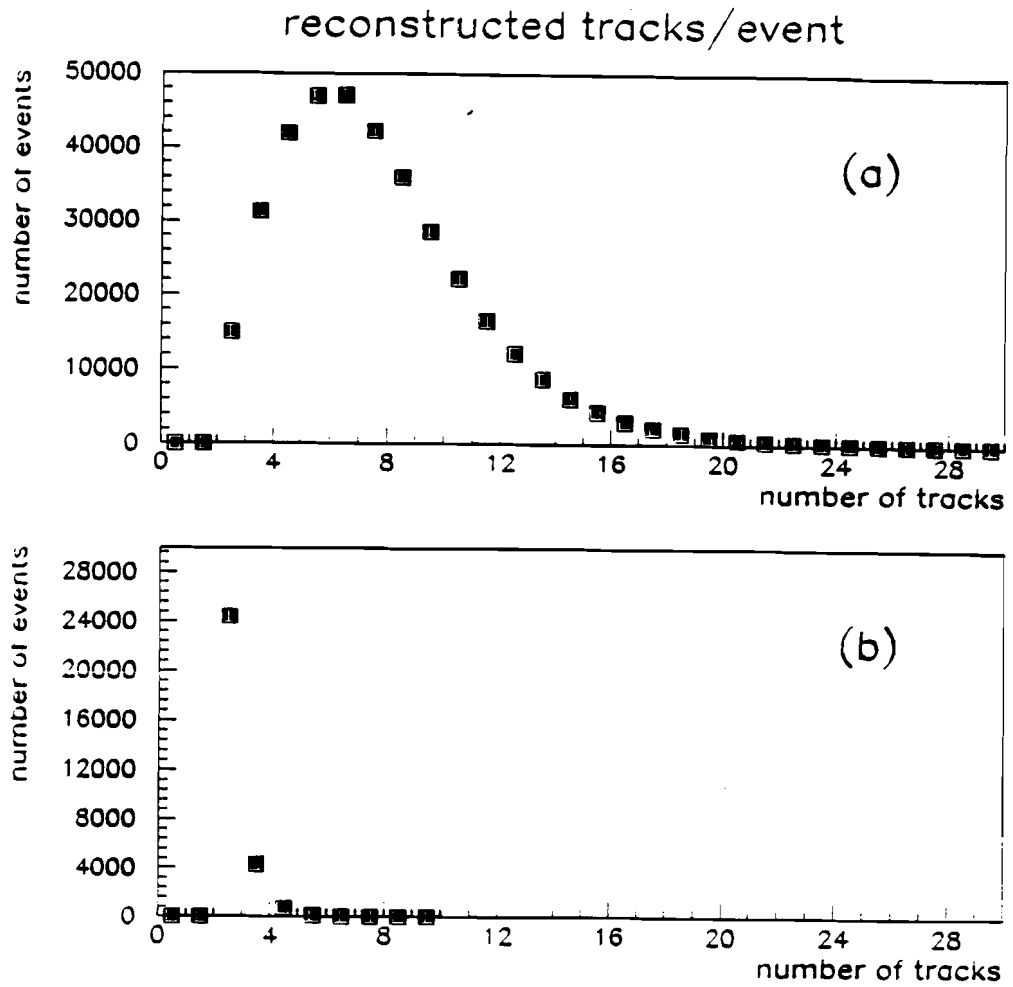

Figure 4.4
Number of tracks per event (a) before track selection and (b) after selection and elimination of duplicates

The real tracks having been selected, every permutation of pairs formed from one top and one bottom was considered, and the pair of highest mass chosen. If its mass was greater than the mass cut (which, for the analysis described in this dissertation, was 6.5 GeV/c^2), the event was written onto a condensed data summary file (CDSF). Table 4.2 shows the physical quantities for a CDSF event.

Of the 455 data tapes written during the 1987-88 run, ~ 5% contained runs configured for calibration rather than data taking. Low intensity runs were used for calibrating the ion chamber. Runs taken with the muon trigger setup (described in section 2.7) were used for alignment studies, and for the calorimeter and hodoscope calibration. Of the event tapes, many were rejected because of some problem with the apparatus or readout system at the time of the run. For the analysis described here 297 tapes were selected for the data sample. Table 4.3 summarizes event sample reduction for each target.

Data word (16 bit)	Data List Element
1	Run Number
2	Event Number
3	# Of Tracks (NT)
4	Latch Bits Set
5	A Interrupt Number
6	B Interrupt Associated Spill Number
7 - 38	Calorimeter Module Energies (16 Top and Bottom = 32)
39 - 45	Track #1 Number of Hits x-z Target Plane Intercept x-z Slope y-z Target Plane Intercept y-z Slope Chamber Plane Hit Pattern Nearest Prop Tube Hit
46 - 53	Track #2 . ...
NN - NN+6	Track # NT ...

Table 4.2
CDSF event data list

Target	Be	Al	Fe	W
# of Tapes	75	29	67	126
#Events on DSF	1.58×10^{6}	0.94×10^{6}	1.80×10^{6}	1.09×10^{6}
# Events on DSF Pairs Trigger	0.95×10^{5}	0.68×10^{5}	1.23×10^{5}	0.84×10^{5}
# Events Written CDSF	7848	5289	9534	6992

Table 4.3
Data reduction summary

4.4 Momentum Calculation

The two magnets upstream of the chambers imparted a horizontal p_t kick of 1.16 GeV/c to any charged particle passing through the length of the combined magnetic fields. The fields were measured to be uniform to within 1 %, so the momentum analysis used the approximation that the p_t kick came at a single bend plane at the half-way point in z in the magnetic field. The interaction point upstream of the magnet was taken to be the central point in x and z of the target. The y coordinate of the interaction could be extrapolated from the downstream track as the momentum component in y was unaffected by the magnets. The momentum was determined by a "similar triangles" construction with the slope and intercept information provided by the trackfitter, and is described in Appendix 3.

The errors in the momentum calculation came primarily from the length of the targets in z and the combination of the target width and chamber resolution. These are proportional to p and p^2 respectively, and are listed in table 4.4. The details of the error calculation are also included in appendix 3. It should be noted that at p = 20 GeV/c the p^2 term becomes dominant, and at 200 GeV/c the term in p^2 is negligible.

Target	Calculated Error
Be	$\Delta p = 2.795 \times 10^{-4} p^2 + 5.263 \times 10^{-3} p$
Fe	$\Delta p = 2.689 \times 10^{-4} p^2 + 5.118 \times 10^{-3} p$
Al	$\Delta p = 2.542 \times 10^{-4} p^2 + 2.164 \times 10^{-3} p$
W	$\Delta p = 2.794 \times 10^{-4} p^2 + 1.234 \times 10^{-3} p$

Table 4.4
Calculated target dependant errors

Two different studies, with the data and with Monte Carlo events, confirmed these calculations. One study took the difference in momenta found by two different trackfitters for each track in a selected data sample. The width of this distribution was consistent with the calculated results. Another study superimposed Monte Carlo generated tracks onto data events, and compared their known momentum values to those the trackfitter had reconstructed. The results were also consistent with the above calculated values.

The difference distributions from these studies were used in a Monte Carlo mass resolution calculation. It was found that the resulting corrections to the mass were less than 2 % of the mass bin size, and were considered negligible.

4.5 Acceptance Calculation

The fact that the dihadron centre-of-mass was often quite different from that of the beam-target system required an acceptance correction in the varibles M, Y, $\cos\theta$, and p_t. The sensitivity of the acceptance to the rapidity is illustrated in Figure 4.5. The acceptance of the detector for the analysis described in this dissertation was calculated using a simple geometric Monte Carlo simulation of the E711 detector. With the fiducial and p_y cuts of the analysis incorporated into the program, the acceptance was calculated

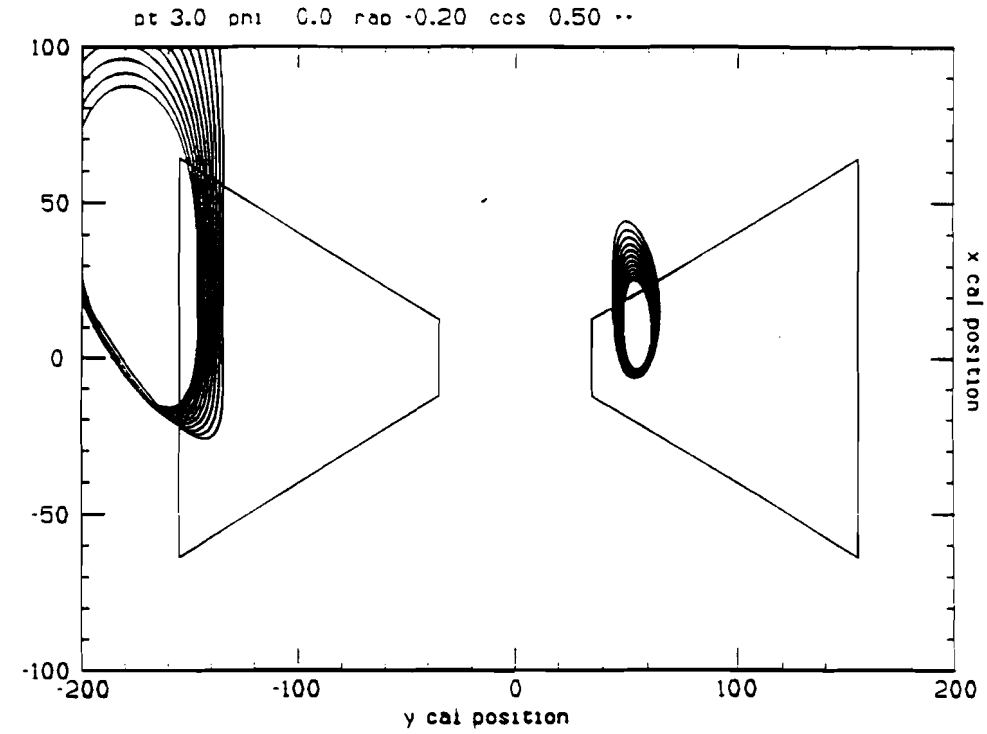

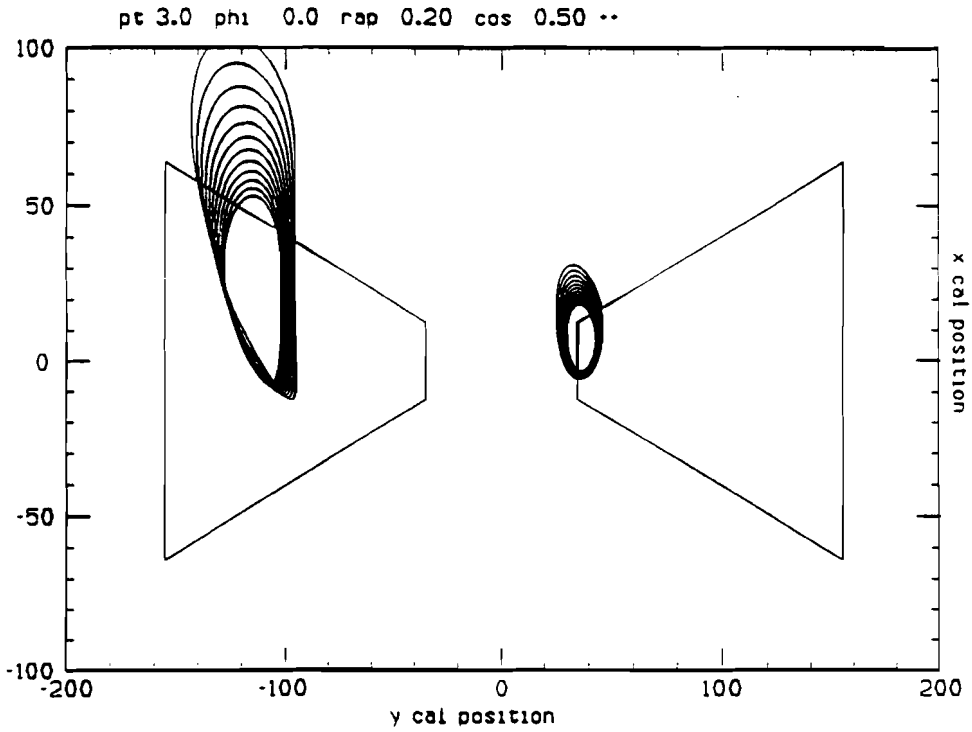

Figure 4.5
The geometric acceptance for events with Pt less than 3.0 GeV and $cos\theta$=0.5 is shown here for a y=-0.2 and y=0.2. The forward going particles in the centre-of-mass are towards the inner edge of the calorimeter

in bins of the pair variables, M, Y, $\cos\theta$, and p_t, with integration over Φ_{AVE} and $\Delta\Phi$. The output is in the form of $\cos\theta$ - rapidity tables for various values of M and p_t. For the geometric acceptance, these tables were calculated for like- and unlike- sign charge states. Since this program also incorporated the dead wire positions, the position-dependent efficiency of the detector could also be calculated, with a separate calculation for positive (+ +) and negative (- -) like-sign states.

The Monte Carlo simulation, which ran on the VAX 2610 cluster at the University of Michigan, generated back-to-back hadron pair of a given mass, net rapidity and $\cos\theta$ (in the dihadron c.m.). Φ was generated in a flat distribution, and P_t was generated according to a convolution of a 2-dimensional Gaussian function (for the parton motion smearing), and a polynomial function in the scattering plane (for the fragmentation smearing). The contribution to P_t by the transverse parton motion in the nucleon (hereafter denoted as p_{KT}) and the difference in parton momentum fraction $(z_1 - z_2)$ between the two leading hadrons is expressed as

$$P_t = \sqrt{p_{KT\perp}{}^2 + ((z_1 - z_2)\cdot|p_{PART}| + p_{KT\parallel})^2}\,. \qquad (4.5.1)$$

The parton transverse momentum p_{KT} is expressed here as components parallel and perpendicular to the parton scattering plane. p_{PART} is the magnitude of the parton momentum in the parton-parton centre-of-mass frame Figure 4.6 shows the corresponding "in plane" and "out-of-plane" components of the net dihadron P_t from the data.

The pair was boosted from the dihadron rest frame into the beam-target c.m. frame by a vector V constructed from p_z (calculated from the rapidity) and the net P_t components defined by $\cos\theta$ and Φ. A second boost along the z (beam) direction with β and γ calculated from the Fermilab beam momentum brought the pair into the lab frame (Appendix 4 describes the general Lorentz boost for a two-particle system). Sums of

particles that would pass through the detector, defined in the Monte Carlo by the fiducial cuts, were kept for each bin. These were divided by the number of events generated per bin for the acceptance of an event of particular mass, rapidity, P_t and $cos\theta$.

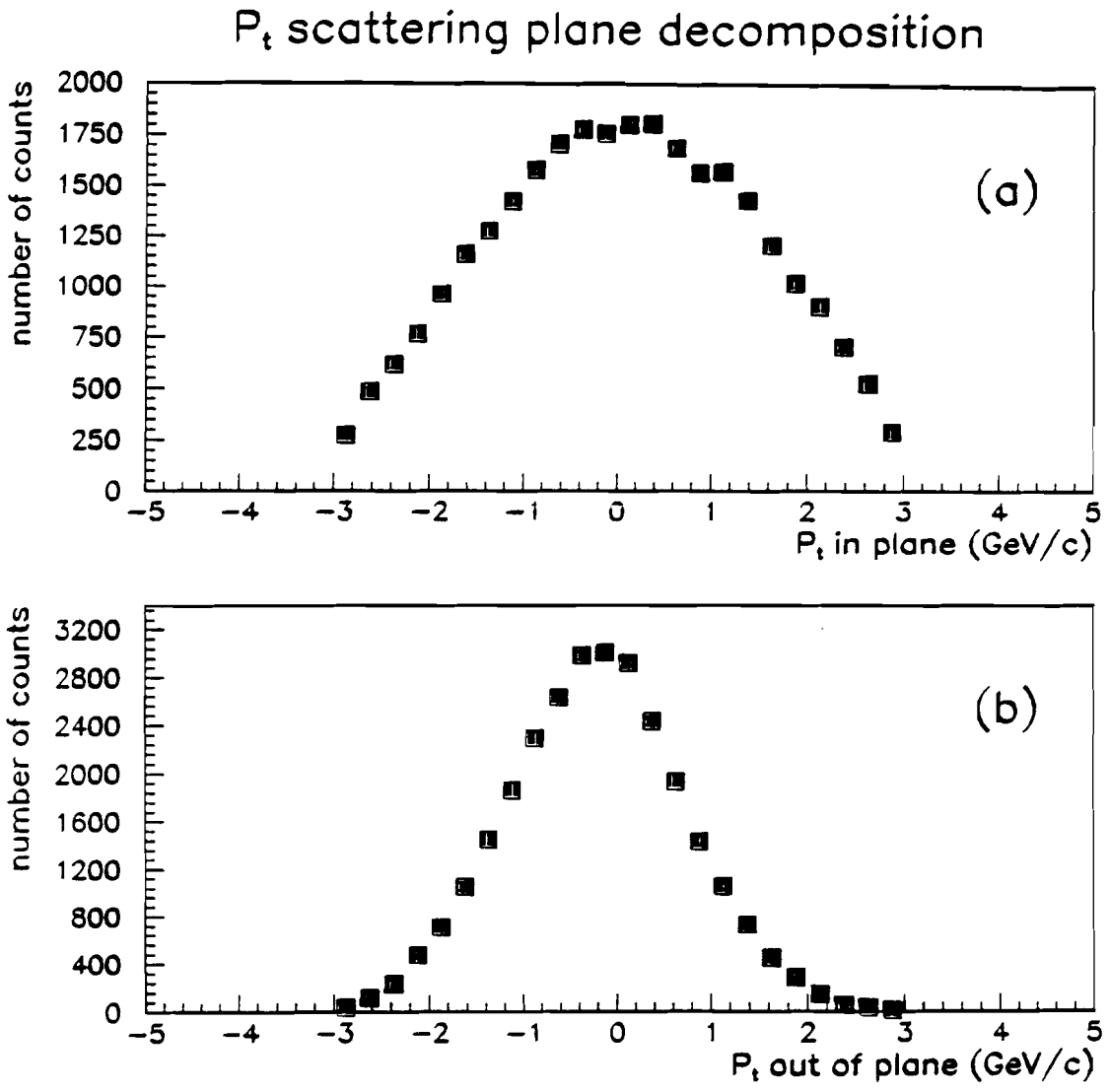

Figure 4.6
Components of the net tranverse momentum of the hadron pair (a) parallel to the scattering plane (b) perpendicular to the scattering plane. The "out-of-plane" component comes principly from "k_t" motion, while the "in plane" component reflects both parton motion and differences in the partons' fragmention .

The inverse of this number was used in an event-by-event weighting in the analysis,

$$K_{ACC} = \frac{1}{\eta_{ACC}} \tag{4.5.2}$$

where

$$\eta_{ACC} = \frac{number\ of\ events\ accepted}{number\ of\ events\ generated} \tag{4.5.3}$$

4.6 Efficiencies

After determining what fraction of the events of a given mass, net p_t, rapidity and $cos\theta$ were accepted by the experiment, it was necessary to understand how reliable the detector was both in responding to the events that actually went through, and in reconstructing their kinematics. There were three types of these efficiencies that had to be included in the cross section calculations. These were 1) the "turn-on" efficiency in the mass trigger, 2) the global track reconstruction efficiency and 3) the efficiencies from the chamber performance which depended on the location in the detector. These are described below.

4.6.1 Mass Trigger Efficiency

The last chapter described three event triggers based on the mass of the hadron pair. The inherent resolution of the hadron calorimeter and the finite shower containment of the trigger segments caused the Q • P • M event trigger to be less than 100% reliable for low mass events. To correct for this, a turnon curve with respect to event mass was constructed for this event trigger using the Q • P trigger, described in the previous chapter, which was 100% efficient below the Q • P • M threshold. For a given region, or bin, of mass, the trigger efficiency is defined as

$$eff_{TRIG} = \frac{N_{QPM}}{N_{QP}} \tag{4.6.1}$$

where N_{QPM} is the number of Q • P events that also set a latch for a Q • P • M trigger, and N_{QP} is the total number of Q • P triggers. The data for this analysis was taken with the Q• P • M and MHI triggers disabled. This means that the signals from these triggers were disconnected from the "A interrupt" coincidence, but all other information was recorded. These Q • P events were required to pass the selection criteria described earlier. Table 4.4 shows the efficiencies and statistical errors for three bins of mass, two before total "turn-on". Monte Carlo calculations estimated the systematic error to be 5% for the mass bin 6.5 GeV/c^2 < M < 7.0 GeV/c^2. The Q • P • M trigger was completely efficient at mass 7.5 GeV/c^2 and above.

Mass Bin (Gev/c 2)	Trigger Efficiency
6.5 - 7.0	0.81 ±0.0023
7.0 - 7.5	0.90 ±0.0013
>7.5	1.00

Table 4.5
Mass trigger efficiency

4.6.2 Trackfitter Efficiency

After completion of the track reconstruction, it was discovered that the efficiency for the trackfitter to reconstruct tracks was dependent on the chi-squared requirement set inside the program. The chi-squared requirement was then loosened, and the trackfitter run on a sample of data. The results were compared with those from the same data passed through a different trackfinding algorithm, known to be efficient. With the looser chi-square requirement, the vectorised algorithm found virtually 100% of the tracks. Rather than go through the formidable task of redoing the entire data set, a subset of tapes from each target data set was selected and reprocessed (all the aluminum data) with the altered trackfitter. These were analysed with the same requirements for events as described

earlier. The ratios of events found by the original trackfitter to the modified version were calculated and found to be 0.81 ± 0.013. This was independent of target or trigger type. The ratios were then plotted both as a function of mass and as a function of $cos\theta$. The variation was found to be less than 3% in both cases and within statistical errors, so little distortion was introduced to the shape of $cos\theta$ or mass cross sections. Table 4.5 gives the overall efficiencies for both Q • P • M events and MHI events .

	Be	Fe	W	W (Early)
Q•P•M Pairs	0.8235 ±0.0097	0.8097 ±0.0062	0.8280 ±0.0099	0.805 ±0.012
MHI Pairs	0.808 ±0.021	0.806 ±0.014	0.833 ±0.023	0.792 ±0.023

Table 4.6
Trackfitter efficiencies

4.6.3 Chamber Plane and Dead Wire Efficiencies.

The third efficiency correction concerned the operation of the drift chambers. Due to the high rate of interaction during the spill, the probability that any given particle registered a hit was less than 100%. The overall efficiency was calculated for of each of the 20 DC planes using a tracks from a sample of processed events. A given plane was "turned off" in the program, and those tracks that could pass the requirements described earlier without that plane's hit being present were collected. The program was then run on those tracks with the plane "turned on", and the fraction of those tracks where that plane's hit was present was taken to be the plane's efficiency. Various individual wires were rendered inactive during the run. These were determined from wire-hit histograms, and a file was made of these "dead" wires for each plane.

The inefficiency from the dead wires cannot be handled globally since the dead wires were not uniformly distributed throughout the chambers. This introduced a dependence on $cos\theta$ as well as other variables. To calculate the efficiency correction, the

acceptance program also incorporated the dead wire positions into the geometric calculation. Tracks that were within a wire spacing of a dead wire's position had that particular hit were removed from the track's hit list. A subroutine was called that incorporated the plane efficiencies (corrected for the dead wire contribution) into calculating the number of hits remaining on average With dead wires and plane efficiencies removing hits, the track was then tested for viability according to the requirements for tracks described earlier. For a given bin of mass, rapidity and $cos\theta$, the efficiency was calculated as the number of tracks passing the track requirements out of those passing the geometric cuts for that bin. The efficiency correction for the bin was the reciprocal of the ratio

$$K_{EFF} = \frac{1}{\eta_{EFF}} \tag{4.7.1}$$

where

$$\eta_{EFF} = \frac{number\ of\ viable\ tracks}{number\ of\ tracks\ accepted}$$

Tables were created similar to the acceptance tables, with the exception that the entries here were averaged over p_t. The efficiency correction, as the acceptance correction, was applied to each event, using K_{EFF} from the bin corresponding to the event's kinematic variables.

4.7 Normalisation

The normalisation factor expressing the time integrated rate of proton-nucleon interaction is referred to as the "luminosity", and is defined as

$$\mathcal{L} = \frac{n_{evt}}{\sigma} \tag{4.7.1}$$

where sigma is the cross section for a particular event and n_{evt} is the number of such events that occur. The luminosity, so defined, is independent of the scattering process. An

experiment's luminosity is determined using a process for which the cross section is known and is measurable. In the present case, monitors at 90° to the target from the beamline measured some fraction of the total target nuclear interactions. The luminosity can be expressed as

$$\mathcal{L} = \int N_{inc} \times N_A \times \frac{\rho}{A}\, dz \qquad (4.7.2)$$

where

N_{inc} = number protons intercepted by target.

N_A = Avogadro's number 6.022 X 1023

ρ = density of target (g/cm^3).

A=atomic number,

dz = length of target

The targets were chosen to be ~10% of a nuclear interaction length in the z direction. The narrowness in the x (horizontal) direction provided a good vertex constraint, but did not entirely contain the beam width. Typically the beam fraction incident on the target was around 90%, so not only the beam count, but an indication of target interception was necessary to determine the total beam-target interaction rate. The expression for the the number of protons intercepted by the target at a depth z becomes

$$N_{inc} = N_{beam} \times F_{xy} \times \exp(-\frac{z}{\lambda}) \qquad (4.7.3)$$

where F_{xy} is the fraction of the beam intercepted by a given target. The exponential term describes the depletion of the beam as its protons interact with the target nucleons where λ is the nuclear interaction length of the target material.

Each luminosity monitor intercepted some small fraction of the total nuclear interactions. Counts on a given luminosity monitor over a 20 second beam spill were be parametrised as

$$N_{mon} = (c_1 \times F_{xy} + c_2) \times N_{beam} \qquad (4.7.4)$$

N_{beam} was the number protons in the beam per spill, and this could be expressed in terms of the ion chamber (NECIC) counts,

$$N_{beam} = N_{NECIC} \times c_3 \tag{4.7.5}$$

The ion chamber measured the total number of protons in a 20 second beam spill. It was calibrated against scintillation counters placed in the beamline with low intensity beam (~10^5 protons/sec). The constant c_3 was the ratio of the scintillator counts for each count on NECIC. Figure 4.7 shows data from a low intensity run.

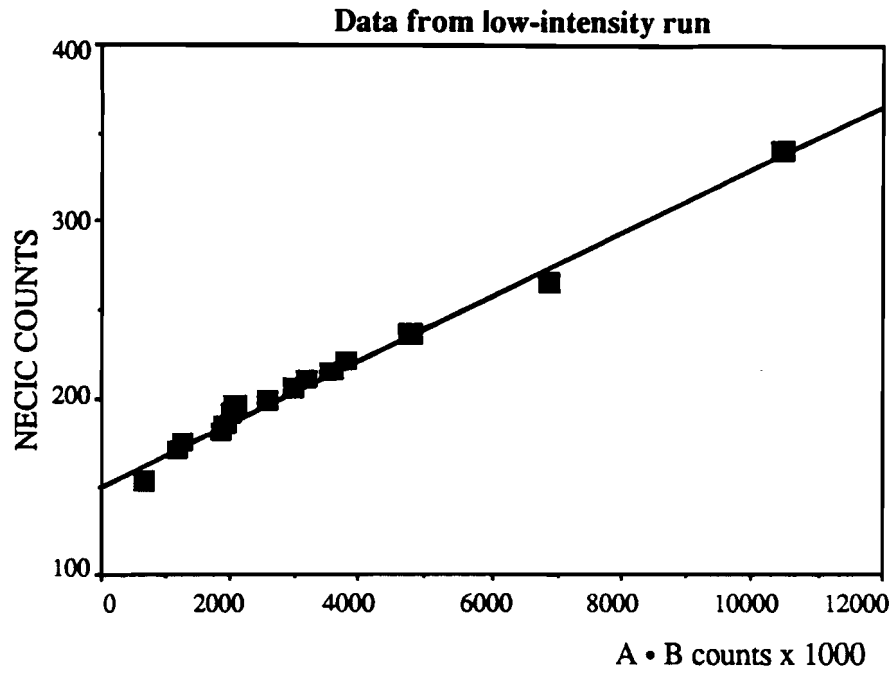

Figure 4.7
NECIC beam monitor calibrated against scintillation counters in low intensity run. Inverse of slope gives calibration constant c_3

The individual luminosity monitor calibration constants were determined by a "target scan". This was done using the horizontal deflection magnet NECH upstream in the beamline that moved the beam in the x direction by a known amount for a given increment in its current setting. Figure 4.8 shows the current increments in NECH plotted against the horizontal deflection of the beam as measured in wire chamber NEEPWC. The ratio of counts on a given luminosity monitor to the output from the beam monitor (NECIC) over a 20-second spill was plotted versus the beam centre position in x (from the

current settings in NECH). A typical target scan for one of the luminosity monitors is presented in Figure 4.9. The target scan data suggested that the beam profile could be parametrised by a Gaussian distribution. This was done using MINUIT to determine the constants c_1 and c_2 as well as a width and centre for the target scan profile. F_{xy} was then determined using the normalised Gaussian integral

$$F_{xy} = \frac{1}{\sqrt{2\pi\sigma_b}} \int_{x=x_0-w/2}^{x=x_0+w/2} \exp\left[-\frac{(x-x_b)^2}{2\sigma^2}\right] dx. \qquad (4.7.6)$$

The target width (w) and position (x_0) are known previous to any particular scan. The constant c_2 in the equation (4.6.4) was found to be equal to N_{mon}/N_{beam} for each monitor when the target was removed, so was independent of target. From the fitted target scan data

$$c_1 = \left(\frac{N_{mon}}{N_{NECIC} \times c_3} - c_2\right) / F_{xy}. \qquad (4.7.7)$$

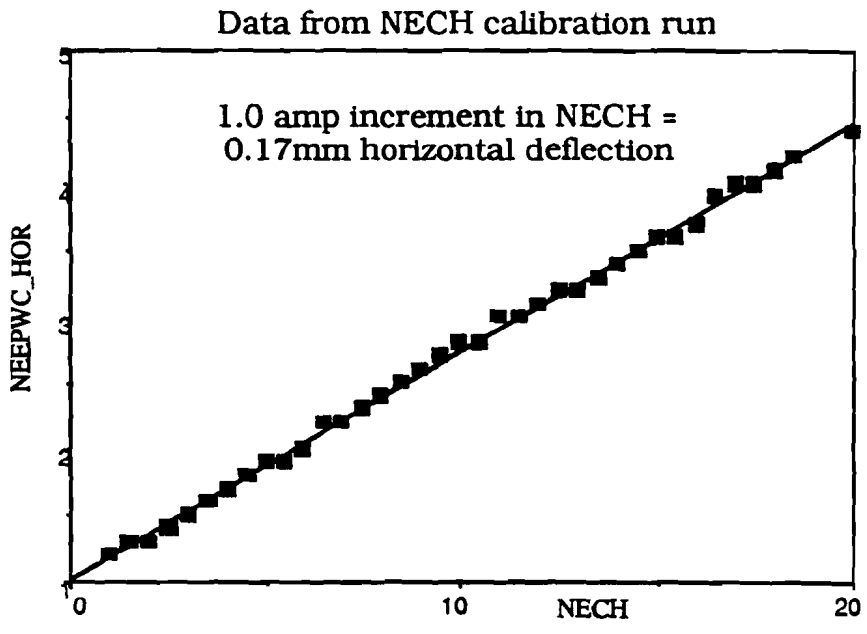

Figure 4.8
Calibration of the horizontal deflecting magnet NECH

With c_1, c_2 and c_3 determined, the targeting ratio F_{xy} for any random position of the beam relative to the target can be expressed from the data as

$$F_{xy} = \frac{N_{mon} - N_{NECIC} \cdot c_3 \cdot c_2}{c_1} \tag{4.7.8}$$

The integrated luminosity for each beam spill was calculated from the each luminosity monitor to be

$$\mathcal{L}_{spill} = \frac{(N_{NECIC} \cdot c_3) \times (N_{mon} - \cdot N_{NECIC} \cdot c_3 \cdot c_2)}{c_1} \times \frac{N_A \cdot \rho \cdot \lambda (1 - e^{-L_T})}{A} \tag{4.7.9}$$

where L_T is the length, in interaction lengths, of the target (see section 2.3 for exact target lengths).

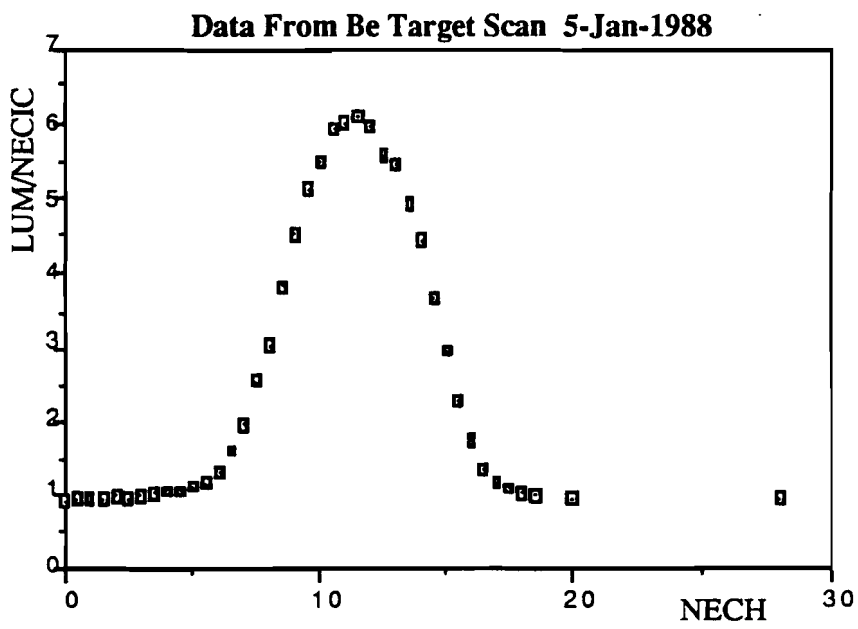

Figure 4.9
Example of a target scan

The four individual monitors agreed to within 3%, eliminating any directional bias in the interaction count. The statistical errors inherent in using scintillation

counters were negligible. The systematic error from the ion chamber calibration was estimated to be 2% (the spread from successive calibration runs). The other systematic errors came from change in the beam spot shape which altered the value of the luminosity constants described above. These were estimated at less than 4% for the beryllium targets, and less than 2% for iron, aluminum and tungsten. Table 4.7 shows the calculated luminosities for each target.

Target	Q•P•M	MHI Pairs
Be	1.563×10^{13}	1.778×10^{13}
Al	5.794×10^{12}	5.797×10^{12}
Fe	1.464×10^{13}	1.484×10^{13}
W	9.339×10^{12}	3.017×10^{13}

Table 4.7

Total integrated luminosity in barn^{-1} per nucleon

4.8 Background

The experiment was designed to trigger on a pair of high-p_t hadrons. The background from any other interaction with the target was considered neglible. However, high-p_t pairs could be produced from the target stand and the surrounding air. It was also considered possible for single, uncorrelated high-p_t hadrons to simulate a correlated pair.

For the latter concern, Q • P • M signals (described in the last chapter) from top half of the calorimeter were delayed with respect to those from the bottom, and put into a separate coincidence module. The coincidence rate as a function of the delay time was recorded during a data-taking run, and was found to be neglible with delay times of more than the width of a logic signal (Figure 4.10). This was consistent with a calculation done using single hadron production data[12] in the range of the rapidity and Φ of the E711 detector.

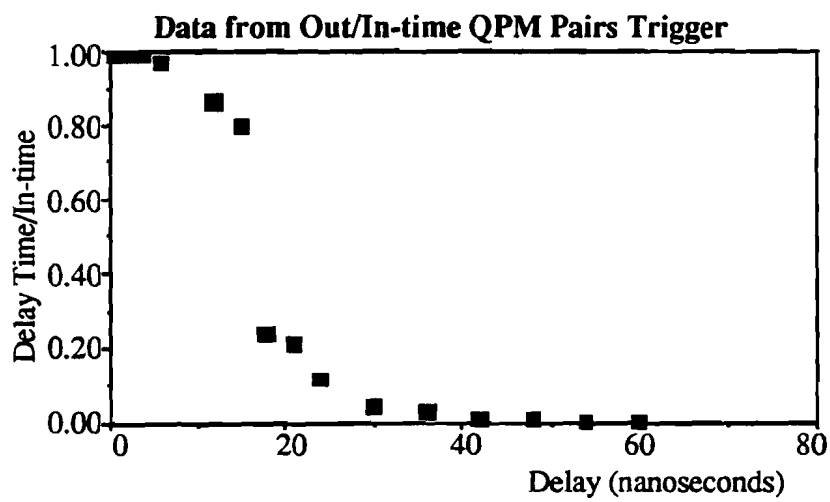

Figure 4.10
Delay curves for pairs trigger

To determine the pairs production apart from interactions with the targets, runs were taken with the target removed but the target stand still in place. The analysis was conducted exactly as for the target data. Using the luminosity from these runs, a

background percentage, normalised for each of the targets, was calculated. These are given in Table 4.8

Target	% Events From Non-target Interactions
Al	1.4
Be	2.7
Fe	1.2
W	1.0

Table 4.8
Percentage of background events

The statistical error on each background calculation is 20% of its value. In constructing the cross sections presented in the next chapter, these were used to correct the luminosity for each target sample.

CHAPTER 5

MASS AND ANGULAR DISTRIBUTIONS

The results of the analysis described in the previous chapter are presented here. Mass cross sections for the opposite sign, positive sign and negative sign dihadrons are shown for each target data set. Normalised angular distributions for the +-, ++ and -- are shown for low mass and high mass data separately.

5.1 Cross sections

The differential cross sections as a function of mass and $cos\theta$ can be expressed in terms of the luminosity, efficiencies and the number of observed events as

$$\frac{d^2\sigma}{dMdy} = \frac{1}{\Delta M \Delta Y \cdot eff_{TRIG} eff_{TRK}} \cdot \mathcal{L}^{-1} \cdot \int \frac{d^4 N'_{event}}{dMdYdP_T d\cos\theta} dMdYd\cos\theta dP_T \qquad (5.1.1)$$

and

$$\frac{d^3\sigma}{dMdyd\cos\theta} = \frac{1}{\Delta M \Delta Y \Delta\cos\theta \cdot eff_{TRIG} \cdot eff_{TRK}} \mathcal{L}^{-1} \cdot \int \frac{d^4 N'_{event}}{dMdYdP_T d\cos\theta} dMdYd\cos\theta dP_T. \qquad (5.1.2)$$

where eff_{TRIG} and eff_{TRK} are the trigger and track efficiencies described earlier, and N'_{event} is the number of events in a given bin of phase space N_{event}, corrected by the detector acceptance K_{acc}, and detector efficiency K_{eff}. ΔM , ΔY and $\Delta cos\theta$ are the widths of the M, Y and $cos\theta$ integrations.

5.1.1 *Differential cross sections in mass*

For the mass cross section, the widths ΔM varied as the steepness of the mass distribution required bins of higher mass be wider to provide an adequate number of entries per bin. The single bin of rapidity had width $\Delta Y = 0.3$ and was centred around Y=0.0. The magnitude of the transverse momentum of the hadron pair p_t was restricted to $|p_t|$ of 3 GeV/c or less. The integration in $cos\theta$ had the limits of the distributions presented in this chapter, $0.0 < cos\theta < 0.5$. With these limits the differential mass cross sections were calculated as

$$\left.\frac{d^2\sigma}{dMdY}\right|_{Y=0} = \frac{1}{\Delta Y \Delta M}\int_{M-\Delta M}^{M+\Delta M} dM \int_{-0.15}^{0.15} dY \int_{0.0}^{3.0} dP_T \int d|\cos\theta| \frac{d^4\sigma}{dMdYdP_T d|\cos\theta|}, \qquad (5.1.3)$$

Figures 5.1 and 5.2 show the cuts placed on the raw data p_t and rapidity distributions.

The mass cross section in terms of the physical quantities was calculated as

$$\left.\frac{d^2\sigma}{dMdY}\right|_{Y=0} = \mathcal{L}^{-1}\frac{N'_{events}}{\varepsilon_{TRIG}\varepsilon_{TRK}\Delta M \Delta Y} \qquad (5.1.4)$$

where N'_{event}, $\mathcal{L}$, eff_{TRIG} and eff_{TRK} are the same quantities used in 5.1.1 and 5.1.2. These were described in the last chapter. The background due to interactions other than those from the target was incorporated as a correction to the luminosity for each target (see section 4.7). Two types of triggers were accepted as signalling physics events. These were the Q • P • M and the MHI triggers, whose thresholds were set at 6.0 and 8.5 GeV/c2 respectively, but whose components were identical. The Q • P • M trigger was prescaled (reduced), typically by a factor of 2, from the MHI trigger to allow for a greater sample of the relatively rare higher mass events. Running two different triggers complicated the cross section calculation somewhat as data could be considered as coming from two different experiments, each with a different effective luminosity. For this analysis, the data were separated into 2 sets, those setting an MHI trigger, and those setting a Q • P • M trigger latch that did not also set an MHI latch (to avoid double counting). The

luminosities (shown in Table 4.5) were calculated for each trigger separately, then applied in equation 5.1.4 to the corresponding data set. The two data sets were added together after going through separate analyses.

The mass differential cross section per nucleon are shown in Figures 5.3 - 5.5. The values of each entry are shown in tables 5.1 - 5.4. The curves shown are from a Monte Carlo calculation folding in QCD calculations, parton fragmentation and structure functions, as well as the phase space restrictions of the analysis. This is discussed in chapter 6. The errors shown on the tables and plots are statistical. The total systematic error on the mass cross sections was estimated to be 14%. This came from the sum of the uncorrelated systematic errors from the luminosity monitor calibration (4%), uncertainty in the ion chamber calibration (2%) and the systematic uncertainty in the drift chamber efficiency (8%). In addition, the first mass bin (6.5 to 7.0 GeV/c^2) had a 5% error in the trigger efficiency determination.

5.1.2 *Angular distributions*

The E711 detector was designed for angular acceptance of $-0.6 < \cos\theta < 0.6$ in the proton-nucleon c.m.frame (θ being the polar angle with respect to the incoming proton direction). Because the reconstructed dihadron centre of mass could vary considerably from that of the proton-target system due to fragmentation and initial parton motion within the nucleons, the angular acceptance for dihadron pairs could only be reasonably studied in the range $5. < \cos\theta < .5$. The $\cos\theta$ distribution was calculated as

$$\left.\frac{d^2\sigma}{dMdYd|\cos\theta|}\right|_{Y=0} = \frac{N'_{event}}{\varepsilon_{TRIG}\varepsilon_{TRK}\Delta M\Delta Y\Delta|\cos\theta|}\mathcal{L}^1 \quad . \tag{5.1.4}$$

The $\cos\theta$ cross sections were determined in two bins of mass, $6.5 < M < 7.5$ and $7.5 < M < 15.0$. In order to obtain reasonable statistics, data from all four targets were included in each plot. Since the shape is of more interest here than the normalisation (which is

already established by the cross sections with respect to mass), the angular distributions here will be normalised to unity at $cos\theta = 0$.

Figures 5.6 through 5.11 and tables 5.5 through 5.10 present the data for the angular distributions for the three charge states of the dihadrons, ++, -- and +-, in a higher and lower mass range.The plots also show a parametrisation of QCD calculation.Table 5.11 summarises the fits to this parametrisation with the values predicted by QCD.The errors presented are statistical. The magnetic field maps indicated that the field was uniform to within a percent, which implied a 1% error in momentum reconstruction. A Monte Carlo calculation determined that the worst error in the $cos\ \theta$ reconstruction , given the largest difference in p_t kick due to field inhomogeneity, was no more than 4%. The error from "misbinning" in the acceptance calculation due to error in the mass reconstruction was estimated to be less than 5%. Another source of systematic error is from the determination of the chamber efficiencies as a function of angle. This was estimated at around 4% from the largest variance in values for the phase space bin efficiency in successive runs of the acceptance/efficiency Monte Carlo. Assuming these are uncorrelated, the total systematic error on the angular distributions is estimated to be less than 13%.

5.1.3 *Ratios of charge states*

Figures 5.12 through 5.14 present ratios of events produced as a function of mass. These ratios are # events (++)/#events(--), #events(+-)/#events(++) and #events(+-)/#events(--). This was a check on the consistency of QCD predictions that is independent of luminosity. These are presented for data from each target. The solid lines show the data, and the dashed lines give the QCD prediction.

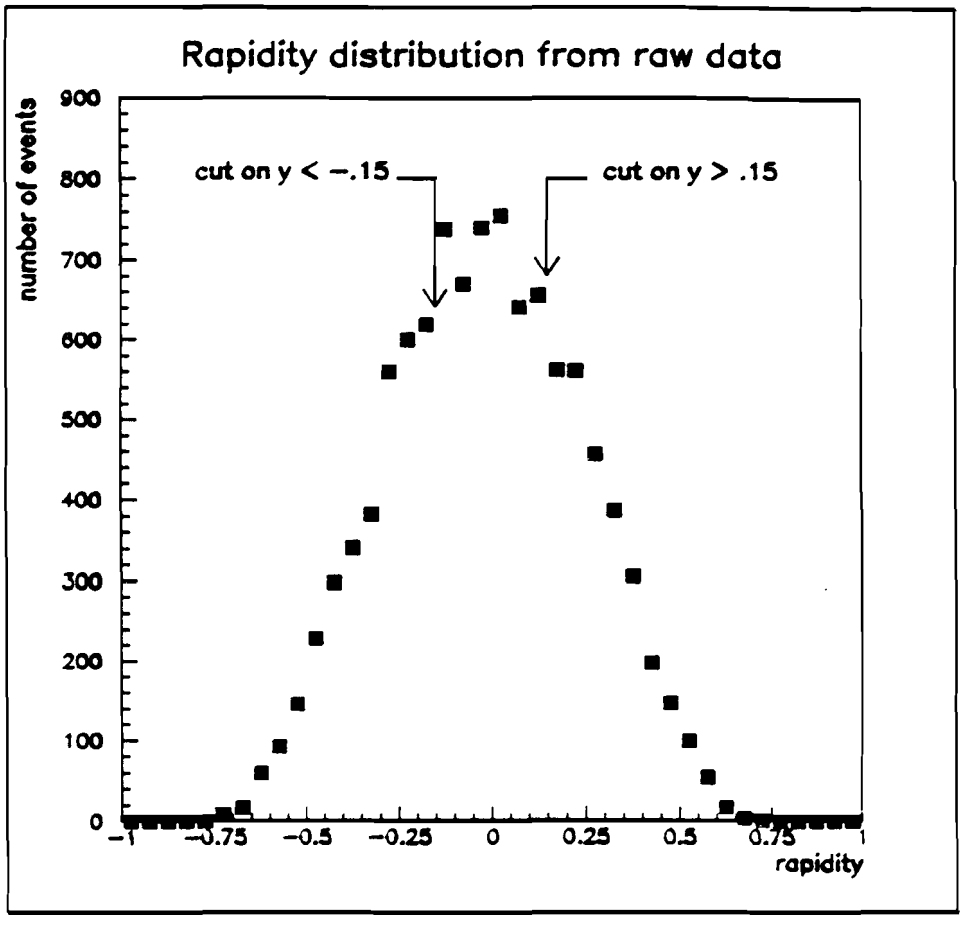

Figure 5.1
Phase space cut in rapidity for final data sample

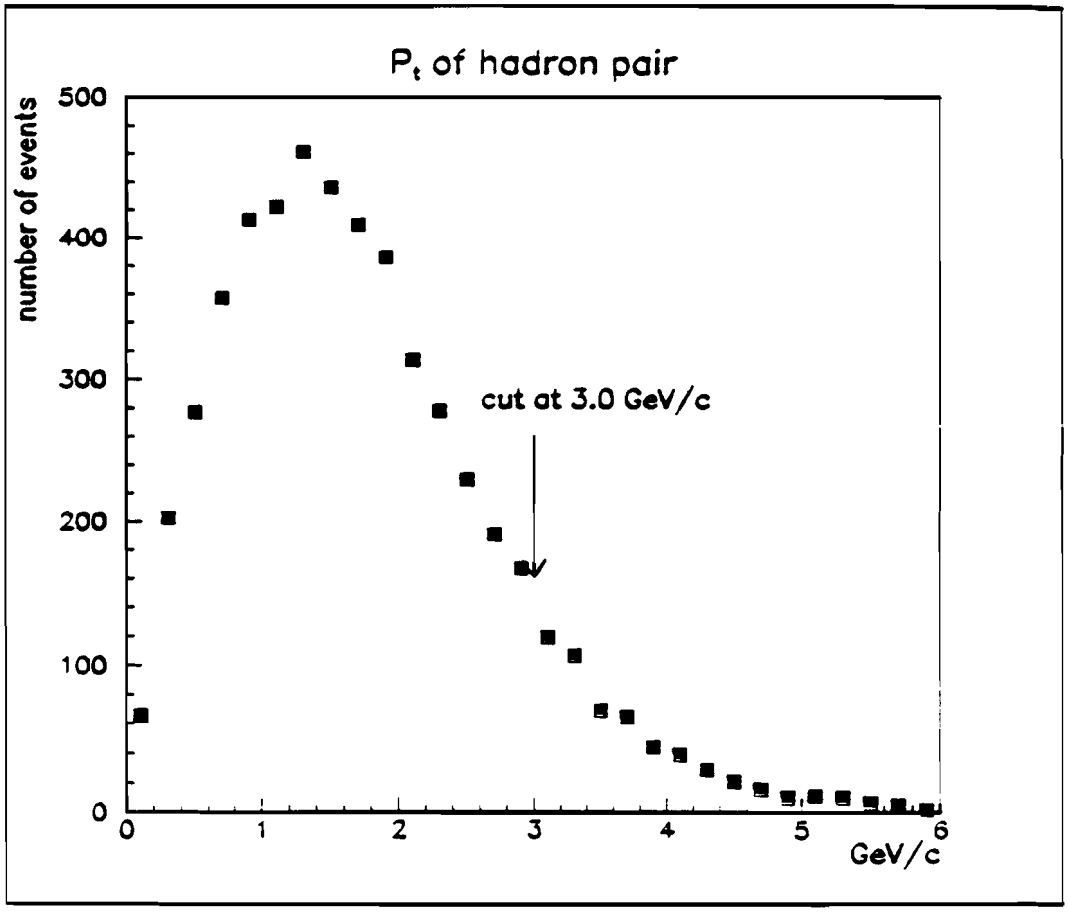

Figure 5.2
Phase space cut in p_t of the pair for final data sample

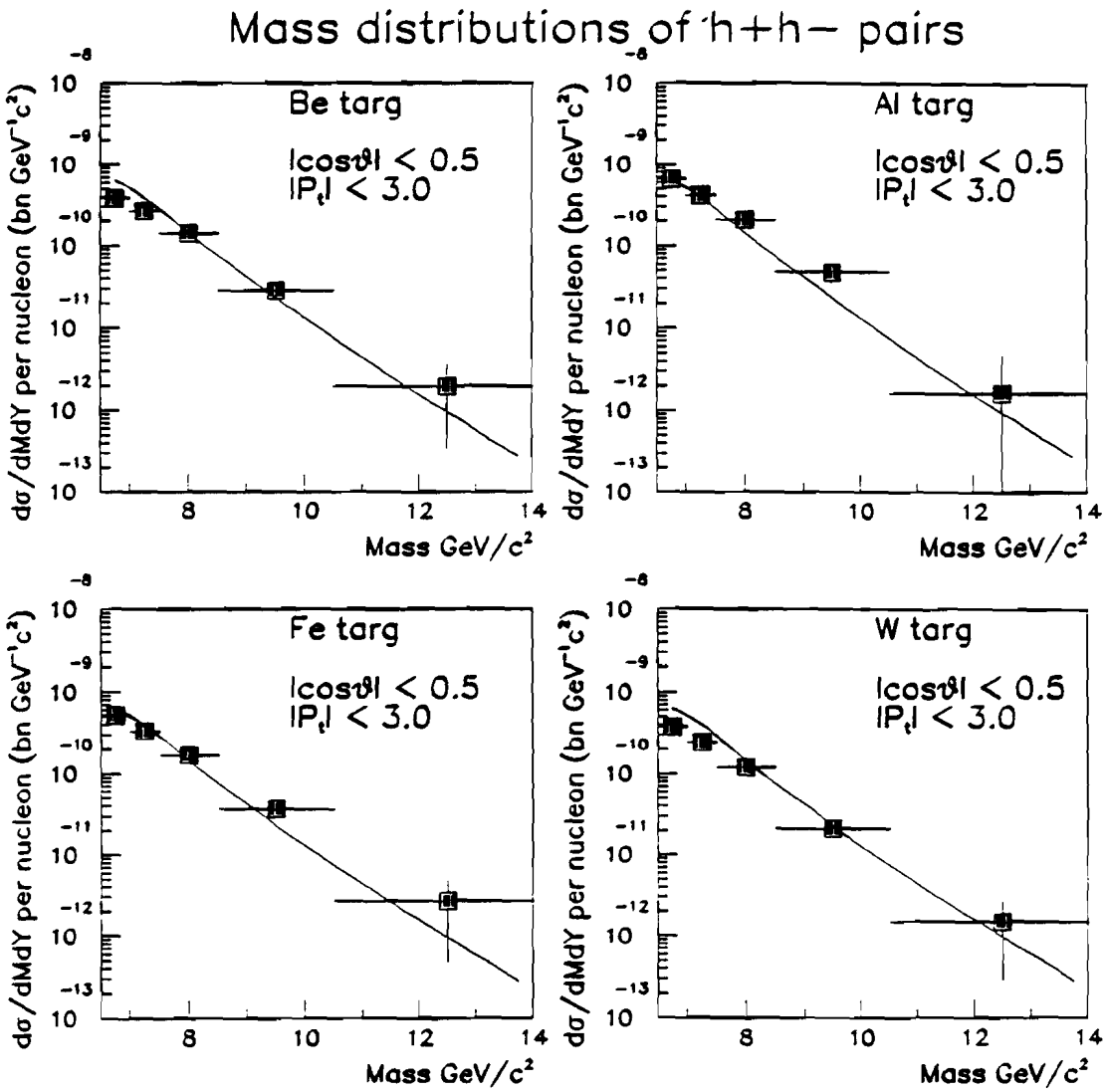

Figure 5.3
Differential mass cross sections for the + - Dihadron charge state.
Solid line shows QCD calculation.

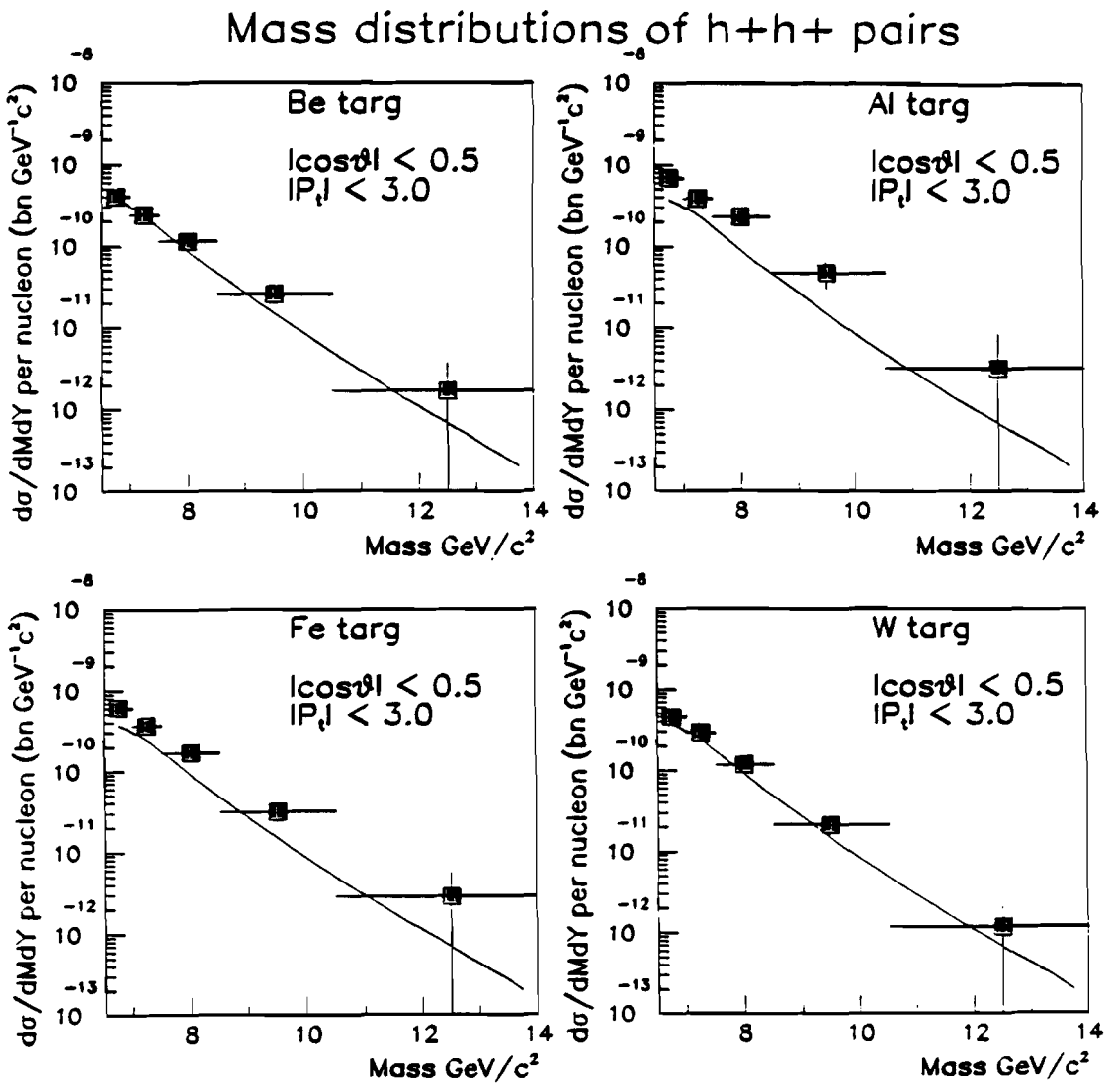

Figure 5.4
Differential mass cross sections for the + + Dihadron charge state.
Solid line shows QCD calculation.

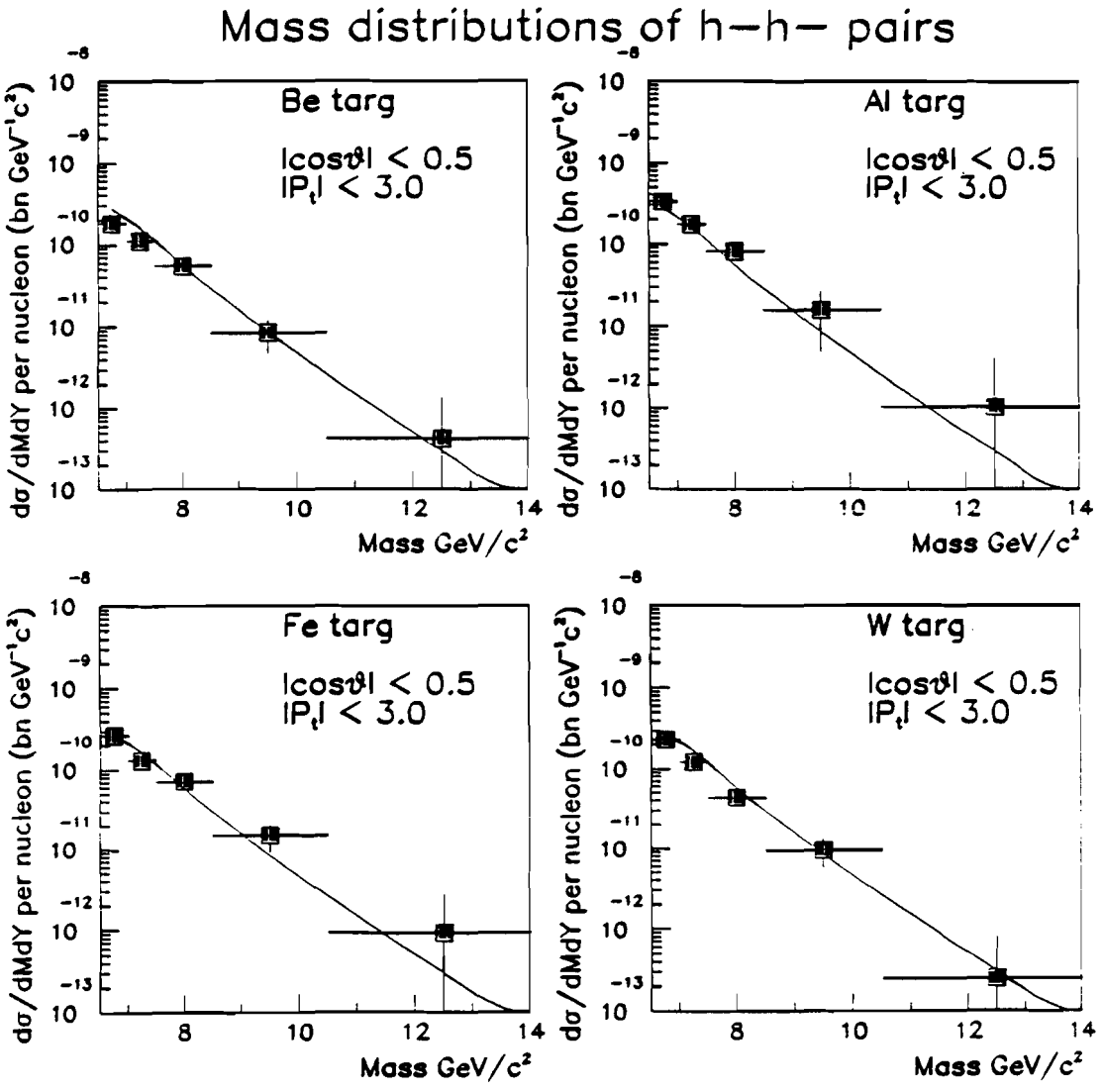

Figure 5.5

Differential mass cross sections for the - - Dihadron charge state.
Solid line shows QCD calculation.

+ - Mass Range Gev/c^2	Weighted Mass Gev/c^2	$\frac{d^2\sigma}{dMdY}$ $barns\ GeV^{-1}c^2$
6.5 – 7.0	6.74	$5.08 \pm 0.11 \times 10^{-10}$
7.0 – 7.5	7.19	$2.65 \pm 0.07 \times 10^{-10}$
7.5 – 8.5	7.92	$1.48 \pm 0.08 \times 10^{-10}$
8.5 – 10.5	9.20	$2.81 \pm 0.48 \times 10^{-11}$
10.5 – 15.0	11.80	$1.87 \pm 1.69 \times 10^{-12}$

+ + Mass Range Gev/c^2	Weighted Mass Gev/c^2	$\frac{d^2\sigma}{dMdY}$ $barns\ GeV^{-1}c^2$
6.5 – 7.0	6.74	$4.51 \pm 0.17 \times 10^{-10}$
7.0 – 7.5	7.22	$2.34 \pm 0.11 \times 10^{-10}$
7.5 – 8.5	7.91	$1.07 \pm 0.11 \times 10^{-10}$
8.5 – 10.5	9.13	$2.43 \pm 0.62 \times 10^{-11}$
10.5 – 15.0	11.01	$1.52 \pm 2.06 \times 10^{-12}$

- - Mass Range Gev/c^2	Weighted Mass Gev/c^2	$\frac{d^2\sigma}{dMdY}$ $barns\ GeV^{-1}c^2$
6.5 – 7.0	6.73	$1.91 \pm 0.11 \times 10^{-9}$
7.0 – 7.5	7.25	$1.19 \pm 0.08 \times 10^{-9}$
7.5 – 8.5	7.87	$5.56 \pm 0.79 \times 10^{-10}$
8.5 – 10.5	9.14	$8.69 \pm 3.82 \times 10^{-12}$
10.5 – 15.0	11.86	$4.36 \pm 10.1 \times 10^{-13}$

Table 5.1
Data for the differential mass cross sections from the beryllium target.

+ - Mass Range Gev/c^2	Weighted Mass Gev/c^2	$\frac{d^2\sigma}{dMdY}$ $barns\ GeV^{-1}c^2$
6.5 – 7.0	6.74	$1.03 \pm 0.03 \times 10^{-9}$
7.0 – 7.5	7.24	$5.37 \pm 0.18 \times 10^{-10}$
7.5 – 8.5	7.89	$2.62 \pm 0.19 \times 10^{-10}$
8.5 – 10.5	9.31	$5.81 \pm 1.23 \times 10^{-11}$
10.5 – 15.0	11.50	$1.59 \pm 2.76 \times 10^{-12}$

+ + Mass Range Gev/c^2	Weighted Mass Gev/c^2	$\frac{d^2\sigma}{dMdY}$ $barns\ GeV^{-1}c^2$
6.5 – 7.0	6.75	$9.75 \pm 0.43 \times 10^{-10}$
7.0 – 7.5	7.21	$4.84 \pm 0.27 \times 10^{-10}$
7.5 – 8.5	7.81	$2.91 \pm 0.33 \times 10^{-10}$
8.5 – 10.5	9.10	$5.94 \pm 1.77 \times 10^{-11}$
10.5 – 15.0	11.23	$3.71 \pm 5.52 \times 10^{-12}$

- - Mass Range Gev/c^2	Weighted Mass Gev/c^2	$\frac{d^2\sigma}{dMdY}$ $barns\ GeV^{-1}c^2$
6.5 – 7.0	6.74	$4.48 \pm 0.30 \times 10^{-10}$
7.0 – 7.5	7.26	$2.36 \pm 0.20 \times 10^{-10}$
7.5 – 8.5	7.92	$1.03 \pm 0.19 \times 10^{-10}$
8.5 – 10.5	8.97	$1.85 \pm 1.02 \times 10^{-11}$
10.5 – 15.0	10.50	$1.25 \pm 3.40 \times 10^{-12}$

Table 5.2
Data for the differential mass cross sections from the aluminum target.

+ - Mass Range Gev/c^2	Weighted Mass Gev/c^2	$\frac{d^2\sigma}{dMdY}$ $barns\ GeV^{-1}c^2$
6.5 – 7.0	6.75	$7.21 \pm 0.15 \times 10^{-10}$
7.0 – 7.5	7.25	$3.66 \pm 0.09 \times 10^{-10}$
7.5 – 8.5	7.90	$1.82 \pm 0.10 \times 10^{-10}$
8.5 – 10.5	9.30	$3.83 \pm 0.61 \times 10^{-11}$
10.5 – 15.0	11.22	$2.57 \pm 2.28 \times 10^{-12}$

+ + Mass Range Gev/c^2	Weighted Mass Gev/c^2	$\frac{d^2\sigma}{dMdY}$ $barns\ GeV^{-1}c^2$
6.5 – 7.0	6.74	$7.52 \pm 0.25 \times 10^{-10}$
7.0 – 7.5	7.20	$3.71 \pm 0.15 \times 10^{-10}$
7.5 – 8.5	7.93	$1.71 \pm 0.15 \times 10^{-10}$
8.5 – 10.5	9.24	$3.32 \pm 0.79 \times 10^{-11}$
10.5 – 15.0	11.01	$2.66 \pm 2.91 \times 10^{-12}$

- - Mass Range Gev/c^2	Weighted Mass Gev/c^2	$\frac{d^2\sigma}{dMdY}$ $barns\ GeV^{-1}c^2$
6.5 – 7.0	6.73	$3.26 \pm 0.16 \times 10^{-10}$
7.0 – 7.5	7.23	$1.35 \pm 0.89 \times 10^{-10}$
7.5 – 8.5	7.88	$7.58 \pm 0.10 \times 10^{-11}$
8.5 – 10.5	9.20	$1.60 \pm 0.59 \times 10^{-11}$
10.5 – 15.0	10.91	$8.70 \pm 1.81 \times 10^{-12}$

Table 5.3
Data for the differential mass cross sections from the iron target.

+ - Mass Range Gev/c^2	Weighted Mass Gev/c^2	$\frac{d^2\sigma}{dMdY}$ $barns\ GeV^{-1}c^2$
6.5 – 7.0	6.74	$5.31 \pm 1.36 \times 10^{-10}$
7.0 – 7.5	7.26	$2.69 \pm 0.08 \times 10^{-10}$
7.5 – 8.5	7.91	$1.40 \pm 0.09 \times 10^{-10}$
8.5 – 10.5	9.10	$2.33 \pm 0.39 \times 10^{-11}$
10.5 – 15.0	11.43	$1.32 \pm 1.19 \times 10^{-12}$

+ + Mass Range Gev/c^2	Weighted Mass Gev/c^2	$\frac{d^2\sigma}{dMdY}$ $barns\ GeV^{-1}c^2$
6.5 – 7.0	6.70	$4.74 \pm 0.20 \times 10^{-10}$
7.0 – 7.5	7.25	$2.72 \pm 0.13 \times 10^{-10}$
7.5 – 8.5	7.92	$1.16 \pm 0.11 \times 10^{-10}$
8.5 – 10.5	9.36	$2.17 \pm 0.55 \times 10^{-11}$
10.5 – 15.0	10.70	$1.03 \pm 1.24 \times 10^{-12}$

- - Mass Range Gev/c^2	Weighted Mass Gev/c^2	$\frac{d^2\sigma}{dMdY}$ $barns\ GeV^{-1}c^2$
6.5 – 7.0	6.73	$2.62 \pm 0.53 \times 10^{-10}$
7.0 – 7.5	7.29	$1.30 \pm 0.09 \times 10^{-10}$
7.5 – 8.5	7.97	$4.75 \pm 0.73 \times 10^{-11}$
8.5 – 10.5	9.00	$9.63 \pm 3.89 \times 10^{-12}$
10.5 – 15.0	10.32	$2.19 \pm 5.49 \times 10^{-13}$

Table 5.4
Data for the differential mass cross sections from the Tungsten target.

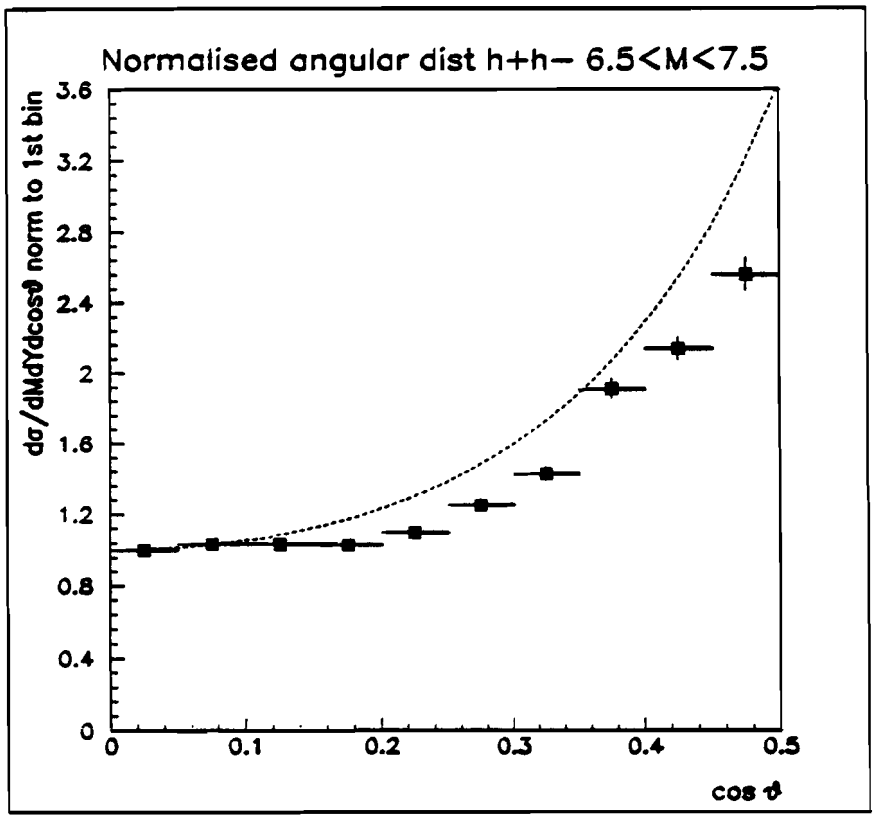

Figure 5.6

Plot of normalised *cosθ* distribution for + - pairs at 6.5<M<7.5 Gev/c^2

Cos θ Range	Cos θ Normalised To First Bin
0.00 - 0.05	$1.00 \pm 3.21 \times 10^{-2}$
0.05 - 0.10	$1.03 \pm 3.27 \times 10^{-2}$
0.10 - 0.15	$1.03 \pm 3.31 \times 10^{-2}$
0.15 - 0.20	$1.03 \pm 3.28 \times 10^{-2}$
0.20 - 0.25	$1.10 \pm 3.46 \times 10^{-2}$
0.25 - 0.30	$1.25 \pm 3.73 \times 10^{-2}$
0.30 - 0.35	$1.42 \pm 4.19 \times 10^{-2}$
0.35 - 0.40	$1.91 \pm 5.66 \times 10^{-2}$
0.40 - 0.45	$2.13 \pm 6.79 \times 10^{-2}$
0.45 - 0.50	$2.56 \pm 9.51 \times 10^{-2}$

Table 5.5

Values for normalised *cosθ* distribution for + - pairs at 6.5<M<7.5 Gev/c^2

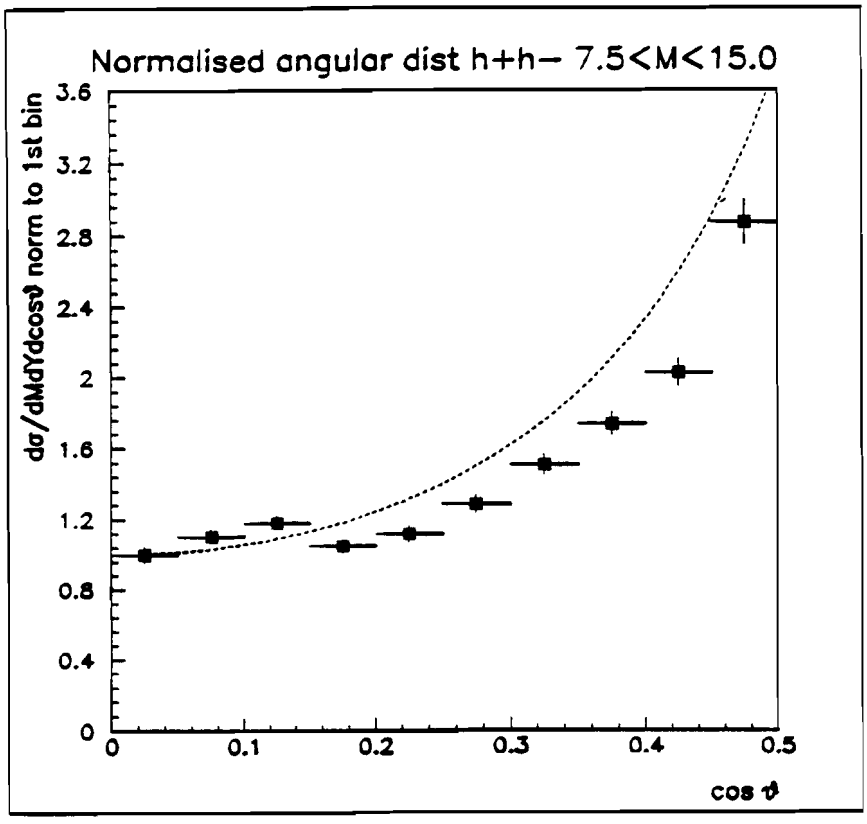

Figure 5.7

Plot of normalised $cos\theta$ distribution for+ - pairs at $7.5<M<15.0$ Gev/c^2

Cos θ Range	Cos θ Normalised To First Bin
0.00 - 0.05	$1.00 \pm 4.65 \times 10^{-2}$
0.05 - 0.10	$1.10 \pm 4.86 \times 10^{-2}$
0.10 - 0.15	$1.17 \pm 5.03 \times 10^{-2}$
0.15 - 0.20	$1.04 \pm 4.75 \times 10^{-2}$
0.20 - 0.25	$1.11 \pm 4.91 \times 10^{-2}$
0.25 - 0.30	$1.28 \pm 5.27 \times 10^{-2}$
0.30 - 0.35	$1.50 \pm 5.89 \times 10^{-2}$
0.35 - 0.40	$1.73 \pm 6.71 \times 10^{-2}$
0.40 - 0.45	$2.02 \pm 7.90 \times 10^{-2}$
0.45 - 0.50	$2.87 \pm 1.24 \times 10^{-1}$

Table 5.6

Values for normalised $cos\theta$ distribution for + - pairs at $7.5<M<15.0$ Gev/c^2

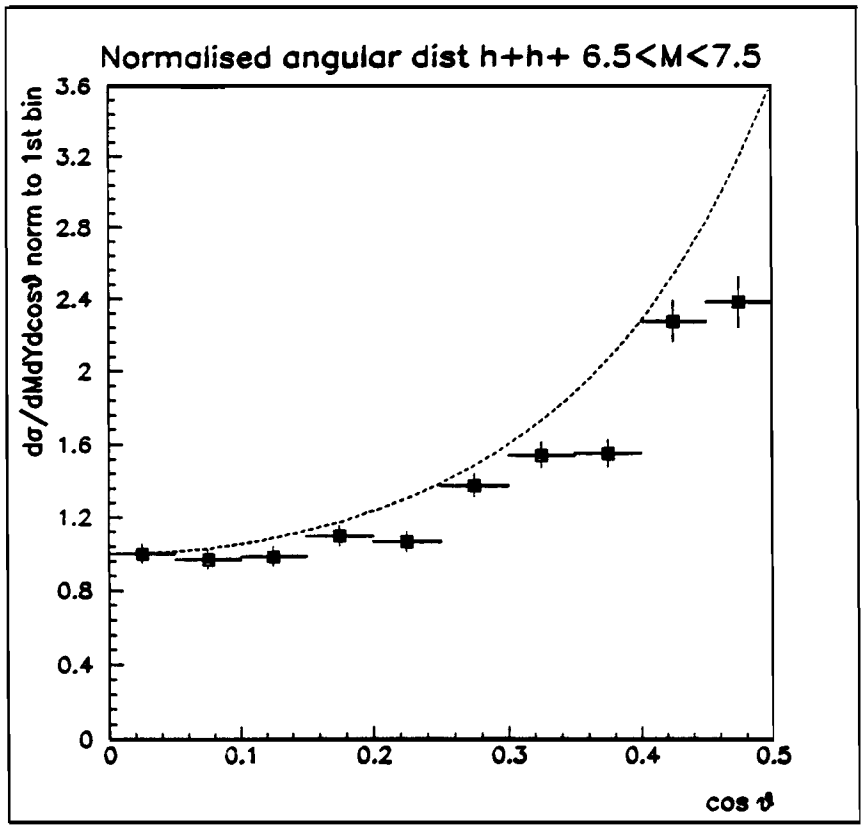

Figure 5.8

Plot of normalised *cosθ* distribution for + + pairs at 6.5<M<7.5 Gev/c^2

Cos θ Range	Cos θ Normalised To First Bin
0.00 - 0.05	$1.00 \pm 5.43 \times 10^{-2}$
0.05 - 0.10	$0.96 \pm 5.31 \times 10^{-2}$
0.10 - 0.15	$0.98 \pm 5.43 \times 10^{-2}$
0.15 - 0.20	$1.09 \pm 5.76 \times 10^{-2}$
0.20 - 0.25	$1.06 \pm 5.62 \times 10^{-2}$
0.25 - 0.30	$1.37 \pm 6.58 \times 10^{-2}$
0.30 - 0.35	$1.53 \pm 7.29 \times 10^{-2}$
0.35 - 0.40	$1.54 \pm 7.68 \times 10^{-2}$
0.40 - 0.45	$2.27 \pm 1.14 \times 10^{-1}$
0.45 - 0.50	$2.38 \pm 1.40 \times 10^{-1}$

Table 5.7

Values for normalised *cosθ* distribution for + + pairs at 6.5<M<7.5 Gev/c^2

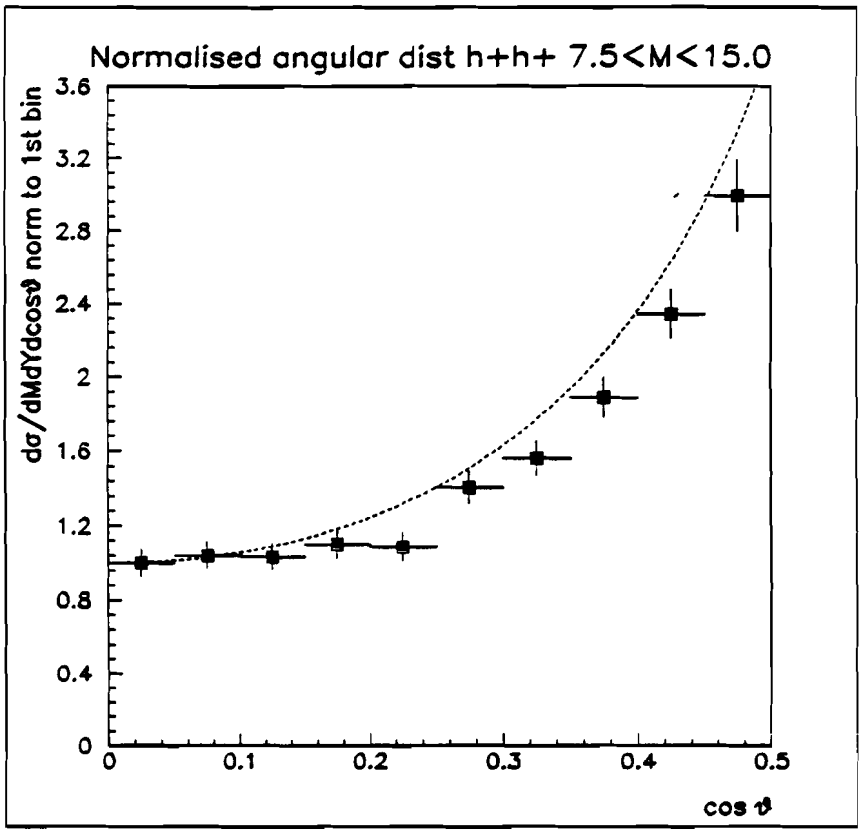

Figure 5.9

Plot of normalised *cosθ* distribution for + + pairs at 7.5<M<15.0 Gev/c^2

Cos θ Range	Cos θ Normalised To First Bin
0.00 - 0.05	$1.00 \pm 7.37 \times 10^{-2}$
0.05 - 0.10	$1.04 \pm 7.40 \times 10^{-2}$
0.10 - 0.15	$1.04 \pm 7.37 \times 10^{-2}$
0.15 - 0.20	$1.10 \pm 7.75 \times 10^{-2}$
0.20 - 0.25	$1.09 \pm 7.62 \times 10^{-2}$
0.25 - 0.30	$1.41 \pm 8.76 \times 10^{-2}$
0.30 - 0.35	$1.56 \pm 9.35 \times 10^{-2}$
0.35 - 0.40	$1.88 \pm 1.10 \times 10^{-1}$
0.40 - 0.45	$2.34 \pm 1.35 \times 10^{-1}$
0.45 - 0.50	$2.99 \pm 1.96 \times 10^{-1}$

Table 5.8

Values for normalised *cosθ* distribution for + + pairs at 7.5<M<15.0 Gev/c^2

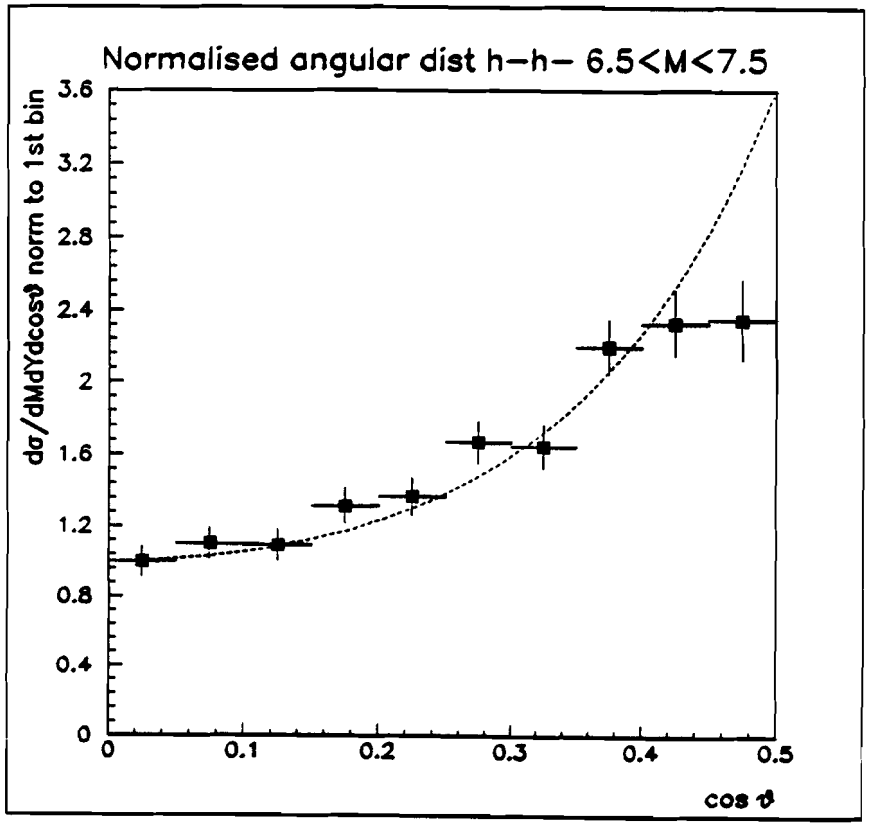

Figure 5.10

Plot of normalised $cos\theta$ distribution for - - pairs at $6.5<M<7.5 Gev/c^2$

Cos θ Range	Cos θ Normalised To First Bin
0.00 - 0.05	$1.00 \pm 8.77 \times 10^{-2}$
0.05 - 0.10	$1.10 \pm 9.02 \times 10^{-2}$
0.10 - 0.15	$1.09 \pm 9.11 \times 10^{-2}$
0.15 - 0.20	$1.32 \pm 1.03 \times 10^{-1}$
0.20 - 0.25	$1.37 \pm 1.05 \times 10^{-1}$
0.25 - 0.30	$1.67 \pm 1.18 \times 10^{-1}$
0.30 - 0.35	$1.65 \pm 1.22 \times 10^{-1}$
0.35 - 0.40	$2.20 \pm 1.52 \times 10^{-1}$
0.40 - 0.45	$2.33 \pm 1.83 \times 10^{-1}$
0.45 - 0.50	$2.35 \pm 2.22 \times 10^{-1}$

Table 5.9

Values for normalised $cos\theta$ distribution for - - pairs at $6.5<M<7.5 Gev/c^2$

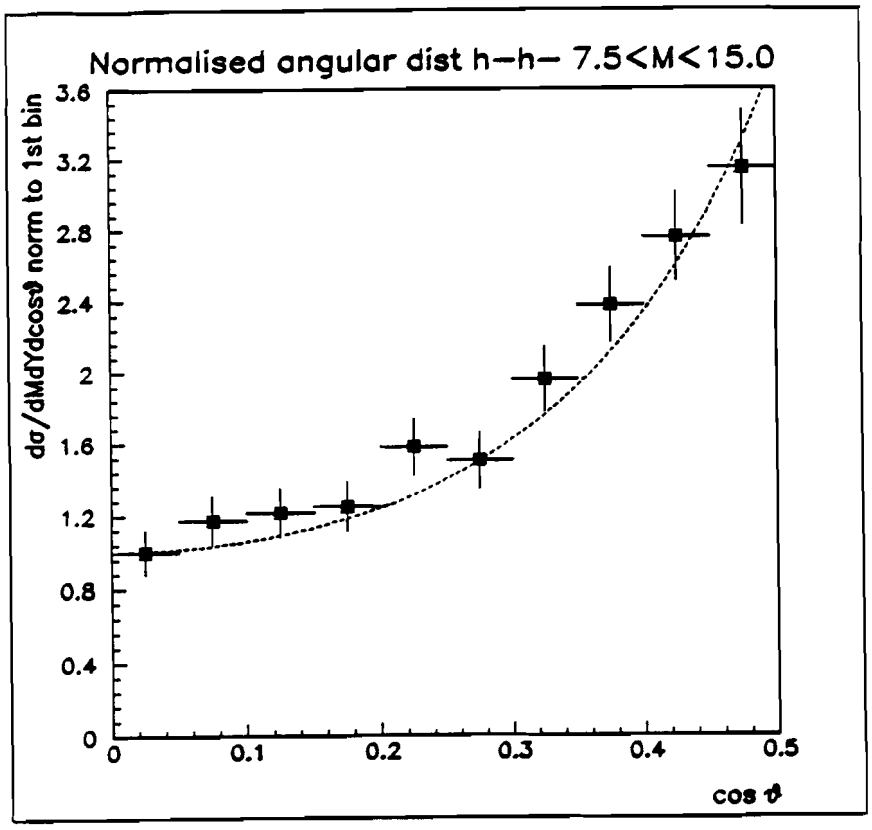

Figure 5.11

Plot of normalised $cos\theta$ distribution for - - pairs at 7.5<M<15.0 Gev/c^2

Cos θ Range	Cos θ Normalised To First Bin
0.00 - 0.05	$1.00 \pm 1.22 \times 10^{-1}$
0.05 - 0.10	$1.17 \pm 1.36 \times 10^{-1}$
0.10 - 0.15	$1.22 \pm 1.38 \times 10^{-1}$
0.15 - 0.20	$1.25 \pm 1.40 \times 10^{-1}$
0.20 - 0.25	$1.58 \pm 1.60 \times 10^{-1}$
0.25 - 0.30	$1.50 \pm 1.58 \times 10^{-1}$
0.30 - 0.35	$1.96 \pm 1.84 \times 10^{-1}$
0.35 - 0.40	$2.37 \pm 2.10 \times 10^{-1}$
0.40 - 0.45	$2.76 \pm 2.50 \times 10^{-1}$
0.45 - 0.50	$3.14 \pm 3.28 \times 10^{-1}$

Table 5.10

Values for normalised $cos\theta$ distribution for - - pairs at 7.5<M<15.0 Gev/c^2

Fit to $\frac{1}{2}\left(\frac{1}{(1-\cos\theta)^n}+\frac{1}{(1+\cos\theta)^n}\right)$			
$Cos\,\theta$ Distribution	n	χ^2	QCD n
+ - Low Mass	2.35	4.85	2.80
+ - High Mass	2.38	2.96	2.84
+ + Low Mass	2.28	2.30	2.79
+ + High Mass	2.58	8.17×10^{-1}	2.87
- - Low Mass	2.62	1.92	2.79
- - High Mass	2.81	9.80×10^{-1}	2.85

Table 5.11
Cosθ distributions fit to parametrisation in variable '*n*'.
QCD preciction for *n* shown in far right column

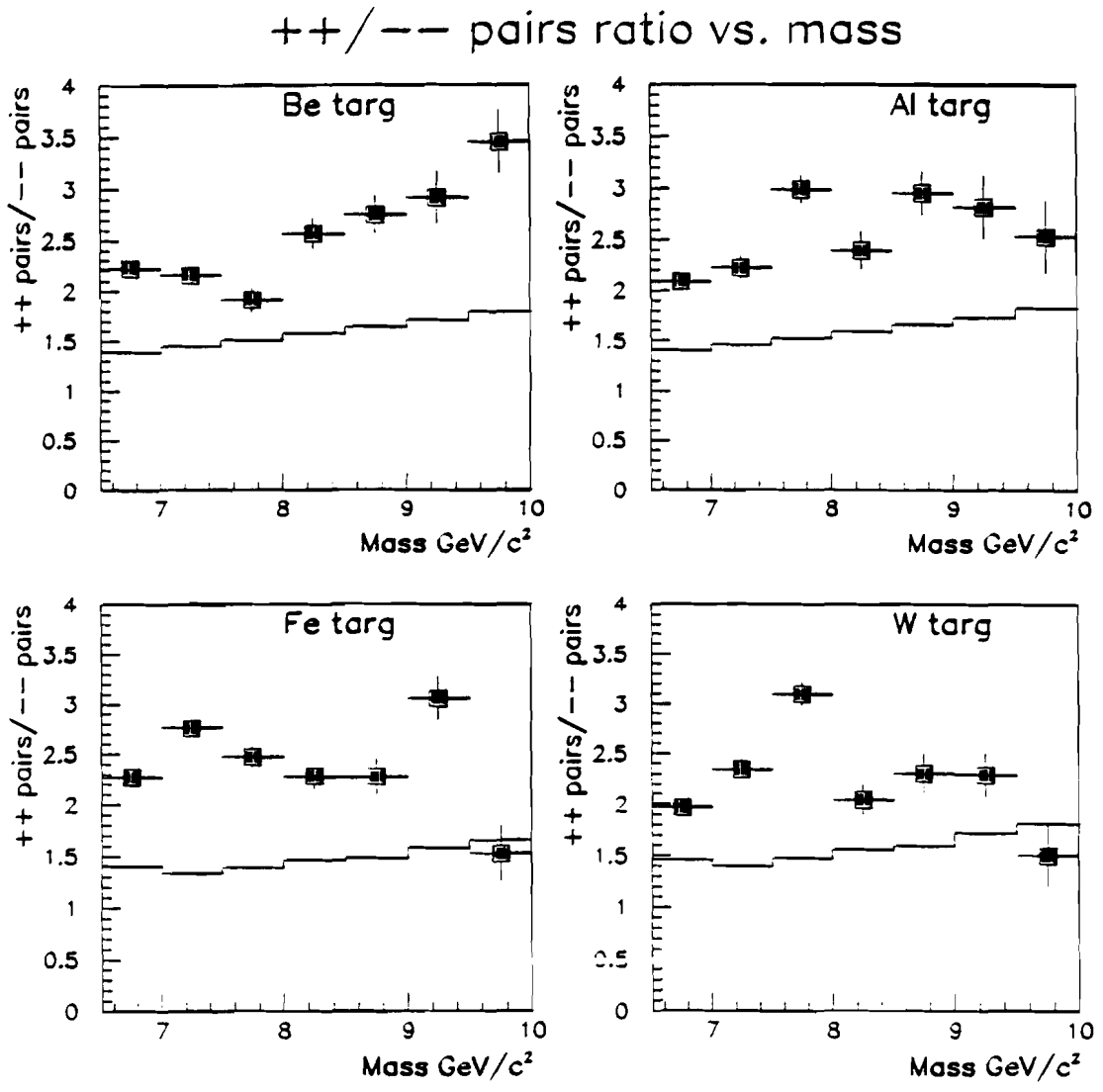

Figure 5.12
Positive like sign/negative like sign pairs ratio plotted as a function of mass.
Solid line is theory prediction.

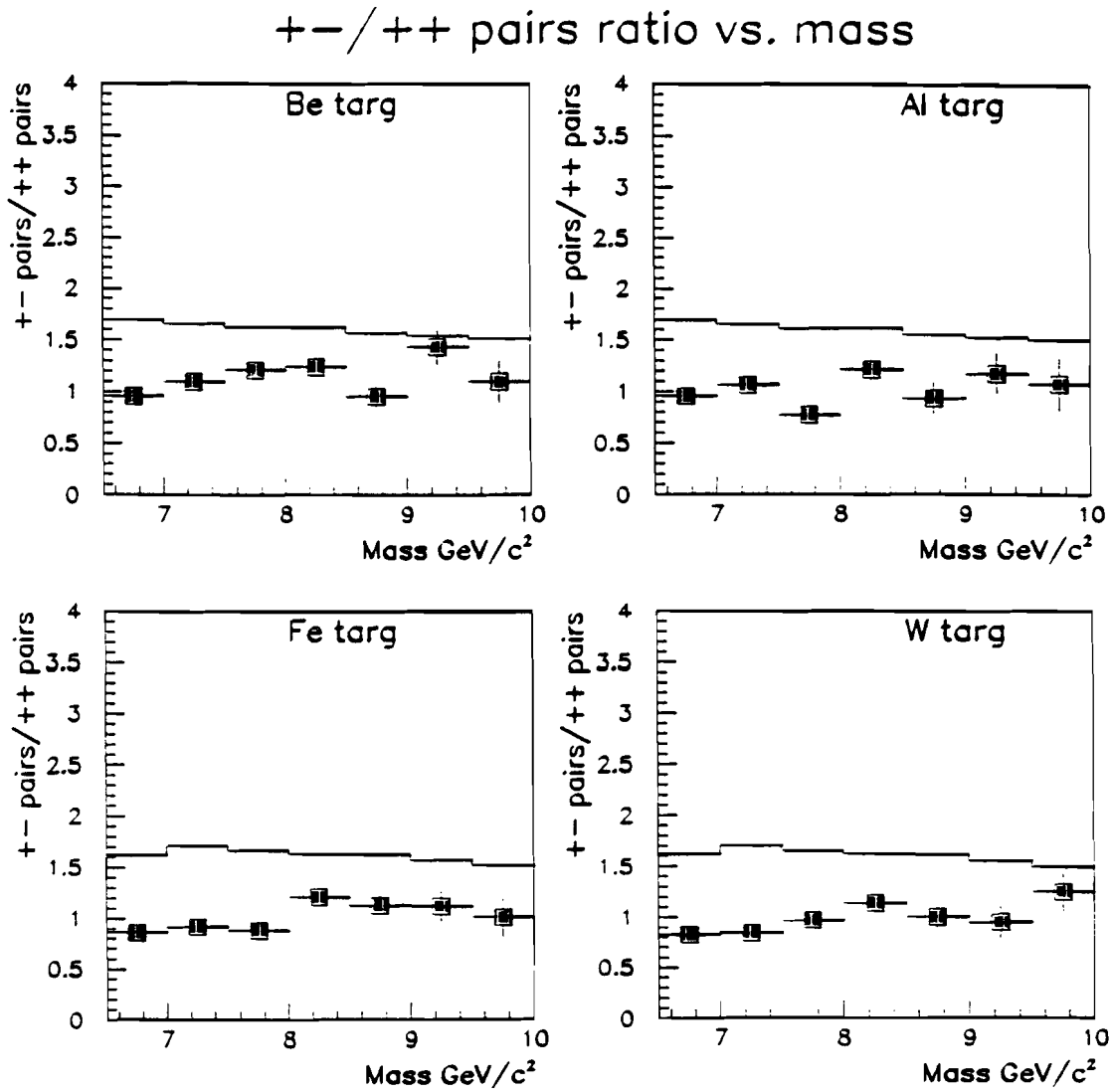

Figure 5.13
Opposite sign/positive like sign pairs ratio plotted as a function af mass.
Solid line is theory prediction.

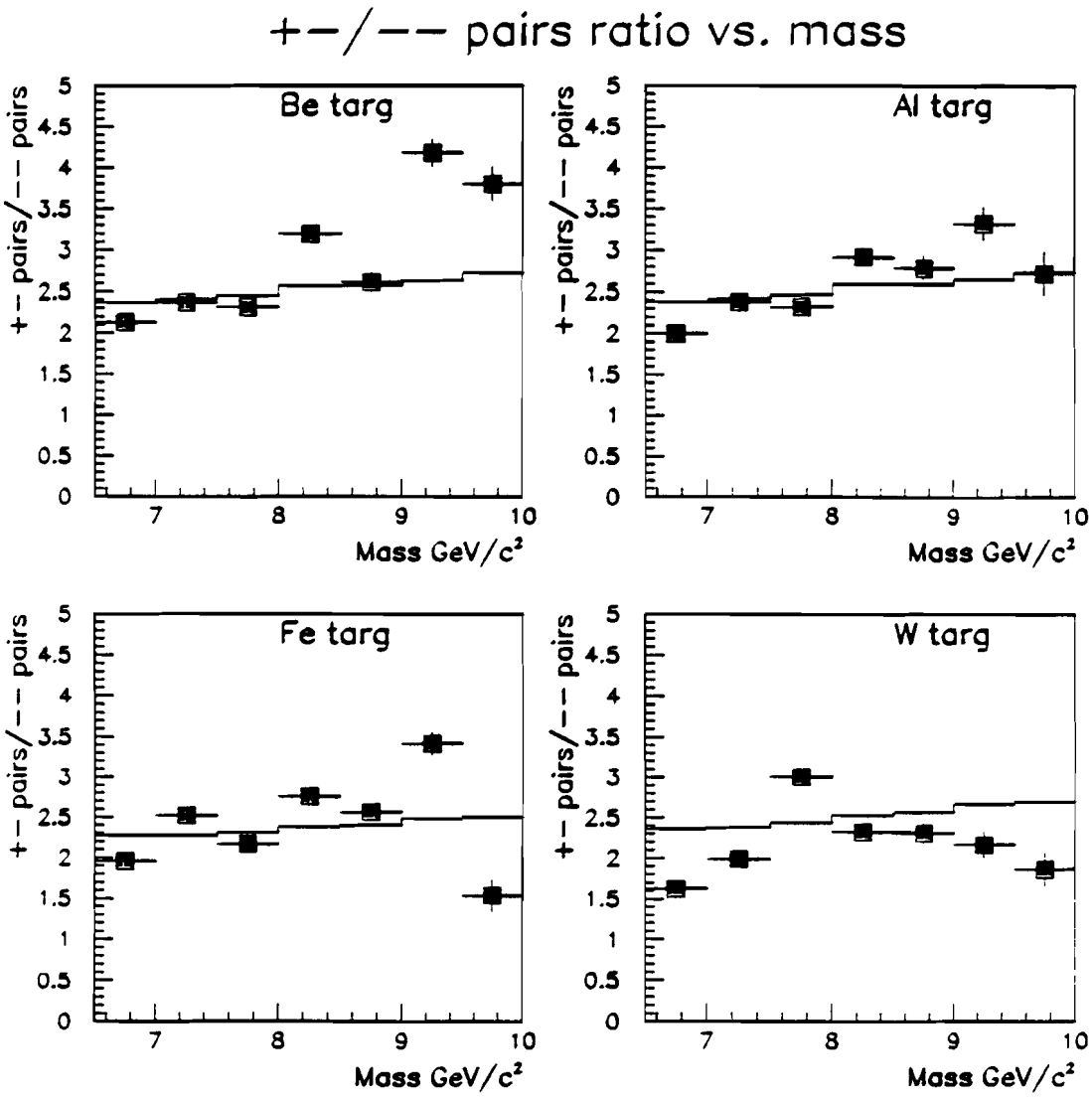

Figure 5.14
Opposite sign/negative like sign pairs ratio plotted as a function of mass.
Solid line is theory prediction.

CHAPTER 6

QCD CALCULATION

The data from the previous section are believed to be the final state products from gluon and quark interactions, the constituents of protons and neutrons. This chapter will discuss the theory involved in obtaining cross sections predicted by Quantum Chromodynamics, in particular, the parametrisations used in the program that generated the curves shown with the data.

6.1 QCD

Quantum Chromodynamics is the theory that describes the interactions of the strong force; the force that binds the nucleus and nucleons together through interactions with colour charge. The chief difficulty in trying to experimentally test the theory is the confinement, at long range, of the quarks and gluons into states that are colour-neutral. This arises from the fact that the gluon, unlike the photon, carries charge and can interact with itself and other gluons. The constant gluon interaction results in a "colour tube" of constant energy per unit length as any two colour-charged particles are separated. This manifests as a potential $V \sim R$. Photons, by contrast, have no such hindrance to their propagation, which is reflected in the $1/R$ long-range form of the electromagnetic potential. This is sometimes referred to as "infrared slavery". A scattered quark or gluon manifests itself as hadrons when the potential energy of the separation is large enough to create a quark-antiquark pair, each of which "dresses" a scattered parton into a colour-neutral particle.

This "fragmentation" of the scattered parton into hadrons, and their arrangement inside the nucleon, are too complicated to be calculated directly. QCD can only make predictions in the regime where the coupling constant, α_S, is small enough to use perturbation techniques. Information concerning the initial states in the nucleon and the final states fragmenting into hadrons come solely from experimental observation. So, the hadron pair production in the lab is a convolution of the QCD parton interactions, parton distribution in the nucleus, and the transformation of the scattered parton into the jets with leading hadrons. This is pictured schematically in Figure 6.1.

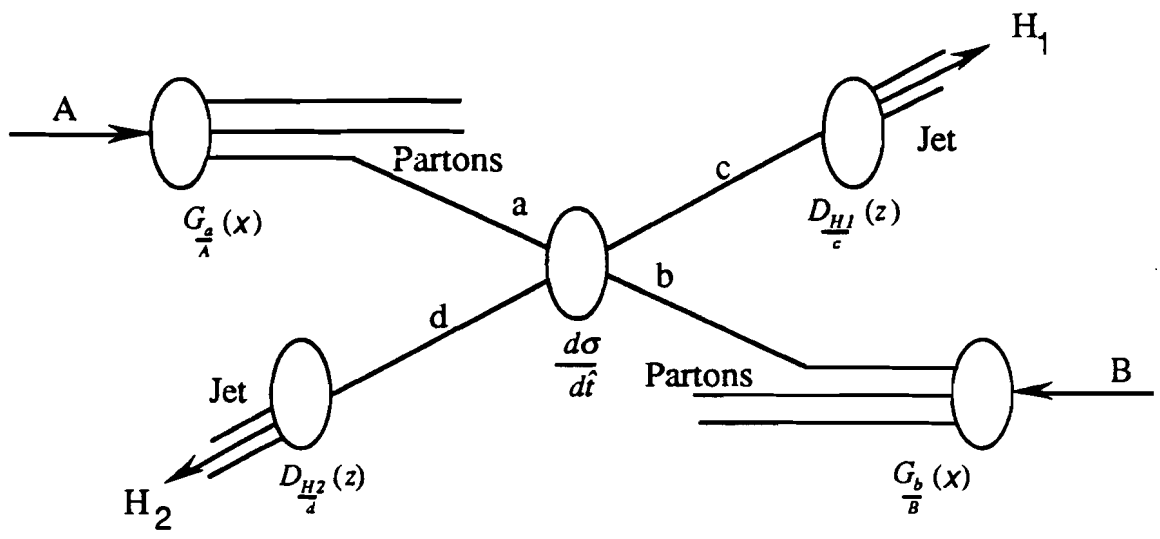

Figure 6.1
Schematic of hadron interaction

6.1.1 Distribution and Fragmentation Functions

The parton composition of nucleons is described by structure functions. These are parametrisations of results of deep inelastic lepton-hadron scattering experiments[23], and are expressed as functions of the fractional momentum of the parent hadron, x. They are Ga/A(x) and Gb/B(x) in the diagram below, and express the probability of hadron A(B) producing a parton a(b) with fractional momentum x

between x and dx. Analogously, the final state parton "decomposition" into hadrons is described by "fragmentation" functions. These are parametrisations of results from e+e- annihilation experiments[24], and are expressed as functions of the fractional momentum of the parent parton, z. These are denoted by $D_{h1/c}(z)$ and $D_{h2/d}(z)$ in Figure 6.1, and express the probability that parton c(d) fragments into a hadron h1(h2) with fractional momentum z between z and dz

The actual QCD cross sections, denoted by $\frac{d\sigma}{d\hat{t}}$ are computed from lowest-order Feynman diagrams, shown in Figure 6.2. All the lowest order processes can be expressed in the following way

$$\frac{d\hat{\sigma}_{(a,b\to c,d)}}{d\hat{t}} = \frac{1}{16\pi\hat{s}^2}\left|M_{(a,b\to c,d)}\right|^2 \tag{6.1.1}$$

where M is the scattering matrix element of the parton subprocesses, and $\hat{s}$ is the square of the center-of-mass energy. The coupling constant for the strong interactions, α_s, describes the strength of the interaction at each vertex for the diagrams in Figure 6.2. There are two vertices for each of the lowest-order diagrams, so the matrix element $M_{a,b\to c,d}$ can be expressed as

$$\left|M_{a,b\to c,d}\right|^2 = \alpha_s^2\left|\hat{M}_{a,b\to c,d}\right|^2. \tag{6.1.2}$$

so that the lowest order subprocesses are given by

$$\frac{d\sigma_{a,b\to c,d}}{d\hat{t}} = \frac{\alpha_s^2}{\hat{s}^2}\pi\left|\hat{M}_{a,b\to c,d}\right|^2. \tag{6.1.3}$$

The explicit expressions for $\hat{M}_{a,b\to c,d}$ for all the lowest-order QCD diagrams are given in Tabled 6.1, expressed terms of the Mandelstam variables described in the next section.

6.1.2 QCD coupling constant

At close range (i.e., high energy, or momentum transfer) the value of the couping constant α_s, becomes smaller. This is a result of an inverse screening process that takes

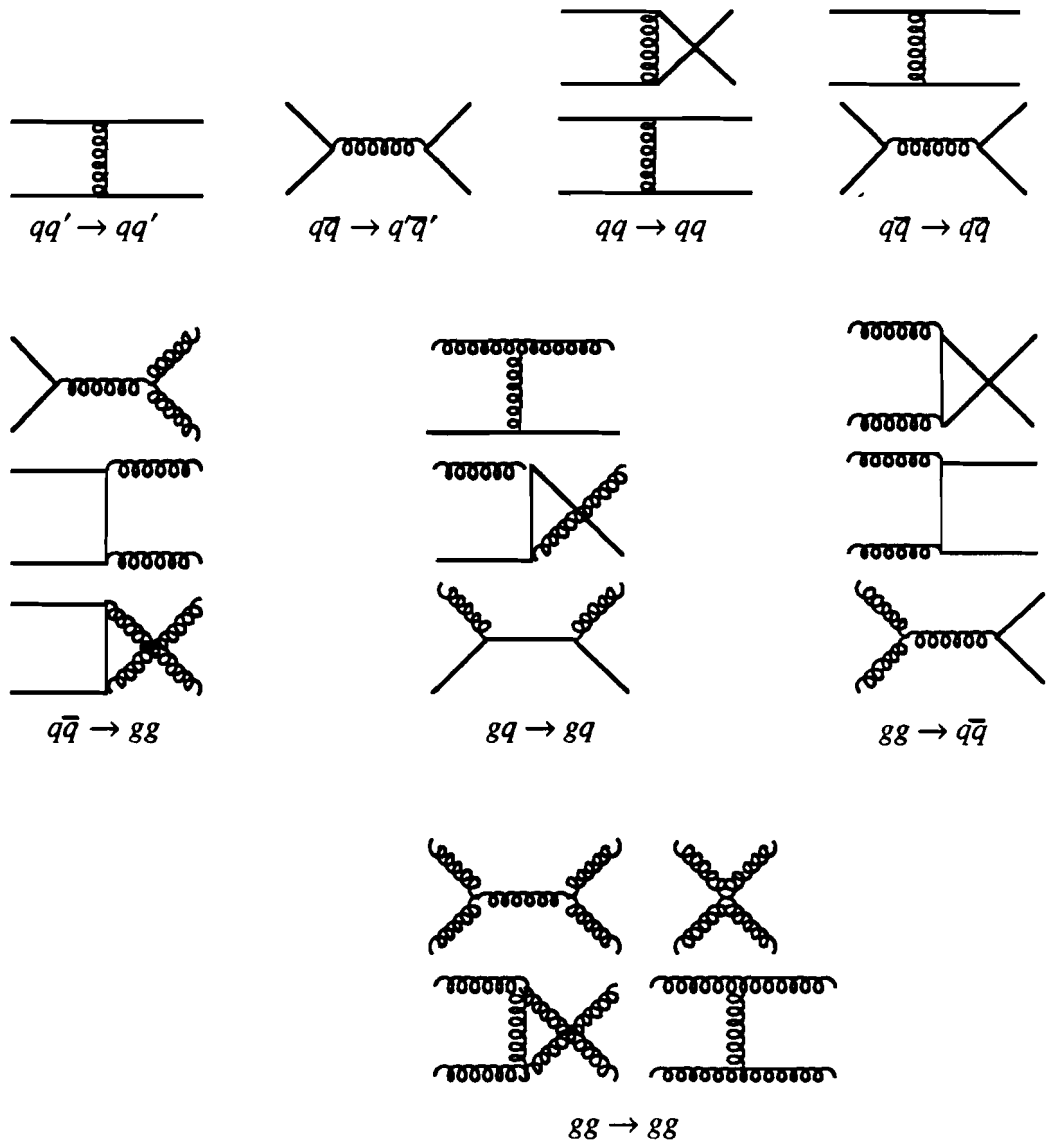

Figure 6.2
Feynman Diagrams for lowest order QCD processes

place around the "bare" colour charge. A bare electron charge will polarise the vacuum such that the spontaneous e^+e^- pairs will align with the positive charges closer to the electron, screening its true charge. Analogously, a bare colour charge induces q^+q^- pairs. However, gluon pairs, which spread out the effective colour of the quark are also produced. The additional diagrams are enough to reverse the screening effect of the q^+q^- pairs. The closer the scatter, the less effective charge is seen, and the coupling

"constant", which depends on the charge, is lower. This is referred to as "asymptotic freedom"; at very close range the quarks and gluons, behave as quasi-free particles, whose interactions can then be calculated perturbatively. The high-p_t hadron pairs observed in E711 are the final states of such close-range interactions.

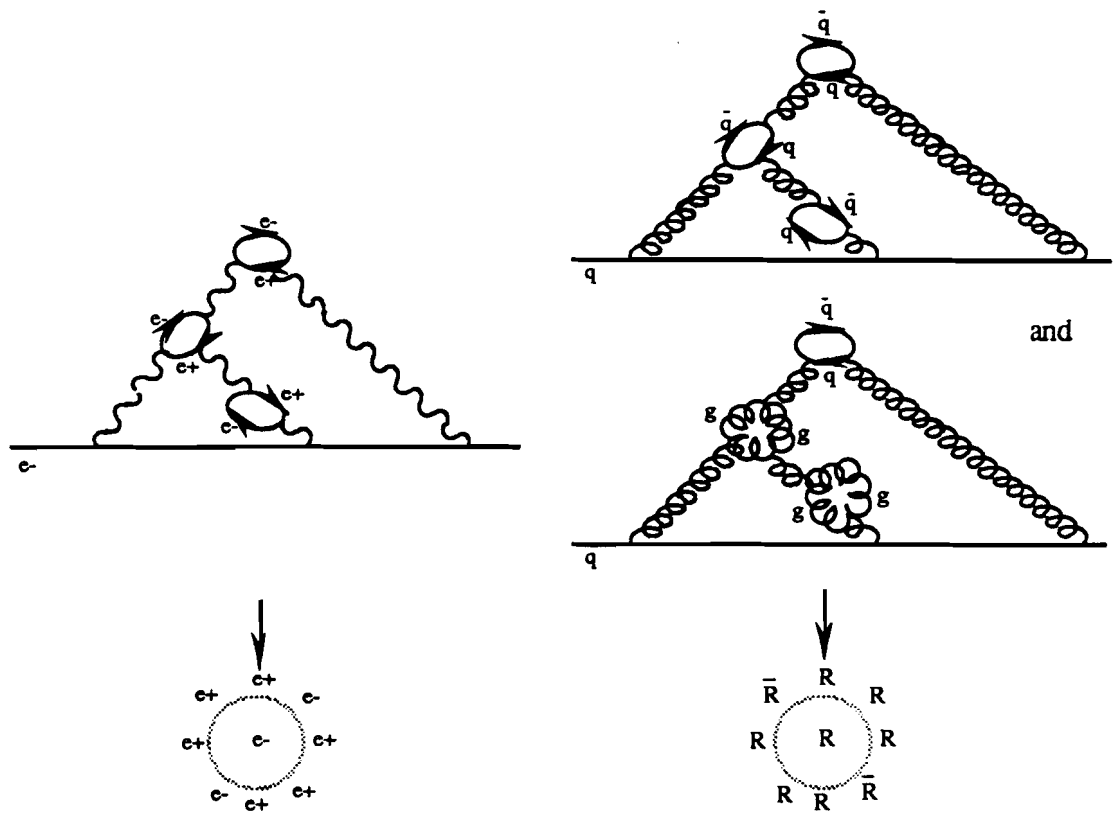

FIGURE 6.3
Screening of electromagnetic charge (left) compared with strong charge (right).
The gluon self-coupling enhances colour charge.

So the coupling "constant" is actually a function of the nearness of the interaction, and, by implication, the energy or momentum transferred. This is characterised by the quantity Q^2, with units of energy squared. Its definition is somewhat ambiguous, because of the diversity of the parton subprocesses that contribute to the cross sections. One definition found to agree well with CCOR[25] data is to set $Q^2=p_t^2$, the momentum transfer squared of the interaction. This was chosen for calculations shown with the cross sections of the last chapter.

As in the case with Quantum Electrodynamics (QED), the exchange gluon in strong interactions will also spontaneously transform into a q^+q^- pair. These higher order (loop) terms are handled by a redefinition of the coupling constant as:

$$\alpha_s(Q^2) = \frac{12\pi}{b\ln(Q^2/\Lambda^2)} + O(\ln^2(Q^2/\Lambda^2)) \qquad (6.1.4)$$

where b = (33-2n_f) ,n_f equals the number of quark flavours.The above expression for α_s is a result of renormalisation of single loop diagrams, analogous to a similar expression in QED. "Renormalisation" is actually a reparametrisation of the integrals involved in calculating the matrix elements containing these loop singularities. The parameter Λ is a scale factor and is a relic of renormalisation. The value for Λ is set at ~ 800 MeV, determined from fits to structure function data[26]. For interactions where p_t is greater than 1 GeV/c, α_s becomes small enough for perturbation techniques to become applicable.

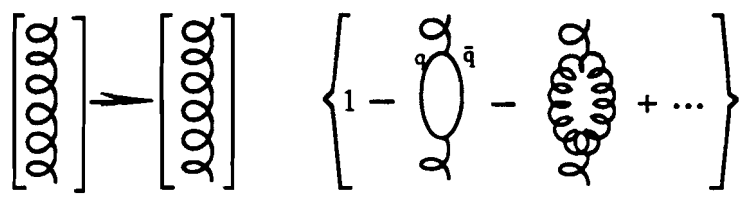

Figure 6.4
Redefinition of the strong coupling constant to include loops diagrams

Perturbative QCD does not directly address the definition of the fragmentation or structure functions, but does describe their evolution with Q^2. The perturbative couplings of quarks to gluons, and gluons to gluons at a particular scale (Q^2 of the interaction) serve to specify how a parton of a certain scale Q^2 "fragments" into partons of scale $Q_0^2 < Q^2$. In analogy to the fragmentation described above, a distribution function can be defined describing the number of partons of type p and scale Q_0^2 in a jet initiated by parton of type q and scale Q^2

$$dN_p = D_{p/q}(z, Q^2, Q_0^2)dz. \qquad (6.1.5)$$

Perturbative QCD can determine how $D_{p/q}$ evolves with changing Q^2 as long as both Q^2 and Q_0^2 are large enough to justify a perturbative analysis. The integral-differential equation containing this QCD information at lowest non-trivial order in perturbation theory is identical to the Altarelli-Parisi equation describing distribution functions within hadrons. Both equations are driven by the same type of collinear singularities (radiated gluon being collinear with its parton "leg").

The discussion of these evolution equations, and the renormalisation of the integrals necessary to handle the singularities in QCD calculations is beyond the scope of this chapter. More detailed discussion can be found in reference [27]. The point here is that the structure and fragmentation functions become functions of the scale factor Q^2; $D(z)$ and $G(x)$ become $D(z,Q^2)$ and $G(x,Q^2)$. In this manner, the higher order corrections to the lowest order QCD cross sections can be effectively absorbed into scale-dependent expressions for these functions. The hadronic cross section then comprises a convolution of the Q^2 dependent structure and fragmentation functions with the lowest order QCD subprocesses. For the calculations in this dissertation, the "leading log" approximation was used. This amounts to including all higher order terms in the calculations (α_s^2, α_s^3, etc.), but retaining only those terms of the form α_s^{n+2} $\ln^n(Q^2)$. Only the first term in the expression of the coupling constant α_s is retained. At the leading-log level the scale factor Q^2 of the structure and fragmentation functions, and the Q^2 in the expression for the coupling constant are formally equivalent, and are merged in the calculation.

6.2 Calculations

6.2.1 Parton kinematics

The explicit calculations are in terms of the nucleon momentum fractions x_a

and x_b, the parton momentum fractions, z_a and z_b and the Mandelstam variables. For initial state hadron four-vectors p_a and p_b, and final state hadron four vectors p_c and p_d, the Mandelstam variables are defined to be:

$$\begin{aligned} \hat{s} &= x_a x_b s, \\ \hat{t} &= -x_b p_t \sqrt{s} e^{y_2}, \\ \hat{u} &= -x_a p_t \sqrt{s} e^{-y_2}. \end{aligned} \tag{6.2.1}$$

In the frame of a highly energetic hadron, the constituents can be considered to be travelling in the same direction, with little transverse momentum. In addition, the internal state of the constituents will have a lifetime which is lengthened by relativistic time dilation. The time of the actual hadron-hadron interaction is assumed relatively short compared to the lifetime of the initial state of the constituents, so for the duration of the interaction the particles can be considered "quasi-free". In this scheme, the masses of colliding hadrons and partons are ignored, as is the transverse momenta of the partons in the initial state hadrons. The p_t of each of the colliding constituents is approximated as equal and opposite. With these assumptions a set of Mandelstam variables can be defined at the parton level:

$$\begin{aligned} \hat{s} &= x_a x_b s, \\ \hat{t} &= -x_b p_t \sqrt{s} e^{y_2}, \\ \hat{u} &= -x_a p_t \sqrt{s} e^{-y_2}, \end{aligned} \tag{6.2.2}$$

where y is the rapidity of the recoiling parton. For this "impulse" approximation, any interaction taking place among the "spectator" (non-colliding) partons, or between the scattered and spectator parton is ignored. Thus, the interference terms normally associated with the quantum-mechanical squaring of amplitudes are not considered in the hard-scattering model, and the cross section for hadronic processes can be expressed essentially as a product of probabilities:

$$d^3\sigma_{(A,B\to c,d+X)} = \int dz_1 D_{c/H1}(z_1) D_{d/H2}(z_2) \sum_{a,b,c,d} G_{a/A}(x_a) G_{b/B}(x_b) \frac{d\sigma_{(a,b\to c,d)}}{d\hat{t}}. \tag{6.2.3}$$

6.2.2 *Dihadron cross section*

E711 triggered on single hadrons rather than jets, so a formalism must be introduced here specific to dihadron cross sections. The fragmentation functions are now labelled $D_{H1/c}$ and $D_{H2/d}$, the probability of a hadron H1(H2) produced from parton c(d) with momentum fraction z between z and $z+dz$. Then, the calculations are carried out using the first order scattering subprocesses, absorbing the Q^2 dependence into the structure and fragmentation functions. These are now expressed as functions of Q^2.The quantities M, Y and Δ denote invariant mass, rapidity and net transverse motion of the dihadron system. In the approximation that parton-k_t effects are ignored, the following relations are derived

$$\begin{aligned} M^2 &= z_1 z_2 M^2_{dijet} \\ \Delta &= p_T(z_1 - z_2) \\ Y &= Y_{dijet} - ln\left(\frac{\sqrt{M^2+\Delta^2}}{M}\right) - \left[\sqrt{\frac{z_1}{z_2}}\frac{1+cos\,\theta}{2} + \sqrt{\frac{z_2}{z_1}}\frac{1-cos\,\theta}{2}\right] \end{aligned} \tag{6.2.4}$$

where z_1 and z_2 are the momentum fractions of hadrons 1 and 2, p_t is the transverse momentum of the jet producing the leading hadron, and M_{dijet} and Y_{dijet} are the invariant mass and rapidity of the dijet system producing the hadron pair. All the above quantities can be used to express the cross section in terms of M, Y, Δ and $cos\,\theta$ (the parton-parton centre-of-mass scattering angle) as

$$\begin{aligned} &\frac{d^3\sigma}{dY dM d\Delta d\cos\theta} \\ &= \frac{M^2}{2s}\int dz_1 D_{c/H1}(z_1,Q^2) D_{d/H2}(z_2,Q^2) \frac{2}{z_1 P_t(z_1+z_2)} \sum_{a,b,c,d} G_{a/A}(x_a,Q^2) G_{b/B}(x_b,Q^2) \frac{d\sigma_{(a,b\to c,d)}}{d\hat{t}} \end{aligned} \tag{6.2.5}$$

This calculation of the cross section was used to generate the curves shown with

the data presented in the last section. The atomic number dependence is assumed to be linear (i.e. α is equal to 1). The fragmentation functions used are described in ref. [28] and the structure "set one" functions are from ref. [29]. The value of Q^2 in these calculations was set to p_t^2. Calculations using this definition of the Q^2 agreed well with the data from the Cern-Columbia-Oxford-Rockefeller (CCOR) experiments.

The relative contribution of the subprocesses varied with the mass and charge state in the QCD calculation. Table 6.2 gives percentages from each type of lowest-order diagram for the three charge states at three different masses. These percentages reflect the characteristics of the parton structure functions. In particular, the gluon distribution falls more rapidly with x than that of the quarks, so at higher masses the diagrams involving gluons contribute less to the overall cross section. The relative contribution of the quark flavours also vary in the QCD calculation, which leads to varying ratios of different hadrons. In the E711 data, the dihadron events were composed largely of pions. For masses above 7 GeV/c^2, the π:K:p was calculated to be approximately 8:3:1.

Subprocess	Cross Section
$qq' \to qq'$	$\frac{4}{9}\frac{s^2+u^2}{t^2}$
$qq \to qq$	$\frac{4}{9}\left(\frac{s^2+u^2}{t^2}+\frac{s^2+t^2}{u^2}\right)-\frac{8}{27}\frac{s^2}{tu}$
$q\bar{q} \to q'\bar{q}'$	$\frac{4}{9}\frac{t^2+u^2}{s^2}$
$q\bar{q} \to q\bar{q}$	$\frac{4}{9}\left(\frac{s^2+u^2}{t^2}+\frac{t^2+u^2}{s^2}\right)-\frac{8}{27}\frac{u^2}{st}$
$gq \to gq$	$-\frac{4}{9}\left(\frac{s}{u}+\frac{u}{s}\right)+\frac{s^2+u^2}{t^2}$
$q\bar{q} \to gg$	$\frac{32}{27}\left(\frac{t}{u}+\frac{u}{t}\right)-\frac{8}{3}\frac{t^2+u^2}{s^2}$
$gg \to q\bar{q}$	$\frac{1}{6}\left(\frac{t}{u}+\frac{u}{t}\right)-\frac{3}{8}\frac{t^2+u^2}{s^2}$
$gg \to gg$	$\frac{9}{2}\left(3-\frac{tu}{s^2}-\frac{su}{t^2}-\frac{st}{u^2}\right)$

Table 6.1

Cross sections for the lowest order QCD subprocesses

Mass	$qq \to qq$	$q\bar{q} \to q\bar{q}$	$q\bar{q} \to gg$	$gg \to q\bar{q}$	$gq \to gq$	$gg \to gg$
5 GeV (++)	20	4	<1	2	50	24
10 GeV (++)	62	4	<1	<1	31	3
15 GeV (++)	89	2	<1	<1	9	<1
5 GeV (+ -)	17	4	<1	4	49	26
10 GeV (+ -)	57	4	<1	3	32	4
15 GeV (+ -)	86	2	<1	<1	11	<1
5 GeV (- -)	14	4	<1	2	49	31
10 GeV (- -)	50	4	<1	2	38	6
15 GeV (- -)	81	3	<1	<1	15	<1

Table 6.2
Relative contributions of lowest order subprocesses

6.2.3 *Angular Distributions.*

The Mandelstaam parameters $\hat{t}$ and $\hat{u}$ have very simple expressions involving $\cos\theta$:

$$\hat{t} = \frac{\hat{s}}{2}(1 - \cos\theta)$$
$$\hat{u} = \frac{\hat{s}}{2}(1 + \cos\theta) \qquad (6.2.6)$$

The simpliest lowest-order diagram, $q_i q_j' \to q_i q_j'$ (scattering of dissimilar quarks) gives the Rutherford formula presented in chapter 1. The presence of other scattering subprocesses complicates this expression, but the dominant processes are those with either $\hat{u}^2$ or $\hat{t}^2$ in the denominator. With the assumption of non-interference of the lowest order processes, the QCD predictions can be parametrised by

$$\frac{1}{2}\cdot\left[\frac{1}{(1-\cos\theta)^{n}}+\frac{1}{(1+\cos\theta)^{n}}\right]$$

Table 5.11 shows the results from fitting the data to this parametrisation against the predictions from QCD calculations. An interesting observation is that the data show a difference, in particular, of the shape of the distribution between the like-sign and opposite-sign angular distributions. This could be an indictment of any of a number of assumptions made above, yet the like-sign distributions seem to agree with QCD predictions within the systematic and statistical errors.

CHAPTER 7

CONCLUSION

The analysis described in this dissertation studied two predictions of the current theory of the strong interactions, or Quantum Chromodynamics: the mass and angular distributions for dihadron production. E711 was unique in its wide angular acceptance for all three states of charged dihadron production: +-, ++, and -- pairs.

The mass distributions were calculated for the region of phase space where the angular ($\cos\theta$) distributions were to be studied. This was to check the validity of QCD "leading log" calculations for overall normalisation. The data plots were shown to fall close to the QCD prediction for the opposite-sign (+-) and negative like-sign (--) pairs, given the statistical and systematic errors, but with consistently higher-than-predicted cross sections for the positive like-sign (++) pairs. Moreover, the ratio of positive (++) pairs over negative (--) pairs produced plotted against mass was consistently higher, as much as a factor of two, than the QCD calculations predicted. This was found to be true for data from all targets. The +-/-- ratios did not show such a large discrepancy, suggesting that this may not be a result of misunderstood acceptance for negatively charged tracks.

The $\cos\theta$ cross sections were then constructed, normalised to their value at $\cos\theta = 0.0$. These were obtained separately for the three different charge states, and separated into mass bins of $M > 7.5$ GeV/c^2 and $6.5 < M < 7.5$ GeV/c^2 for each state.The $\cos\theta$ distributions for $M > 7.5$ were found to be consistent, within errors, with the parametrisation of QCD results only in the -- charge state. The opposite-sign, and positive like-sign angular distributions appeared flatter than the negative like-sign distributions.

In all cases, the distributions for $M<7.5$ GeV/c^2 produced a worse fit to the parametrisations, most likely a reflection of the indeterminacy introduced by accepting hadron pairs of net P_t up to 3.0 GeV/c. The $\cos\theta$ reconstruction is less distorted at higher mass by the P_t of the pair.

In summary, results from Experiment 711 has shown deviations from the QCD predictions for the mass and angular dependence of dihadron production that are dependent on the charge state of the hadron pair. These may reflect the limitations of the assumptions made in the QCD calculations, particularly in disregarding interference terms that would give rise to differences in distributions for the different quark flavours. There could also be nuclear effects distorting the distribution functions that are not yet understood. This analysis has raised some intriguing questions concerning flavour dependence in the strong interactions that, given the limited statistics and inherent sensitivity of the analysis to detector inefficiencies, cannot be resolved definitively in one experiment. Other experiments at higher luminosity, particularly if pion beams are available, will be needed to compare with the results presented here, and should be done as flavour-independence remains a largely unconfirmed assumption of QCD.

APPENDIX 1

ENERGY CALIBRATION

For triggering purposes, the absolute calibration of the calorimeter needed to be determined - that is, the amount of energy deposition in MeV represented by a count on an ADC - in order to correctly set discriminator threshold levels in the trigger electronics. A calibration run was made in May 1985 where both halves of the calorimeter were illuminated by a pion beam of fixed energy steered vertically by a dipole magnet. The experiment was run in the muon trigger mode described in section 2.7, but without the chamber muon counters in the coincidence, allowing illumination of the entire height of the calorimeter face.

In principle, the energy of a particle deposited in the calorimeter can be expressed as

$$E = \sum_n C_n P_n \tag{A1.1}$$

where n is the number of PMT's carrying a signal, P_n is the pulse height in ADC counts, and C_n is the calibration constant for the nth PMT. The C_n's need to be determined.

The relative calibration of the 4 longitudinal (z) sections (*EM, H1, H2, H3*) in each calorimeter was established using data from dedicated muon runs, with the relative calibration of the 16 vertical modules within each longitudinal section obtained by adjusting the high/low gain ratios on each phototube in response to LED pulses (see section 2.6). These reduced the number of absolute calibration constants to those of the

total logitudinal sections, or

$$E = \sum_k C_k \sum_{i,j} P_{ijk} \tag{A1.2}$$

where P is the pulse height in each z section (scaled by the corresponding muon peak from the hardware calibration). The subscripts i denote east and west PMTs, j the PMT's in the vertical direction, and k the longitudinal sections. The calibration constants C_k were determined by minimising the chi-squared

$$\chi^2 = \left[E_{beam} - \frac{\sum_k C_k \sum_{i,j} P_{ijk}}{\sigma_k} \right]^2 \tag{A1.3}$$

with respect to each C_k. The error on the kth term, σ_k is defined as

$$\sigma_k^{\,2} = dE_{beam}^2 + dE_{cal}^2 \tag{A1.4}$$

One run was dedicated to estimating the systematic errors. Since dE_{beam} was known, the energy resolution was determined from

$$\left(\frac{\sigma}{E}\right)^2 = \left(\frac{dE_{beam}}{E}\right)^2 + \left(\frac{dE_{cal}}{E}\right)^2 \tag{A1.5}$$

where E is the average beam energy. dE_{cal}/E can be expressed as const/$\sqrt{E}$. This is a consequence of assuming that the calorimeter response is homogeneous and isotropic[30]. From the calibration data the calorimeter resolution was found to be $.64/\sqrt{E}$. Figure A1.1 shows the calculated total energy in the calorimeter, determined by minimising the χ^2 mentioned above. Table A1.1 lists the relative calibrations for each z section. The errors listed are statistical. The systematic errors, estimated from the difference between calibration constants of two separate runs, were 5%, 2%, 9% and 19% for each of the C_k's, respectively.

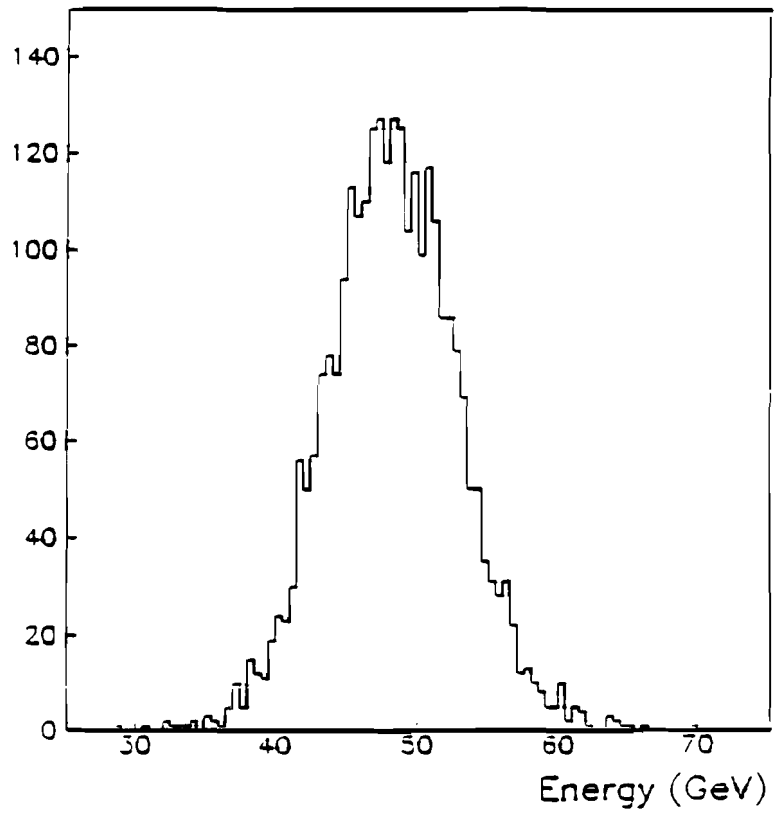

Figure A1.1
Total energy deposited in calorimeter, calculated from calibration constants

z module	Calibration Constant c
EM	0.446±0.002
H1	0.930±0.004
H2	0.855±0.009
H3	0.923±0.030

Table A1.1
The calibration of each longitudinal section relative to the sum of all PMT pulse heights, scaled to their corresponding muon peaks

APPENDIX 2

CHAMBER CONSTRUCTION

The 5 multi-wire drift proportional chambers (MWPC's) were stationed in front of the the calorimeter and hodoscopes. Each station was constructed from several planes of wires, stacked parallel to one another. The wire spacings varied from chamber to chamber, and were chosen such that corresponding sense wires in each chamber projected back to the target.

The sense wire planes were the anode planes and each chamber contained 4, corresponding to the 2-dimensional views described in chapter 2: X,Y,U and V. Cathode planes produced the electric field perpendicular to the planes that accelerated electrons from the ionised gas toward the anodes. Grounding planes were also included to shield the anode wires from external noise. Labelling the ground, cathode and anode planes as G, C and (X,Y,U,V), the construction for each plane starting upstream towards the calorimeter was:

Chambers 1 and 2: G C U C X C G (space) G C V C Y G

Chambers 5, 3 and 4: G C U C V C X C Y C G

The largest chambers (3 and 4) also included field wires placed between the sense wires in the anode plane. These were considered necessary to maintain uniform field strength and drift velocity for the larger wire spacings. The placement downstream of the magnets at 5.39, 6.75, 8.23, 11.18 and 14.86 m for DC1, DC2, DC3, DC4 and DC5, respectively, and their wire spacings formed a projective geometry with the target to simplify the track reconstruction.

The sense wires were gold-plated tungsten, and all others were silver- plated beryllium-copper. The gas used during the '87-'88 run was mixture of argon with 17% carbon dioxide and 0.4% freon in chambers 1, 2, and 5, and a 50% argon - 50% ethane mixture bubbled through ethyl alcohol at $0^{o}C$ for the larger chambers 3 and 4. Tables A2.1-A2.5 list the specifications for wire spacing, voltages, wire diameters, number of sense wires in each plane, and the dimensions of the active regions of the chambers.

Chamber	Sense Wires (mm)	Cathode Wires (mm)	Field Wires (mm)	Ground Wires (mm)
DC1-U,V, X,Y	2.03	1.0	---	2.0
DC2-U,V,X,Y	2.53	1.0	---	2.0
DC3-U,V	4.11	2.0	4.11	2.0
DC3-X,Y	4.17	2.0	4.17	2.0
DC4-U,V	5.47	2.0	5.47	2.0
DC4-X,Y	5.56	2.0	5.56	2.0
DC5-U,V,X,Y	3.05	2.0	---	2.0

Table A2.1
Chamber wire spacing

Chamber	Live Cathodes (kV)	Field Wires (kV)
DC1	-3.05	---
DC2	-3.30	---
DC3	-2.40	-1.40
DC4	-2.30	-1.45
DC5	-3.65	---

Table A2.2
Chamber wire voltages

Chamber	Sense Wires (μm)	Cathode Wires (μm)	Field Wires (μm)	Ground Wires (μm)
DC1	25.4	63.5	---	127.0
DC2	25.4	76.2	---	127.0
DC3	25.4	76.2	76.2	127.0
DC4	25.4	76.2	76.2	127.0
DC5	25.4	76.2	---	127.0

Table A2.3
Chamber wire diameters

Chamber	Y	X	U	V
DC1	544	256	320	320
DC2	544	256	320	320
DC3	544	256	352	352
DC4	544	256	352	352
DC5	576	256	352	352

Table A2.4
Number of sense wires in each chamber plane

Chamber	X (cm)	Y (cm)
DC1	103.9	110.4
DC2	129.5	137.6
DC3	224.7	226.8
DC4	299.1	302.5
DC5	169.3	175.7

Table A2.5
Chamber active region dimensions

APPENDIX 3

MOMENTUM CALCULATION

The trackfitter provided slopes and intercepts in x-z and y-z planes for each particle track it reconstructed. these are the parameters of the trajectories downstream of the magnetic fields. To reconstruct the momenta upstream of the magnet, the effect of the magnetic field was approximated, for the purposes of calculation, by having the +-1.16 GeV/c p_{mag} kick imparted at the centre plane (in z) of the total magnetic field. The "single bend" calculation was done by extrapolating the downstream trajectory to the bend plane, then defining a trajectory from the x-y point in the bend plane to the centre of the target (see Figure A1). The original particle momenta are determined by

$$s_{xz}^{u} = \frac{s_{xz}^{d} \cdot d_{x_{int}} - x_{targ}}{z_{mag} - z_{targ}} \tag{A3.1}$$

where s_{xz}^{u} and s_{xz}^{d} are the upstream and downstream slopes in the x-z plane z(mag) is the position of the magnetic field bend plane and x_{int} is the x intercept at z = 0. x_{targ} and z_{targ} are the x and z coordinates of the target centre. The y-z slope is unaffected by the horizontal magnetic kick.

The vector representations of the trajectories in Figure A3.1 are precisely those of the momenta. The magnetic field imparts a deflection, but no net energy, to the particle so,

$$p_{xu}^{2} + p_{zu}^{2} = p_{xd}^{2} + p_{zd}^{2} \tag{A3.2}$$

where $p_{xd} = p_{xu} + p_{mag}$.

With the relationships

$$\frac{p_{xu}}{p_{zu}} = s_{xz}^{u}$$

and (A3.3)

$$\frac{p_{xd}}{p_{zd}} = s_{xz}^{d}$$

some algebraic manipulation and the quadratic formula yields

$$p_{zu} = p_{mag} \cdot \left(\frac{2s_{xz}^{u}\left(s_{xz}^{d\,2} + 1\right) + s_{xz}^{d}\sqrt{s_{xz}^{d\,2} \cdot s_{xz}^{u\,2} + s_{xz}^{d\,2} + s_{xz}^{u\,2} + 1}}{\left(s_{xz}^{d\,2} - s_{xz}^{u\,2}\right)} \right) \tag{A3.4}$$

Then

$$p_{xu} = s_{xz}^{u} \cdot p_{zu}$$

and (A3.5)

$$p_{yu} = s_{yz}^{u} \cdot p_{zu}$$

where the y-z slope is unchanged by the magnetic field.

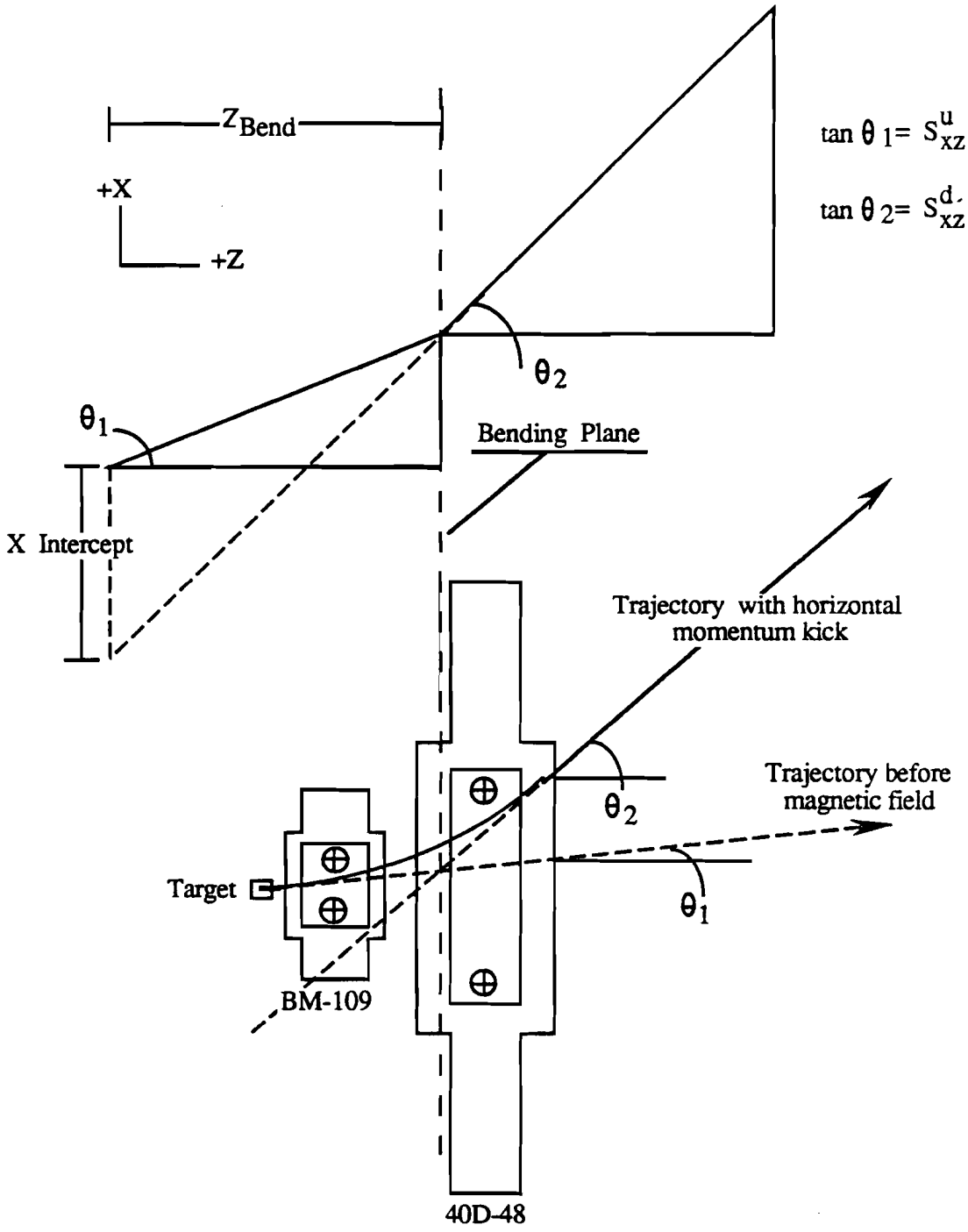

Figure A3.1
Calculation of the momentum using the "single bend" approximation

APPENDIX 4

LORENTZ BOOST OF 2 PARTICLE SYSTEM

The generalised Lorentz transformation for a 3-dimensional boost can be written as

$$x_0' = \gamma\left(x_0 - \vec{\beta}\cdot\vec{x}\right)$$
$$\vec{x}' = \vec{x} + \frac{(\gamma-1)}{\beta^2}\left(\vec{\beta}\cdot\vec{x}\right)\vec{\beta} - \gamma\beta x_0 \qquad \text{(A4.1)}$$

where

$$\vec{x} - \frac{(\gamma-1)}{\beta^2}\left(\vec{\beta}\cdot\vec{x}\right)\vec{\beta}$$

is the component of $\vec{x}$ orthogonal to $\vec{\beta}$[31].

Reconstruction of the dihadron kinematics required a boost to the massive state rest frame, which, in general, was not the rest frame of the beam-target system. For the total dihadron momentum P_{DH} and energy E_{DH}, the boost to the dihadron rest frame along the direction of P_{DH}) is expressed by

$$P_{RF} = \gamma\left(P_{DH} - \beta E_{DH}\right)$$
$$E_{RF} = \gamma\left(E_{DH} - \beta P_{DH}\right) \qquad \text{(A4.2)}$$

where P(RF) and E(RF) are the momentum and energy in the dihadron rest frame and are equal to 0 and the invariant mass, respectively. Solving equations A4.2 yields

$$\beta = \frac{P_{DH}}{E_{DH}}$$
$$\gamma = \frac{E_{DH}}{M_{DH}} \qquad \text{(A4.3)}$$

where M_{DH} is the invariant mass of the dihadron system. For the individual hadrons in the massive state, equations A4.3 can be substituted into equations A4.1 for the expressions

$$\varepsilon = \frac{E_{DH}}{M_{DH}} \cdot \left(\varepsilon' + \frac{P_{DH}}{E_{DH}} p' \right)$$
$$\vec{p} = \vec{p}' - \frac{\left(\frac{E_{DH}}{M_{DH}} - 1 \right)}{\left(\frac{P_{DH}}{E_{DH}} \right)^2} (P_{DH} \cdot \vec{p}') \left(\frac{P_{DH}}{E_{DH}} \right) - \left(\frac{E_{DH}}{M_{DH}} \right) \left(\frac{P_{DH}}{E_{DH}} \right) \varepsilon' \qquad \text{(A4.4)}$$

The primes denote the dihadron rest frame quantities. Using the approximation that the masses of the hadrons are ignored, $\varepsilon' = M_{DH} / 2$. With $P_{DH}^2 = E_{DH}^2 - M_{DH}^2$,equations A5.4 can be reduced to

$$\varepsilon = \frac{E_{DH}}{2} + \vec{P}_{DH} \cdot \vec{p}'$$
$$\vec{p} = \vec{p}' + \vec{P}_{DH} \left(\frac{(E_{DH} - M_{DH}) \vec{P}_{DH} \cdot \vec{p}'}{\left((E_{DH}{}^2 - M_{DH}{}^2) M_{DH} \right)} \right) - \frac{1}{2} \qquad \text{(A4.5)}$$

REFERENCES

[1] F. W. Busser *et al.*, Nucl. Phys. B106, 1 (1976).

[2] A. G. Clark *et al.*, Phys. Scripta 19 79 (1979).

[3] M. D. Corcoran *et al.*, Phys. Scripta 19, 95 (1979)

[4] M. W. Arenton *et al.*, Phys. Rev. D 31, 984 (1985)

[5] J. Gunion and B. Petersson, Phys. Rev. D 22, 629 (1980).

[6] R. J. Fisk, *et al.*, Phys. Rev. Lett. D 40, 984 (1978)

[7] H. Jostlein, *et al.*, Phys. Rev. D 20, 53 (1979)

[8] H. Jostlein, *et al.*, Phys. Rev. Lett. 42 146 (1979)

[9] A. L. S. Angelis *et al.*, Physica Scripta 19, 116 (1979).

[10] B. C. Brown, *et al.*, Phys. Rev. D 29, 1895 (1984).

[11] J. A. Crittenden *et al.*, Phys. Rev. D 34, 2584 (1986)

[12] A.L.S. Angelis *et al.*, Nucl. Phys. B 209, 284 (1982).

[13] J. Bell *et al.*, Phys. Rev. D 18, 3905 (1978)

[14] UA1 Collaboration: Phys. Lett. B 158, 494 (1985).

[15] D. Levinthal, Ph.D. thesis, Columbia University, 1980.

[16] K. R. T. Streets, Ph.D. thesis, Florida State University, 1989.

[17] A. Ito, W. Bosworth, J. Rutherford, A. Lynch, L. Tung and W. Yang, Fermilab Publication, TM 1200 - 2311.00 (1983).

[18] J. F. Bartlett *et al.*, Fermilab Multi User's Guide, PN-97.5 (1979).

[19] V. White *et al.*, IEEE Transactions on Nuclear Science NS-34, 763 (1987).

[20] Fermilab Experimental Physics Interactive Control System users manual. Version 1.00.

[21] J. C. Collins and D. E. Soper, Phys. Rev. D 16, 2219 (1977).

[22] C. H. Georgiopoulos, J. H. Goldman, M. F. Hodous, Nucl. Inst. and Meth. A261, 493 (1987).

[23] D. W. Dukes and J. F. Owens, Phys. Rev. D 30, 49 (1984).

[24] J. F. Owens, Rev. Mod. Phys. 59, 465 (1987).

[25] A.L.S. Angelis *et al.*, Nucl. Phys. B209, 284 (1982).

[26] F. Halzen and A. D. Martin, *Quarks and Leptons: An Introductory Course in Modern Particle Physics* (John Wiley & Sons, Inc. (1984)).

[27] G. Altarelli and G. Parisi, Nucl. Phys. B126, 298.

[28] J. F. Owens, Phys. Rev. D 19, 3279 (1979).

[29] D. W. Duke and R. G. Roberts, Phys. Rep. 120, 275 (1985).

[30] S.Youssef, "A Simple Argument about Calorimeters" D0 note #374, March 1986.

[31] J. D. Jackson *Electrodynamics* (John Wiley and Sons, 1975).